Quantitative scanning tunneling spectroscopy of non-polar III-V compound semiconductor surfaces

Michael Schnedler

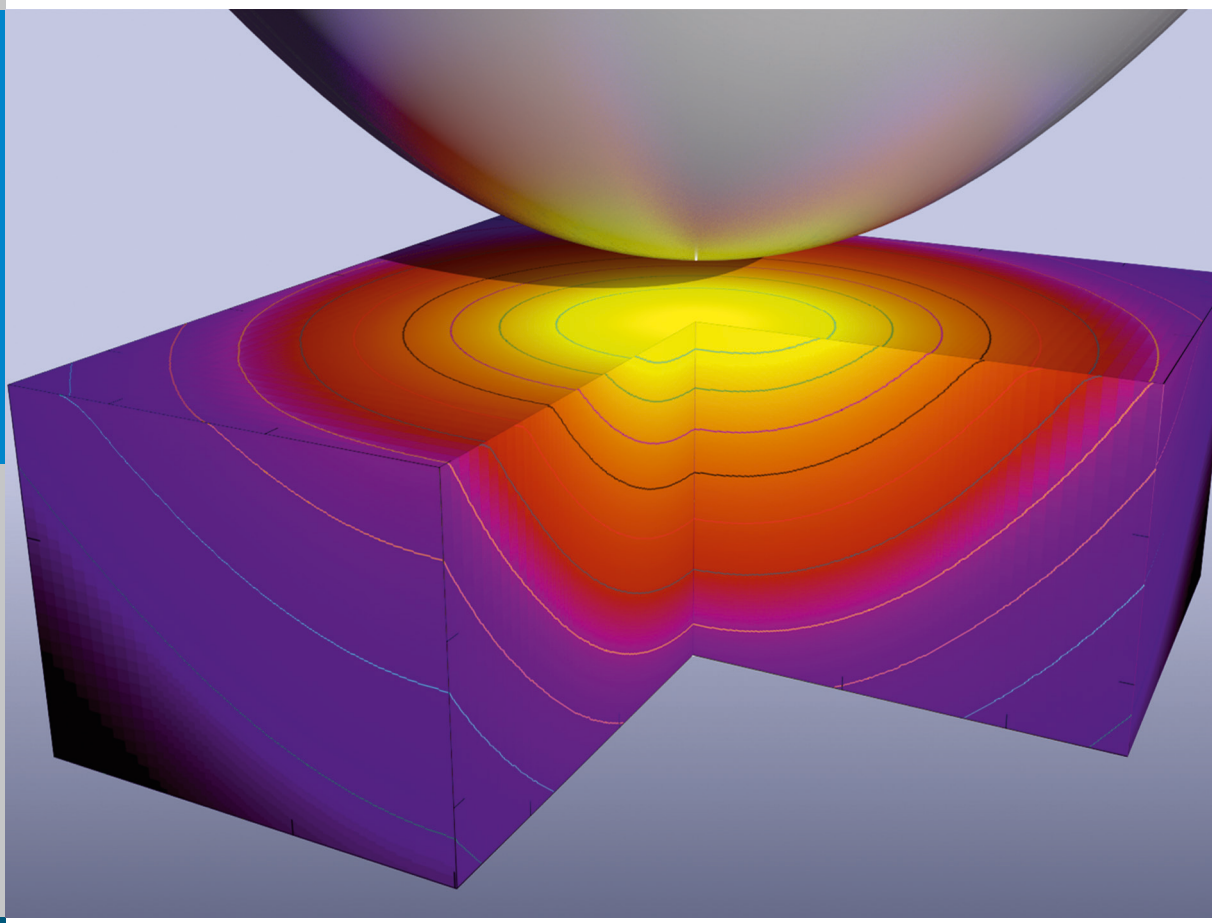

Member of the Helmholtz Association

Information
Band / Volume 44
ISBN 978-3-95806-075-3

JÜLICH
FORSCHUNGSZENTRUM

Schriften des Forschungszentrums Jülich
Reihe Information / Information Band / Volume 44

Forschungszentrum Jülich GmbH
Peter Grünberg Institute (PGI)
Microstructure Research (PGI-5)

Quantitative scanning tunneling spectroscopy of non-polar III-V compound semiconductor surfaces

Michael Schnedler

Schriften des Forschungszentrums Jülich
Reihe Information / Information Band / Volume 44

ISSN 1866-1777 ISBN 978-3-95806-075-3

Bibliographic information published by the Deutsche Nationalbibliothek.
The Deutsche Nationalbibliothek lists this publication in the Deutsche Nationalbibliografie; detailed bibliographic data are available in the Internet at http://dnb.d-nb.de.

Publisher and Distributor: Forschungszentrum Jülich GmbH
Zentralbibliothek
52425 Jülich
Tel: +49 2461 61-5368
Fax: +49 2461 61-6103
Email: zb-publikation@fz-juelich.de
www.fz-juelich.de/zb

Cover Design: Grafische Medien, Forschungszentrum Jülich GmbH

Printer: Grafische Medien, Forschungszentrum Jülich GmbH

Schriften des Forschungszentrums Jülich
Reihe Information / Information, Band / Volume 44

D 82 (Diss., RWTH Aachen University, 2015)

ISSN 1866-1777
ISBN 978-3-95806-075-3

The complete volume is freely available on the Internet on the Jülicher Open Access Server (JuSER) at www.fz-juelich.de/zb/openaccess.

Contents

Chapter 1

Introduction

The Greek philosopher Democritus (460-370 BC) and his mentor Leucippus are said to have been the first who introduced the theory of *atomism.*[1] They proposed that the universe is composed of indivisible elements (atomos) and void, only. The concept was based upon philosophical considerations only. First scientific approaches that employ atomic models, came up in the 18^{th} and 19^{th} century. Especially the development of the kinetic theory of gases, which was motivated by Bernoulli in 1738,[2] developed by Maxwell (1860),[3] and generalized by Boltzmann (1872),[4] represents a milestone for the acceptance of the hypothesis of atoms and molecules, since the macroscopic properties of gases where related to the microscopic motion of a many particle system. In general, the experimental observation of the Brownian motion of particles in a fluid and the theoretical description of this phenomenon, given by Einstein in 1905,[5] is considered as first evidence for the existence of molecules and atoms. Nevertheless, no one had ever observed a single atom at that time.

With the development of modern non-optical microscopes, mankind was enabled to take a look at the atomic world in real space for the first time in more than 2200 years of history of the atom: Shortly after the discovery of magnetic lenses, the electron microscope was invented by Ruska and Knoll in 1931.[6] However, great effort was still needed to overcome spherical and chromatic aberration effects and hence, first images of single atoms where obtained in the early 70s.[7] Five years after the construction of the first electron microscopes, in 1936, Müller invented the field ion microscope[8, 9] and 20 years later he had managed to improve the resolution of this device so far that individual atoms of a sharp tungsten tip became visible.[10] Thus, Müller is said to be the first person who has ever seen an atom. Things dramatically changed with the invention of the scanning tunneling microscope by Binnig and Rohrer in 1981.[11, 12] This technique provided atomic resolution over large regions right from the beginning.

The scanning tunneling microscope (STM) utilizes the quantum mechanical tunnel effect, which leads to a so-called *tunnel current* of electrons between a sharp metal tip and a conducting or semi-conducting sample, when the tip is brought in close proximity to the sample (and a voltage is applied between tip and sample). The exponential dependence of the tunnel current on the tip-sample separation provides very high sensitivity to changes in height of the sample, when scanning the tip laterally along the surface. This way, many surfaces of different crystal lattices were investigated with atomic resolution over the years.

A special advantage of the STM over most diffraction-based methods is the ability to image non-periodic, individual structures. In addition, the STM setup is ideally suited for the investigation of the electrical properties of semiconductors (e.g. band gap[13], doping concentrations[14], surface states[15], and effective masses[16]) by scanning tunneling spectroscopy (STS).[17] Thus, with its unique possibility to investigate the electrical properties with atomic resolution, STM in combination with STS became one of the most important techniques for the investigation of novel semiconductors and semiconductor-based nanostructures.[18]

In this thesis, non-polar III-V semiconductor surfaces are investigated by cross-sectional scanning tunneling microscopy (XSTM) and spectroscopy (XSTS),[19, 20] as well as transmission electron microscopy (TEM), primarily focusing on new physical surface effects that could have a major impact on novel electrical devices. Such devices, e.g. light-emitting diodes and lasers,[21] solar cells,[22] but also high-electron-mobility transistors,[23] are likely to rely on nitride based semiconductors, such as GaN and InN:

Due to the high band gap of approximately 3.4 eV, GaN based *pn*-junctions emit blue or ultra-violet (UV) light, which is used in industry to produce white light emitting diodes.[24] Furthermore, UV-LED sources can be employed for water disinfection.[25] For the invention of the production process needed to create GaN single crystals and especially for the fabrication of *p*-doped GaN crystal layers, Akasaki, Amano, and Nakamura were honored with the Nobel Prize in 2014. But there is still a lot of research to be done in order to improve the crystal quality and thus the power consumption of modern LED lamps (e.g. reduction of dislocations[26] and v-shaped defects [27]). The studies in this thesis on non-polar, *n*-GaN($10\bar{1}0$) surfaces will reveal a polarity depended Fermi-level pinning caused by different charging and discharging rates of an intrinsic surface state that was found in the fundamental band gap of GaN($10\bar{1}0$), recently.[28, 29, 30, 31] Interfaces of electronic devices may exhibit similar effects, crucially affecting the device properties and hence it is important to focus on the analysis of such states.

With a band gap of only $\sim 0.7\,\mathrm{eV}$[32] and an electron affinity of about $5.8\,\mathrm{eV}$,[33] InN exhibits unique properties compared to other nitride based semiconductors. Thus, a variety of potential applications lead to an increasing interest in this material (e.g. deep infrared lasers[34]). Furthermore, by composing an alloy of InN and GaN, the band gap of the resulting semiconductor is tunable from 0.7 to $3.4\,\mathrm{eV}$, depending on the concentration of both materials.[35] This leads to an even larger diversity of potential applications, e.g., multi-stack solar-cells that cover the full spectrum of solar light,[36] InGaN based LEDs,[37], and laser diodes[38] that are already commercially available and used, e.g., in Blu-ray-Disc players ($\lambda = 405\,\mathrm{nm}$). However, it is still difficult to epitaxially grow high quality InN layers. In this thesis the quality of InN layers, grown on GaN will be investigated by combining the advantages of XSTM, XSTS, and TEM. It will be shown that the lattice mismatch of GaN and InN is confined directly at the GaN/InN interface by introducing a dislocation network. Thus, the overgrown InN layer is of highest quality with a low defect concentration. On the cross-sectional m-plane cleavage surface, the interface dislocations induce steps in [0001]-direction in the InN region. These steps lead to an extrinsic pinning of the Fermi level. In contrast to the publications of other groups,[39, 40, 41, 42, 43, 44] it will turn out that an electron accumulation layer caused by intrinsic surface states, cannot be observed on high quality, non-polar *m*-plane InN surfaces. Thus, InN appears to be as conventional as other III-V semiconductors.

Beyond the investigation of nitride based semiconductors, the relatively new technique of photo-excited scanning tunneling spectroscopy is performed on non-polar GaAs(110) surfaces. With this promising technique, surface photo-voltages, local charge carrier distributions, and the influence of non-radiative carrier recombination centers can be probed with atomic resolution.[45, 46, 47, 48, 49, 50, 51, 52, 53] Since the efficiency of solar cell and optoelectronic devices is closely connected to the nanoscale distribution of charge carriers, such effects are detrimental to both the electron-light and light-electron conversion efficiencies in optoelectronic and solar cell devices, respectively. In order to understand the physical processes involved at the atomic scale, the materials used in the device structures need to be investigated simultaneously under illumination and with atomic resolution. However, a fundamental physical understanding and the theoretical modeling of the photo-excited scanning tunneling spectra is still lacking. In this thesis an extended simulation model is developed in order to calculate the band bending, the charge carrier distributions, and hence the tunnel current with and without illumination. A finite difference iteration of the electrostatic potential and the carrier distributions in three dimensions, followed by the calculation of the tunnel current that incorporates light-excited carriers, is used to achieve a quantitative description of

light-excited scanning tunneling spectroscopy for the first time. Furthermore, by comparing photo-excited STS, measured on *p*-GaAs(110) surfaces, with the results of the simulation, one out of two competing physical descriptions[13, 15] of the suppressed accumulation current on *n*-GaAs(110) surfaces will be discarded.

The simulation model developed in this thesis is universally applicable to most semiconductor materials and is not restricted to STS measured under illumination. Hence, it is used for supporting the analysis of the electrical properties of all types of semiconductors investigated in this thesis (i.e. GaAs, GaN, and InN).

Therefore, the thesis summarizes first the current theoretical description of tunneling with emphasis on semiconductors. In Chap. 3, a quantitative model for light-excited tunneling is developed and applied in Chap. 5 to the experimental data measured on GaAs(110) surfaces with the experimental setup and techniques described in Chap. 4. The theoretical description of the tunnel current, developed in Chap. 3 is then also applied to GaN($10\bar{1}0$) surfaces to demonstrate the effect of a polarity depended pinning by the intrinsic surface state (Chap. 6) and to identify the intrinsic properties of the InN($10\bar{1}0$) surface in Chap. 7. Chapter 8 provides a summary and conclusions.

Chapter 2

The theory of tunneling

2.1 The one-dimensional tunneling effect

One of the best known fundamental principles of quantum mechanics is that a free particle (e.g. an electron) with a kinetic energy E can pass a potential barrier V_0 even if $E < V_0$ and thus a transition is classically forbidden.[54] This phenomenon is known as the *tunneling effect* and is described by the wave-particle dualism and the Heisenberg uncertainty principle:[55] The position x and the momentum p of the particle cannot be determined exactly at the same time. Thus, the uncertainties Δx and Δp follow the relation $\Delta x \cdot \Delta p \gtrsim h$ where h is the Planck constant. The statistical nature of the particle is taken into account by a probability density function $|\Psi(x,t)|^2$, which is the square of the absolute value of the wave function $\Psi(x,t)$.

The transmission probability of a particle (e.g. an electron) through a potential barrier can be derived using the time evolution of the particles wave function, given by the time-depended Schrödinger equation. For clarity the one-dimensional case is assumed here in analogy to Ref. [56].

$$-\frac{\hbar^2}{2m_\mathrm{e}}\frac{\partial^2}{\partial x^2}\Psi(x,t) + V(x)\Psi(x,t) = i\hbar\frac{\partial}{\partial t}\Psi(x,t) \tag{2.1}$$

In Eq. 2.1, m_e is the mass of the particle, i is the imaginary unit, and $V(x)$ is the potential energy. In order to investigate the tunneling effect, a rectangular potential barrier is assumed.

$$V(x) = \begin{cases} V_0, & -a < x < a \\ 0, & \text{otherwise} \end{cases} \tag{2.2}$$

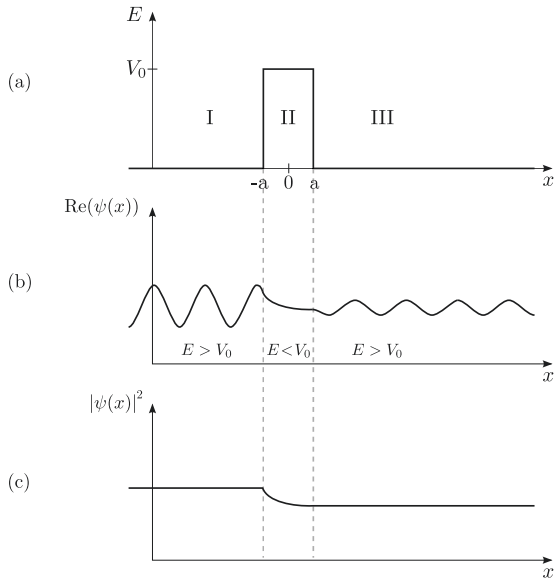

Figure 2.1: The one-dimensional tunneling effect: (a) the one dimensional, time-independent rectangular potential barrier $V(x)$. (b) Real part of the time-independent wave function. (c) The probability density function of the particle's position in real space. Taken from Ref. [57].

The shape of the potential is schematically shown in Fig. 2.1(a).

Eq. 2.1 separates into a spatial and temporal part by using the following time dependence of the wave function.

$$\Psi(x,t) = e^{-i\frac{E}{\hbar}t} \cdot \psi(x) \tag{2.3}$$

Inserting Eq. 2.3 into Eq. 2.1 reveals the eigenvalue equation, commonly known as time independent Schrödinger equation,

$$-\frac{\hbar^2}{2m_\mathrm{e}}\frac{\partial^2}{\partial x^2}\psi(x) + V(x)\psi(x) = E\psi(x) \tag{2.4}$$

where E is the eigenvalue of the energy. For the case of a free particle that tunnels through a energetically forbidden region, Eq. 2.4 is solved by making an ansatz for the wave function separately in each of the three regions: (I) in front of the barrier, (III) behind the barrier, and (II) in the region where $E < V(x)$, as illustrated in Fig. 2.1(b). In the regions I and III, the particle is described as free particle. As

an ansatz, one uses the superposition of the incoming and the reflected wave.

$$\begin{aligned} \psi(x) &= Ae^{ikx} + Be^{-ikx} \\ \text{with } k &= \sqrt{\frac{2\,m_\mathrm{e}}{\hbar^2}E} \end{aligned} \tag{2.5}$$

A and B are the amplitudes of the incoming and reflected wave, respectively. k is the corresponding wave vector. It is the same for the incoming and reflected wave, since the eigenvalue of the energy is not changed by neither the reflection process, nor the tunneling process. A particle that originates from $x = -\infty$ and tunnels from $-a$ to a, has a normalized amplitude $A = 1$. The amplitude of the reflected wave is given by the complex reflection coefficient $B = R$.

Once the particle has reached region III (behind the barrier), it moves away from the barrier to $x = +\infty$. Thus, in region III, the amplitude B for a motion in negative x direction in Eq. 2.5 becomes zero, while A is identified as transmission coefficient T. In summary, one obtains the following wave functions for the region I and III.

$$\begin{aligned} \psi_\mathrm{I}(x) &= e^{ikx} + Re^{-ikx} \\ \psi_\mathrm{III}(x) &= Te^{ikx} \end{aligned} \tag{2.6}$$

The continuity equation in quantum mechanics states that the flux of the probability density $j = \frac{\hbar}{2m_\mathrm{e}i}\left(\Psi^*\frac{\partial\Psi}{\partial x} - \Psi\frac{\partial\Psi^*}{\partial x}\right)$ (where Ψ^* is the conjugate-complex of Ψ) is solenoidal if there is no time dependence of the probability density $|\Psi(x)|^2$:

$$\frac{\partial}{\partial x}\frac{\hbar}{2m_\mathrm{e}i}\left(\Psi^*\frac{\partial\Psi}{\partial x} - \Psi\frac{\partial\Psi^*}{\partial x}\right) = 0 \tag{2.7}$$

Inserting Ψ_I and Ψ_III from Eq. 2.6 into Eq. 2.7 yields the following relationship between the transmission- and the reflection coefficient.

$$|T|^2 + |R|^2 = 1 \tag{2.8}$$

In the second region, which is the region of the barrier, the wave function is given by an exponential decay (argument of the exponential function becomes non-complex).

$$\begin{aligned} \psi_\mathrm{II}(x) &= Ce^{-\kappa x} \\ \text{with } \kappa &= \sqrt{\frac{2\,m_\mathrm{e}}{\hbar^2}\left(V_0 - E\right)} \end{aligned} \tag{2.9}$$

By employing the continuity conditions $\Psi_\mathrm{I}(-a) = \Psi_\mathrm{II}(-a)$ and $\Psi'_\mathrm{I}(-a) = \Psi'_\mathrm{II}(-a)$ as well as $\Psi_\mathrm{II}(a) = \Psi_\mathrm{III}(a)$ and $\Psi'_\mathrm{II}(a) = \Psi'_\mathrm{III}(a)$, the amplitudes C, R, and T can be

obtained. The transmission coefficient $T(E)$ is of particular importance, because $|T(E)|^2$ is the tunneling probability of the particle.[56]

$$T(E) = \mathrm{e}^{-2ika} \frac{2\,k\kappa}{2\,k\kappa\cosh(2\,\kappa a) - i(k^2\,-\kappa^2)\sinh(2\,\kappa a)} \tag{2.10}$$

$$|T(E)|^2 = \frac{1}{1\;+\frac{V_0^2}{4E(V_0-E)}\sinh^2(2\kappa a)} \tag{2.11}$$

Equations 2.10 and 2.11 hold for $E < V_0$ and exhibit values greater than zero for finite values of V_0. Thus, a particle, which exhibits a kinetic energy lower than the barrier potential, has a non-zero probability to overcome this barrier. If the barrier potential tends to infinity, $|T(E)|^2$ becomes zero and the classical limit is reached.

2.2 A one-dimensional approach to the scanning tunneling microscope

Although the one-dimensional tunneling effect is a rudimentary description and hence a strong simplification, ignoring for example the three-dimensional structure of the tip and the influence of a quantum mechanical many-body system, one can already deduce some fundamental properties of the tip-vacuum-sample system. For this purpose, region I in Fig. 2.1(a) is assigned to the metallic sample, region II to the vacuum, and region III to the tip of the scanning tunneling microscope, as schematically shown in Fig. 2.2. In the latter figure, dark shaded areas correspond to occupied states, while light shaded areas indicate unoccupied states. The height of the potential barrier V_0 in region II is given by the work function of the metal Φ, which is defined as the amount of energy needed to extract an electron from the material (at the Fermi-level) into the vacuum. Φ is assumed to be equal for both, tip and sample in this particular case.

When the tip is brought in proximity to the sample, the Fermi-levels are equalized. A tunnel current arises, if an additional voltage V between tip and sample is applied, which shifts the Fermi-level of the tip by $e{\cdot}V$ relative to the Fermi-level of the sample E_F. (In this model one assumes that $e{\cdot}V \ll \Phi$ [58] and hence that the tunnel barrier is not affected by the applied voltage for the reason of simplification.) A shift of the Fermi-energy means that the electronic states of the tip in the energy range from $E_\mathrm{F} + e \cdot V$ to E_F are unoccupied. Hence, electrons in a sample state Ψ_n with an energy eigenvalue E_n within this range, can tunnel from the sample into the tip.[58]

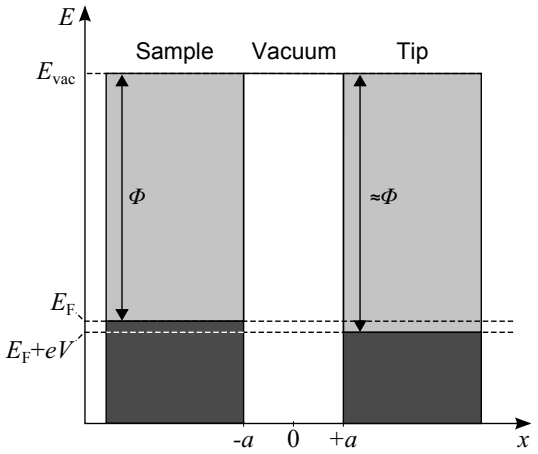

Figure 2.2: Schematic energy diagram of a sample-vacuum-tip system where region I in Fig. 2.1(a) is assigned to the metallic sample, region II to the vacuum, and region III to the tip of the scanning tunneling microscope. Dark shaded areas correspond to occupied states, while light shaded areas indicate unoccupied states. The height of the potential barrier V_0 in region II is given by the work function of the metal Φ. In this model one assumes that $e \cdot V \ll \Phi$ [58] and hence that the tunnel barrier is not affected by the applied voltage for the reason of simplification. A tunnel current arises, if an additional voltage V between tip and sample is applied, which shifts the Fermi-level of the tip by $e \cdot V$ relative to the Fermi-level of the sample E_F.

(Note, Ψ_n denotes the n-th sample state of a finite sample (particle in a box). If a free particle (infinitively large sample) is assumed, n becomes continuous.)

The tunnel current is proportional to the sum of the transmission probabilities of all states of the sample within the range from $E_F + e \cdot V$ to E_F. [58]

$$I \propto \sum_{E_n=E_F+eV}^{E_F} |T(E_n)|^2 = \sum_{E_n=E_F+eV}^{E_F} |\Psi_n(x=a)|^2 \tag{2.12}$$

The *local density of states* at an energy E and a position x is defined by [58]

$$\rho_{LDOS}(x,E) = \frac{1}{\epsilon} \sum_{E_n=E-\epsilon}^{E} |\psi_n(x)|^2 \tag{2.13}$$

where ϵ is a small energy interval. Assuming that the local density of states is nearly

constant within the energy range $[E_\mathrm{F} + eV, E_\mathrm{F}]$, Eq. 2.12 can be transformed into

$$I \propto V \cdot \rho_\mathrm{LDOS}(x{=}a, E{=}E_\mathrm{F}) \tag{2.14}$$

Note that $\rho_\mathrm{LDOS}(a, E_\mathrm{F})$ is evaluated at the position $x{=}a$, where the surface of the tip is located. The probability density of sample states $|\Psi_\mathrm{n}(x)|^2$ exponentially decays in the region of the vacuum barrier (cf. Eq. 2.9 and Fig. 2.1(c)) according to Eq. 2.15.

$$|\psi_\mathrm{n}(x{=}a)|^2 = |\psi_\mathrm{n}(x{=}{-}a)|^2 \cdot e^{-4\kappa a} \tag{2.15}$$

where $2a$ is the total barrier width or the tip-sample separation, respectively. Substituting Eq. 2.15 into Eq. 2.13 gives the local density of states at the surface of the sample.

$$\rho_\mathrm{LDOS}(x{=}{-}a, E_\mathrm{F}) = \frac{1}{\epsilon} \sum_{E_\mathrm{n}=E_\mathrm{F}-\epsilon}^{E_\mathrm{F}} |\psi_\mathrm{n}(x{=}a)|^2 \cdot e^{4\kappa a} \tag{2.16}$$

Assuming a constant local density of states in the interval $[E_\mathrm{F} + eV, E_\mathrm{F}]$ (which means that $\epsilon = eV$) and small voltages V (which means that $e^{4\kappa a}$ does not vary significantly), the exponential term in Eq. 2.16 can be written in front of the sum.

$$\rho_\mathrm{LDOS}(x{=}{-}a, E_\mathrm{F}) = \frac{e^{4\kappa a}}{eV} \sum_{E_\mathrm{n}=E_\mathrm{F}+e\cdot V}^{E_\mathrm{F}} |\psi_\mathrm{n}(x{=}a)|^2 = \rho_\mathrm{LDOS}(x{=}a, E_\mathrm{F}) \cdot e^{4\kappa a} \tag{2.17}$$

Finally, the tunnel current can be derived using the local density of states at the surface of the sample $\rho_\mathrm{LDOS}(-a, E_\mathrm{F})$ by substituting Eq. 2.17 into Eq. 2.14. [58]

$$I \propto V \cdot \rho(x{=}-a, E{=}E_\mathrm{F}) \cdot e^{-4\kappa a} \tag{2.18}$$

Eq. 2.18 shows a proportionality of the tunneling current to the local density of states at the sample $\rho(-a, E_\mathrm{F})$ and the applied voltage V. Furthermore, it depends exponentially on the tip-sample separation $2a$. This dependence is crucial for the operating principle of the scanning tunneling microscope, because a small variation of the tip-sample separation, caused e.g. by the shape of the local density of states of a single atom, results in an exponential variation of the tunnel current. This dependence can be estimated more precisely as follows. For small voltages, the decay constant κ, as given by Eq. 2.9, is a function of Φ, only. [58]

$$\kappa = \frac{\sqrt{2m_\mathrm{e}\Phi}}{\hbar} \approx 0.5\sqrt{\Phi\,[\mathrm{eV}]}\ \mathrm{\AA}^{-1} \tag{2.19}$$

With a typical work function of $\Phi = 4\,\mathrm{eV}$, a value of $1\,\mathrm{\AA}^{-1}$ is obtained for κ. Due

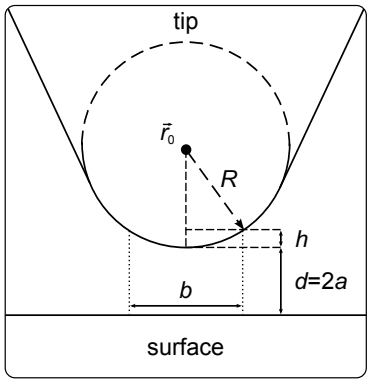

Figure 2.3: Schematic picture of the tip-sample geometry, adapted from Ref. [58, 59]. The tip is assumed to be locally spherical with radius R, while $d = 2a$ is the tip-sample separation.

to the exponential dependence $\exp(-2\kappa 2a)$ of the tunnel current in Eq. 2.18, this value of κ leads to a decay of I proportional to $e^2 \approx 7.4$ per Å.[58] Thus, as a general rule, the tunnel current is reduced by approximately one order of magnitude, when the tip-sample separation is increased by one Ångström.[58]

As final remark in this section, the lateral resolution of the scanning tunneling microscope is discussed. Binnig proposed that the smallest feature that is resolved by the tunneling microscope has to be much smaller than the area πR^2 with R being the radius of spherically shaped tip.[58] Due to the spherical shape, only the tip-sample separation of the outermost part of the tip (tip apex) is significantly determining the tunnel current, as illustrated in Fig. 2.3. When the tip radius R is large compared to the tip-sample separation $d = 2a$, the electric flux lines (and hence, the spatial direction of the tunnel current) can be assumed to be perpendicular to the surface.[58] Hence, the tunnel current is determined by perpendicular tip-sample separations $d + h$, only. Under this assumption, the change of the tip-sample separation h for a point that is located at a distance of $b/2$ from the tip apex is given by

$$h = \frac{(b/2)^2}{2R} \tag{2.20}$$

When h is in the order of 1 Å, the tunnel current at the corresponding position $b/2$ is already one order of magnitude smaller compared to the tunnel current at the tip apex. For a tip radius of 1000 Å(and $h = 1$ Å), the relevant contributions to the tunnel current are concentrated in an area with a diameter of $b \approx 90$ Å.[58]

2.3 Quantitative description of the tunnel current

2.3.1 Bardeen's tunnel current theory

Although it is easy to get some very important information about the tunnel current from the one-dimensional tunneling effect, as presented in the previous section, much more effort is required to end up with a quantitative description. The goal here is to calculate the transition probabilities of an electron that tunnels from an occupied state (i.e. inital state) of the sample to (multiple) empty states of the tip at the same energy (elastic tunneling). These probabilities are added up. The result is summed over all possible initial states. Finally, by multiplying the elementary charge e to this double sum, the total tunnel current is obtained. The derivation of this tunnel current can be found in Ref. [60], but there is a more illustrative and elaborate version of the same derivation given by Ref. [61]. In principle, Bardeen assumed the electron-electron interaction of the many-particle system to be negligible (i.e. electrons in the system are described by the single-electron Hamiltonian H).[61] Furthermore, Bardeen suggested to divide the system into two subsystems, where the Hamiltonian used in the Schrödinger equation $H\Psi = E\Psi$ is defined differently in each of the systems.[58] This is shown in Fig. 2.4: The first subsystem is given by the left metal and the potential barrier ($x < +a$). In this system Φ_i and $\epsilon_\mathrm{l,i}$ are the eigenfunctions and the eigenvalues of the Hamiltonian H_l, respectively (i.e. $H_\mathrm{l}\Phi_\mathrm{i} = \epsilon_\mathrm{l,i}\Phi_\mathrm{i}$). Right to this region ($x > +a$) the eigenfunctions Φ_i tend to zero. This can be achieved by, e.g., defining the potential in H_l to be zero for $x < -a$ and a constant V_0 for $x > -a$. Similarly, the second subsystem is defined by the right metal and the potential barrier ($x > -a$). In this region, χ_k and $\epsilon_\mathrm{r,k}$ are the eigenfunctions and the eigenvalues of H_r, respectively (i.e. $H_\mathrm{r}\chi_\mathrm{k} = \epsilon_\mathrm{r,k}\chi_\mathrm{k}$). Again, all the χ_k fall to zero left to the barrier.[60] A solution Ψ of the Hamiltonian H is a linear combination of the eigenstates Φ_i and χ_k, respectively.

Following this approach, Bardeen could tread the electronic states of the tip and the sample independently and the Hamiltonian H of the composite system is not required explicitly.[61] Tunneling is described by the transition from an initial state $\Psi_\mu = \Psi(t = 0)$ to a final state $\Psi_\nu = \Psi(t = \infty)$. Note the first order perturbation theory used by Bardeen is only valid for small times t. However, one is rather interested in the transition rate from $\mu \to \nu$ than in the precise knowledge of the final state Ψ_ν. At the beginning ($t = 0$), an electron with energy E is assumed to be located at the left metal. Thus, $\Psi = \Psi(t = 0) = \Psi_\mu$ is represented by Φ_i (or a linear combination of those states) and it is $H_\mathrm{l}\Psi = E\Psi$. Without transition

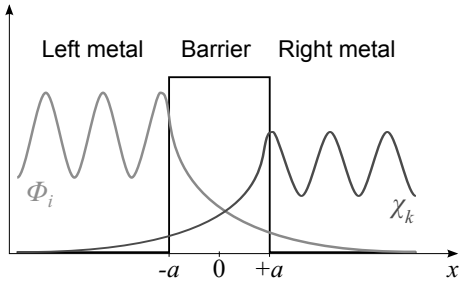

Figure 2.4: Schematic view of the two subsystems, where the Hamiltonian used in the Schrödinger equation $H\Psi = E\Psi$ is defined differently, depending on the position. The first subsystem is given by the left metal and the potential barrier ($x < +a$). In this system Φ_i and $\epsilon_{\mathrm{l,i}}$ are the eigenfunctions and the eigenvalues of the Hamiltonian H_l, respectively (i.e. $H_\mathrm{l}\Phi_\mathrm{i} = \epsilon_{\mathrm{l,i}}\Phi_\mathrm{i}$). Right to this region ($x > +a$) the eigenfunctions Φ_i tend to zero. This can be achieved by, e.g., defining the potential in H_l to be zero for $x < -a$ and a constant V_0 for $x > -a$. Similarly, the second subsystem is defined by the right metal and the potential barrier ($x > -a$). In this region, χ_k and $\epsilon_{\mathrm{r,k}}$ are the eigenfunctions and the eigenvalues of H_r, respectively (i.e. $H_\mathrm{r}\chi_\mathrm{k} = \epsilon_{\mathrm{r,k}}\chi_\mathrm{k}$). Again, all the χ_k fall to zero left to the barrier.[60]

(no tunneling), the time evolution of this state would be given by $\Psi(t) = \Psi \cdot \exp(-i/\hbar Et)$. For weak tunneling and small t, the time evolution is given by[61]

$$\Psi(t) = \Psi \cdot \exp\left(-\frac{i}{\hbar}Et\right) + \sum_{k'} a_{\mathrm{k'}}(t)\chi_{\mathrm{k'}} \tag{2.21}$$

with $a_{\mathrm{k'}}$ being the linear combination coefficients of the bounded eigenstates of H_r.[61] Furthermore $a_{\mathrm{k'}}(t = 0)$ equals zero. According to Eq. 2.21, the transition probability $|\langle\chi_\mathrm{k}|\Psi(t)\rangle|^2$ between the state $\Psi(t)$ and the final eigenstate χ_k is defined by the following relation.[61]

$$\langle\chi_\mathrm{k}|\Psi(t)\rangle = a_\mathrm{k}(t) + \langle\chi_\mathrm{k}|\Psi\rangle\exp\left(-\frac{i}{\hbar}Et\right) \tag{2.22}$$

Note that the states Φ_i and χ_k are not orthogonal, since they are solutions of two different Hamiltonians. However, in Eq. 2.22 they are assumed to be nearly orthogonal and hence $\langle\chi_\mathrm{k}|\Psi\rangle$ is small compared to $a_\mathrm{k}(t)$.[61] Then, the transition

rate is given by[61]

$$\frac{d}{dt}\sum_{k}\left|\langle\chi_{\mathrm{k}}|\Psi(t)\rangle\right|^{2}\approx\frac{d}{dt}\sum_{k}\left|a_{\mathrm{k}}\right|^{2} \tag{2.23}$$

Thus, one has to determine the coefficients a_{k} by substituting Eq. 2.21 into the time-depended Schrödinger equation and applying first order perturbation theory (due to the different Hamiltonians used in the two subsystems). This results in a differential equation for the a_{k} which has the solution[61]

$$a_{\mathrm{k}}(t)=\frac{4\sin^{2}\left(t\left[\epsilon_{\mathrm{r,k}}-E\right]/(2\hbar)\right)}{\left(\epsilon_{\mathrm{r,k}}-E\right)^{2}}\langle\chi_{\mathrm{k}}|H-H_{\mathrm{l}}|\Psi\rangle \tag{2.24}$$

The bra-ket term in Eq. 2.24 is identified as the matrix element $M(\chi_{\mathrm{k}},\Psi)$ for the transition from the initial state Ψ of the left metal to the k-th eigenstate state of the right metal χ_{k}. Inserting Eq. 2.24 into Eq. 2.23 gives

$$\frac{d}{dt}\sum_{k}\left|a_{\mathrm{k}}\right|^{2}=\frac{d}{dt}\sum_{k}P_{\mathrm{t}}(\epsilon_{\mathrm{r,k}}-E)|M(\chi_{\mathrm{k}},\Psi)|^{2} \tag{2.25}$$

with $P_{\mathrm{t}}(\epsilon_{\mathrm{r,k}}-E)=4\sin^{2}\left(t\left[\epsilon_{\mathrm{r,k}}-E\right]/(2\hbar)\right)/\left(\epsilon_{\mathrm{r,k}}-E\right)^{2}$. The function $P_{\mathrm{t}}(W)$ (axially symmetrical, always ≥ 0) has its highest peak at $W=\epsilon_{\mathrm{r,k}}-E=0$ and its first minima at $\pm 2h/t$. The area enclosed by the function $P_{\mathrm{t}}(W)$ and the energy axis can be approximated by an integration from $-2h/t$ to $2h/t$.[61] Outside this interval, $P_{\mathrm{t}}(W)$ is approximated to be zero. Since $\pm 2h/t$ tends to zero for larger t, the matrix element can be averaged for the states χ_{k} with the eigenvalues $\epsilon_{\mathrm{r,k}}$ in the interval $[E-2h/t, E+2h/t]$:[61]

$$M^{2}(\Psi)=\frac{1}{N_{\mathrm{r}}}\sum_{k:|\epsilon_{\mathrm{r,k}}-E|<2h/t}\left|\langle\chi_{\mathrm{k}}|H-H_{\mathrm{l}}|\Psi\rangle\right|^{2} \tag{2.26}$$

with N_{r} being the number of states in the right metal which exhibit energies within the interval defined above. With the help of Eqs. 2.26 and 2.25 one can find the following approximation of Eq. 2.23.[61]

$$\begin{aligned}\frac{d}{dt}\sum_{k}P_{\mathrm{t}}(\epsilon_{\mathrm{r,k}}-E)|M(\chi_{\mathrm{k}},\Psi)|^{2}&\approx\frac{d}{dt}M^{2}(\Psi)\sum_{k:|\epsilon_{\mathrm{r,k}}-E|<2h/t}P_{\mathrm{t}}(\epsilon_{\mathrm{r,k}}-E)\\&\approx\frac{d}{dt}M^{2}(\Psi)\rho_{\mathrm{r}}(E)\int_{-2h/t}^{2h/t}dE'P_{\mathrm{t}}(E')=\frac{2\pi}{\hbar}M^{2}(\Psi)\rho_{\mathrm{r}}(E)\end{aligned} \tag{2.27}$$

$\rho_{\mathrm{r}}(E)=\frac{\partial N_{\mathrm{r}}}{\partial E}$ is the number of states per unit energy of the right metal. Hence, the transition rate from an initial state at the left metal to final states in the right

metal is given by the right hand side of Eq. 2.27, which is commonly known as *Fermi's Golden Rule*.

As mentioned at the beginning of this section, the tunnel current is given by e times the sum of the transition probabilities of electrons that tunnel from an occupied state of the left metal to empty states of the right metal at the same energy. Thus, the sum of the transition probabilities over all initial states Φ_i has to be multiplied by the *Fermi-Dirac distribution* $f(E) = (1 + \exp[(E - E_\mathrm{F})/(kT)])^{-1}$ for the occupation probability of the left metal and by $1 - f(E)$ for the probability of finding an unoccupied state in the right metal. Thus, the tunnel current is given by

$$I = \frac{2\pi}{\hbar} e \cdot \sum_\mathrm{i} f(\epsilon_{\mathrm{l,i}}) \cdot [1 - f(\epsilon_{\mathrm{l,i}} + eV)] \cdot M^2(\Phi_i) \cdot \rho_\mathrm{r}(\epsilon_{\mathrm{l,i}}) \tag{2.28}$$

with the tip-sample voltage V that shifts the Fermi-level of the right metal by eV, as mentioned above (see e.g. Fig. 2.2). For the case of low temperatures T, the two Fermi-Dirac distributions in Eq. 2.28 become step functions and thus the terms of the sum are nonzero only for an energy interval of $[E_\mathrm{F}, E_\mathrm{F} + eV]$. Hence, Eq. 2.28 can be approximated by Eq. 2.29 in the limit of $T \to 0$.

$$I = \frac{2\pi}{\hbar} e \cdot \sum_{i:E_\mathrm{F} < \epsilon_{\mathrm{l,i}} < E_\mathrm{F} + eV} M^2(\Phi_\mathrm{i}) \cdot \rho_\mathrm{r}(\epsilon_{\mathrm{l,i}}) \tag{2.29}$$

In analogy to Eq. 2.26, $M^2(\Phi_\mathrm{i})$ can be averaged for small voltages V and Eq. 2.29 is changed into[61]

$$I = \frac{2\pi}{\hbar} e \cdot \int_{E_\mathrm{F}}^{E_\mathrm{F} + eV} \rho_\mathrm{r}(E') \rho_\mathrm{l}(E') T(E') dE' \tag{2.30}$$

with the number of states per unit energy of the left metal, $\rho_\mathrm{l}(E)$. The averaged matrix element T is given by $T(E) = \frac{1}{N_\mathrm{l}} \sum_{i:|\epsilon_{\mathrm{l,i}} - E'| < \eta} M^2(\Phi_\mathrm{i})$, where N_l is the number of states in the left metal in an energy interval of $[\epsilon_{\mathrm{l,i}} - \eta, \epsilon_{\mathrm{l,i}} + \eta]$. η is chosen such that the energies of the states in the interval are distributed nearly equidistantly.[61]

In the limit of small voltages, the number of states N_l can be assumed to be constant and hence is approximated by $N_\mathrm{l} = eV \cdot \rho_l(E_\mathrm{F})$. For the same reason, the integral in Eq. 2.30 can be approximated by[61]

$$I = \frac{2\pi}{\hbar} e \cdot \rho_\mathrm{r}(E_\mathrm{F}) \rho_\mathrm{l}(E_\mathrm{F}) T(E_\mathrm{F}) \cdot eV \tag{2.31}$$

and by substituting $T(E_\mathrm{F}) = (eV \cdot \rho_\mathrm{l}(E_\mathrm{F}))^{-1} \sum_{i:|\epsilon_{\mathrm{l,i}} - E'| < \eta} M^2(\Phi_\mathrm{i})$ into Eq. 2.31, the

tunnel current in the limit of small voltages and small temperatures is given by Eq. 2.32.

$$I = \frac{2\pi}{\hbar} e \cdot \rho_{\mathrm{r}}(E_{\mathrm{F}}) \sum_{i:|\epsilon_{\mathrm{l,i}} - E_{\mathrm{F}}| < \eta} M^2(\Phi_{\mathrm{i}}) \tag{2.32}$$

At last, one has to determine the matrix elements $\langle \chi_{\mathrm{k}} | H - H_{\mathrm{l}} | \Phi_{\mathrm{i}} \rangle$ such that they are suitable for numerical calculations. Utilizing the fact that $H - H_{\mathrm{l}}$ is the zero operator at the region of the left metal, while $H - H_{\mathrm{r}}$ is the zero operator at the right metal and by the application of Gauss's theorem[61], Bardeen showed[60] that the matrix element can be approximated by the integral over an arbitrary surface $d\vec{S}$ that separates the left metal from the right metal.

$$M(\chi_{\mathrm{k}}, \Phi_{\mathrm{i}}) = -\frac{\hbar^2}{2m_{\mathrm{e}}} \int \Phi_{\mathrm{i}}^* \nabla \chi_{\mathrm{k}} - \chi_{\mathrm{k}} \nabla \Phi_{\mathrm{i}}^* \, d\vec{S} \tag{2.33}$$

Equation 2.33 depends on the overlap of the wave functions χ_{k} and Φ_{i} of the left and the right metal, only. It is independent of the Hamiltonian of the system.

2.3.2 The Tersoff-Hamann model

The approximation for the matrix element derived by Bardeen requires the knowledge of the wave functions of the tip-vacuum-sample system. Especially the dependence of the tunnel current on the tip's wave function posed serious problems, since each tip exhibits an individual shape and thus a different wave function. Furthermore, the density of states of the tip is usually unknown. In order to overcome these problems, Tersoff and Hamann (1983) suggested that the tip's wave functions can be modeled, in a first approach, as radially symmetrical due to the spherical form of the tip apex, as shown in Fig. 2.3. Furthermore, they assumed that tunneling into and out of the localized s-orbitals of the tip's foremost atoms dominates all other tunnel processes (i.e. tunneling into and out of p, sp^3, and d-orbitals is neglected). Then the tip's wave functions (outside the tip region[61]) are given by[62, 59]

$$\Psi_{\mathrm{t}}(\vec{r}) = \Omega_{\mathrm{t}}^{-\frac{1}{2}} c_{\mathrm{t}} \kappa R e^{\kappa R} (\kappa \, |\vec{r} - \vec{r}_0|)^{-1} e^{-\kappa |\vec{r} - \vec{r}_0|} \tag{2.34}$$

where Ω_{t} is the tip's volume and, according to Fig. 2.3, R and $\vec{r}_0$ are the radius and the center of the sphere at the tip apex, respectively. The constant c_{t} depends on the tip geometry, the electronic structure, and the tip-vacuum boundary conditions.[62] $\kappa_{\mathrm{t}} = \frac{1}{\hbar}\sqrt{2m_{\mathrm{e}}(\Phi - (E_{\mathrm{t}} - E_{\mathrm{F}}))}$ is the inverse decay length of the wave function in vacuum with E_{t} being the eigenvalue of the eigenstate Ψ_{t} and Φ being the work function of the metal. κ is again approximated by $\frac{1}{\hbar}\sqrt{2m_{\mathrm{e}}\Phi}$ for small voltages.

Tersoff and Hamann used an expansion of the sample's surface wavefunctions $\Psi_s(x, \vec{s})$ in the region of negligible potential[62]

$$\Psi_s(\vec{r}) = \Omega_s^{-\frac{1}{2}} \sum_G a_G e^{-(\kappa^2 + \left|\vec{k}_\parallel + \vec{G}\right|^2)^{1/2} x} \cdot e^{i(\vec{k}_\parallel + \vec{G})\cdot \vec{s}} \tag{2.35}$$

where Ω_s is the sample's volume, $\vec{G}$ is the reciprocal surface lattice vector, and $\vec{k}_\parallel$ is the surface Bloch wave vector.[62] The two-dimensional surface vector $\vec{s}$ is composed of the second and third component of $\vec{r}$, while x corresponds to the first component. The eigenvalues of Ψ_s are denoted by E_s. By substituting Eqs. 2.34 and 2.35 into Eq. 2.33, the tunnel matrix element can be obtained

$$M(\Psi_\mathrm{t}(\vec{r}), \Psi_\mathrm{s}(\vec{r})) = -\frac{\hbar^2}{2m_\mathrm{e}} 4\pi\kappa^{-1}\Omega_\mathrm{t}^{-1/2}\kappa R e^{\kappa R}\Psi_\mathrm{s}(\vec{r}_0) \tag{2.36}$$

and finally, by assigning the wave function of the left metal Φ_i in Eq. 2.32 to the sample's wave function Ψ_s and the wave function of right metal χ_k to Ψ_t and by substituting Eq. 2.36 into Eq. 2.32, Bardeen's tunnel current in the Tersoff-Hamann approximation is given by

$$\begin{aligned}
I &= \frac{2\pi}{\hbar} e \cdot \rho_\mathrm{t}(E_\mathrm{F}) \sum_{s:|E_\mathrm{s}-E_\mathrm{F}|<\eta} M^2(\Psi_\mathrm{s}) \\
&= \frac{2\pi}{\hbar} e \cdot \rho_\mathrm{t}(E_\mathrm{F}) \sum_{s:|E_\mathrm{s}-E_\mathrm{F}|<\eta} \frac{1}{N_\mathrm{t}} \sum_{t:|E_\mathrm{t}-E_\mathrm{F}|<2h/t} \frac{\hbar^4}{m_\mathrm{e}^2}\frac{4\pi^2}{\Omega_\mathrm{t}} R^2 e^{2\kappa R} \left|\Psi_\mathrm{s}\left(\vec{r}_0\right)\right|^2 \\
&= \frac{8\pi^3}{m_\mathrm{e}^2}\hbar^3\Omega_\mathrm{t}^{-1} R^2 e \rho_\mathrm{t}(E_\mathrm{F}) e^{2\kappa R} \sum_{s:|E_\mathrm{s}-E_\mathrm{F}|<\eta} \left|\Psi_\mathrm{s}\left(\vec{r}_0\right)\right|^2 \frac{1}{N_\mathrm{t}} \sum_{t:|E_\mathrm{t}-E_\mathrm{F}|<2h/t} 1 \\
&= \frac{8\pi^3}{m_\mathrm{e}^2}\hbar^3\Omega_\mathrm{t}^{-1} R^2 e \rho_\mathrm{t}(E_\mathrm{F}) e^{2\kappa R} \sum_{s:|E_\mathrm{s}-E_\mathrm{F}|<\eta} \left|\Psi_\mathrm{s}\left(\vec{r}_0\right)\right|^2 \\
&= \frac{32\pi^3}{\hbar} R^2\Phi^2\kappa^{-4} e \rho_\mathrm{t}(E_\mathrm{F})\Omega_\mathrm{t}^{-1} e^{2\kappa R} \sum_{s:|E_\mathrm{s}-E_\mathrm{F}|<\eta} \left|\Psi_\mathrm{s}\left(\vec{r}_0\right)\right|^2
\end{aligned} \tag{2.37}$$

On the right hand side of Eq. 2.37 the term $\kappa = \hbar^{-1}\sqrt{2m_\mathrm{e}\Phi}$ was used to eliminate m_e from the equation. By introducing the density of states (number of states per unit energy and unit volume) $D_\mathrm{t}(E) = \rho_\mathrm{t}/\Omega_\mathrm{t}$ and using the average value of the sum for small voltages, such that $\eta \approx eV$, one ends up in the relation, originally found by Tersoff and Hamann.[62]

$$I = 32\pi^3\hbar^{-1}e^2 V\Phi^2 D_t(E_\mathrm{F}) R^2\kappa^{-4} e^{2\kappa R} \cdot \sum_s \left|\Psi_s(\vec{r}_0)\right|^2 \delta(E_\mathrm{s} - E_\mathrm{F}) \tag{2.38}$$

Due to the Dirac distribution, the sum in equation 2.38 only has nonzero terms for states that exhibit an energy equal to E_F. Thus, it is identified as the sample's local density of states per unit volume at the center $\vec{r}_0$ of the tip's sphere and per unit energy near the Fermi-energy $D_\mathrm{s}(\vec{r}_0, E_\mathrm{F})$. Thus, the tunnel current in the Tersoff-Hamann approximation is proportional to the applied tip-sample voltage, multiplied by the local density of states of the sample at the position of the center of the tip's sphere.

$$I \propto V \cdot D_\mathrm{s}(\vec{r}_0, E_\mathrm{F}) \tag{2.39}$$

With their approximation, Tersoff and Hamann were able to quantitatively explain the periodicity of the Au(110) 2×1 reconstructed surface[62] that was measured by Binnig and Rohrer.[63] As a drawback, this model cannot explain the atomic resolution of the STM on most surfaces. In 1989, Ohnishi and Tsukada[64] showed that the highly directional $\mathrm{d_z}$ orbitals of the tungsten tip are significantly influencing the tunnel current and hence can account for atomic resolution.

2.3.3 Harrison's approximation of Bardeen's tunnel current

The tunnel current computations in this thesis are based on a model developed by Bono and Good[65] as well as Feenstra and Stroscio[66]. However, this model originates in the tunnel current approximation derived by Harrison[67] in 1961. He described a methodology for the construction of wave functions through regions of varying band structures and derived the transition-probabilities for tunneling with the help of Bardeen's transition matrix element (Eq. 2.33). For the tunneling process, the conservation of the transverse wave vector $\vec{k}_\parallel$ (parallel to the interface plane between energetically allowed regions and the tunnel barrier) as well as the conservation of the particle's energy is applied.

First of all, Harrison considered a system composed of two regions with different (but known) band structures. The interface plane between both regions is assumed to be at the position $x = 0$.[67] The wave function of the entire system is modeled by the superposition of an incoming and an outgoing Bloch wave on each side (left hand side: ϕ_l, right hand side: ϕ_r). All wave functions exhibit the same parallel wave vector $\vec{k}_\parallel$. In the following, the Bloch wave functions are represented by plane waves with the same wave vector k_x.[67] Let ϕ be the linear combination of plane wave functions that represents a linear combination of Bloch wave functions. While the Bloch wave functions are matched at all boundaries, the corresponding plane waves ϕ and their derivatives with respect to x may be discontinuous at these points. With the introduction of the functions $\alpha(E, \vec{k}_\parallel)$ and $\beta(E, \vec{k}_\parallel)$, generalized

boundary conditions that hold even for discontinuous wave functions can be found: [67]

$$\begin{aligned} \phi_\mathrm{l} &= \beta\phi_\mathrm{r} \\ \frac{\partial\phi_\mathrm{l}}{\partial x} &= \alpha\frac{\partial\phi_\mathrm{r}}{\partial x} \end{aligned} \tag{2.40}$$

Using this approach, Harrison found a generalized form of the probability density current J_x that is conserved at all boundaries between different band structures. [67]

$$J_\mathrm{x} = \frac{\hbar}{2m_\mathrm{e}i}\left(\phi^*\alpha\frac{\partial}{\partial x}\beta\phi - \phi\alpha\frac{\partial}{\partial x}\beta\phi^*\right) \tag{2.41}$$

The conservation properties of Eq. 2.41 can be easily proven. The probability density current near the interface $x = 0$ is given by:

$$\begin{aligned} J_{x>0} &= \frac{\hbar}{2m_\mathrm{e}i}\left(\phi_\mathrm{r}^*\alpha\frac{\partial}{\partial x}\beta\phi_\mathrm{r} - \phi_\mathrm{r}\alpha\frac{\partial}{\partial x}\beta\phi_\mathrm{r}^*\right) \\ &= \frac{\hbar}{2m_\mathrm{e}i}\left(\phi_\mathrm{r}^*\alpha\left(\beta\frac{\partial\phi_\mathrm{r}}{\partial x} + \phi_\mathrm{r}\frac{\partial\beta}{\partial x}\right) - \phi_\mathrm{r}\alpha\left(\beta\frac{\partial\phi_\mathrm{r}^*}{\partial x} + \phi_\mathrm{r}^*\frac{\partial\beta}{\partial x}\right)\right) \\ &= \frac{\hbar}{2m_\mathrm{e}i}\left(\phi_\mathrm{r}^*\beta\alpha\frac{\partial\phi_\mathrm{r}}{\partial x} - \phi_\mathrm{r}\beta\alpha\frac{\partial\phi_\mathrm{r}^*}{\partial x}\right) \\ &= \frac{\hbar}{2m_\mathrm{e}i}\left(\phi_\mathrm{l}^*\frac{\partial}{\partial x}\phi_\mathrm{l} - \phi_\mathrm{l}\frac{\partial}{\partial x}\phi_\mathrm{l}^*\right) \\ &= J_{x<0} \end{aligned} \tag{2.42}$$

By comparing Eq. 2.41 with $J_\mathrm{x} = \rho v_\mathrm{x}$, where $\rho = \phi^*\phi$ is the probability density, one finds a relation between the group velocity v_x and the wave vector $k_\mathrm{x} = \left|\vec{k}_\perp\right|$:

$$v_\mathrm{x} = \hbar\alpha\beta\frac{k_\mathrm{x}}{m_\mathrm{e}} \tag{2.43}$$

On the other hand, v_x is given by the derivation of the dispersion relation with respect to the wave vector:[67]

$$v_\mathrm{x} = \frac{\partial H}{\partial p_\mathrm{x}} = \frac{1}{\hbar}\frac{\partial E}{\partial k_\mathrm{x}} \tag{2.44}$$

Solving Eq. 2.43 and Eq. 2.44 with respect to $\alpha\beta k_\mathrm{x}$ yields Eq. 2.45 that determines the boundary parameters α and β and thus the wave functions in the region where

the band structure is discontinuously changed [67]

$$\alpha\beta k_{\mathrm{x}} = \frac{m_{\mathrm{e}}}{\hbar^2}\frac{\partial E}{\partial k_{\mathrm{x}}} \tag{2.45}$$

For regions exhibiting constant band structures, the evolution of ϕ with respect to x can be deduced from the Schrödinger equation[67]

$$\frac{\partial^2\phi}{\partial x^2} + k_{\mathrm{x}}^2\phi = 0 \tag{2.46}$$

with $k_{\mathrm{x}}^2 = (2m_{\mathrm{e}})/\hbar^2\,(E-V) - |\vec{k}_{\parallel}|^2$. In principle, ϕ depends on all three spatial direction x, y, z. Since the tunneling process takes place along the x direction, and $\vec{k}_{\parallel}$ is conserved, Harrison focused on the evolution of ϕ along the x component, only. In the limit of continuously varying band structure (i.e. in the limit of many interface planes of discontinuous band structure regions located close to each other) the differential equation 2.46 becomes [67]

$$\beta\frac{\partial}{\partial x}\frac{\alpha}{\beta}\frac{\partial}{\partial x}\beta\phi + \beta\alpha k_{\mathrm{x}}^2\phi = 0 \tag{2.47}$$

where α, β, and k_{x} depend on the position x. Note that the equations given above are valid for a particle within allowed energy bands. In order to include forbidden energies, Harrison proposed to analytically continue the band structure as well as the parameters α and β for complex values of k_{x} (and hence forbidden energy regions). For small variations of α, β and k_{x} with x, the solution of Eq. 2.47 in the WKB-approximation is given by[60, 67]

$$\phi = \phi_{\parallel}\cdot A\cdot\frac{1}{\sqrt{\alpha\beta k_{\mathrm{x}}}}\cdot\exp\left(i\int k_{\mathrm{x}}dx\right) \tag{2.48}$$

with A being a normalization constant. $\phi_{\parallel}$ contains the spatial evolution of ϕ along the y and z axis. In analogy to Bardeen, Harrison assumed a tunnel region from $x = -a$ to $x = a$ and constructed the left-hand side (right-hand side) wave function $\phi_{\mathrm{l}}(\phi_{\mathrm{r}})$ which is oscillating for the allowed energy region for $x < -a$ ($x > a$) and decays exponentially within and behind the tunnel barrier for $x > -a$ ($x < a$). Assuming that $\alpha\beta k_{\mathrm{x}} = 0$ at $x = -a$, the left-hand side wave function is given

by[67]

$$\begin{aligned}\phi_{\mathrm{l}} &= \phi_{\parallel} \cdot A_{\mathrm{l}} \cdot \frac{1}{\sqrt{\alpha\beta k_{\mathrm{x}}}} \cdot \cos\left(\int_{x}^{-a} k_{\mathrm{x}} dx + \gamma_{\mathrm{l}}\right), \text{ for } x < -a \\ \phi_{\mathrm{l}} &= \phi_{\parallel} \cdot \frac{1}{2} A_{\mathrm{l}} \cdot \frac{1}{\sqrt{\alpha\beta k_{\mathrm{x}}}} \cdot \exp\left(-\int_{-a}^{x} |k_{\mathrm{x}}|\, dx\right), \text{ for } x > -a\end{aligned} \tag{2.49}$$

where γ_{l} is an additional phase-shift of the cosine function and the normalization constant $A_{\mathrm{l}} = 2\,(\alpha\beta k_{\mathrm{x}})|_{\mathrm{l}}\,/L_{\mathrm{l}}$ (along the x axis) depends on the length of the left-hand side crystal L_{l}. In full analogy, the wave function of the right-hand side crystal is obtained.[67] At this point, the matrix element can be obtained from the wave functions (Eq. 2.49).

Bardeen showed[60] that the matrix element (Eq. 2.33) can be rewritten in terms of the probability density current operator in x-direction $J_{\mathrm{x}}(\phi_{\mathrm{r}}, \phi_{\mathrm{l}})$, evaluated at a position x_1 within the barrier region. From Eq. 2.33 one obtains

$$\begin{aligned}M(\phi_{\mathrm{r}}, \phi_{\mathrm{l}}) &= -\frac{\hbar^2}{2m_{\mathrm{e}}} \int \phi_{\mathrm{l}}^{*} \nabla\phi_{\mathrm{r}} - \phi_{\mathrm{r}} \nabla\phi_{\mathrm{l}}^{*}\, d\vec{S} \\ &= -\frac{\hbar^2}{2m_{\mathrm{e}}} \iint \phi_{\mathrm{l}}^{*} \nabla\phi_{\mathrm{r}} - \phi_{\mathrm{r}} \nabla\phi_{\mathrm{l}}^{*} \vec{n}_{\mathrm{x}} dy dz\end{aligned} \tag{2.50}$$

where $\vec{n}_{\mathrm{x}}$ is the normal vector in x-direction (perpendicular to the interface plane). All other surface integrals are located infinitely far away and thus are zero, if one assumes normalized wave functions (this assumption is justified, since the particle can not vanish at any time). Further, assuming that $\phi_{\parallel}$ is normalized, the integration over the y-z plane equals unity and one obtains

$$\begin{aligned}M(\phi_{\mathrm{r}}, \phi_{\mathrm{l}}) &= -\frac{\hbar^2}{2m_{\mathrm{e}}} \left(\phi_{\mathrm{l}}^{*} \frac{\partial}{\partial x}\phi_{\mathrm{r}} - \phi_{\mathrm{r}} \frac{\partial}{\partial x}\phi_{\mathrm{l}}^{*}\right)\Big|_{x_1} \\ &= -i\hbar J_{\mathrm{x}}\left(\phi_{\mathrm{r}}, \phi_{\mathrm{l}}\right)|_{x_1}\end{aligned} \tag{2.51}$$

Hence, by substituting Eq. 2.41 into Eq. 2.51, the matrix element in Harrison's approach is given by

$$M(\phi_{\mathrm{r}}, \phi_{\mathrm{l}}) = i\hbar \frac{\hbar}{2m_{\mathrm{e}} i} \left(\phi_{\mathrm{l}}^{*} \alpha \frac{\partial}{\partial x} \beta\phi_{\mathrm{r}} - \phi_{\mathrm{r}} \alpha \frac{\partial}{\partial x} \beta\phi_{\mathrm{l}}^{*}\right) \tag{2.52}$$

By inserting Eq. 2.49 into Eq. 2.52, a straight forward calculation yields[67]

$$|M(\phi_{\mathrm{r}}, \phi_{\mathrm{l}})|^2 = \frac{\hbar^4}{4m_{\mathrm{e}}^2} \frac{(\alpha\beta k_{\mathrm{x}})|_{\mathrm{l}}}{L_{\mathrm{l}}} \frac{(\alpha\beta k_{\mathrm{x}})|_{\mathrm{r}}}{L_{\mathrm{r}}} \exp\left(-2\int_{-a}^{a} |k_{\mathrm{x}}|\, dx\right) \tag{2.53}$$

Harrison assumed specular transmission, which means that the matrix element is zero except for those states, that exhibit exactly the same value of $\vec{k}_\parallel$ on both sides. Eq. 2.53 reveals that the value of $|M(\phi_\mathrm{r}, \phi_\mathrm{l})|^2$ is equal for all states ϕ_l and ϕ_r which correspond to the same value of $\vec{k}_\parallel$. (note that it is $k_\mathrm{x}^2 = (2m_\mathrm{e})/\hbar^2 (E - V) - |\vec{k}_\parallel|$, as already discussed above). Hence, $|M(\phi_\mathrm{r}, \phi_\mathrm{l})|^2$ is denoted by $|M(\vec{k}_\parallel)|^2$.

For the determination of tunnel current, one has to sum the transmission probability $2\pi/\hbar |M(\vec{k}_\parallel)|^2 \rho_\mathrm{r}(E)$ (cf. Eq. 2.27) over all states of the left metal with a fixed value of $\vec{k}_\parallel$ and over all parallel wave vectors $\vec{k}_\parallel$. The result is multiplied by 2 (due to the electron spin) and by the elementary charge.[67] Further, in order to suppress tunneling from empty or into filled states, the Fermi-Dirac distributions are multiplied. The result is shown in Eq. 2.54,

$$\begin{aligned} I &= \frac{4\pi e}{\hbar} \sum_{\vec{k}_\parallel} \sum_{\phi_\mathrm{l}:\ \text{fixed } \vec{k}_\parallel} \left| M(\vec{k}_\parallel) \right|^2 \rho_\mathrm{r}(E) \left[f(E) - f(E + eV) \right] \\ &= \frac{4\pi e}{\hbar} \sum_{\vec{k}_\parallel} \int_{-\infty}^{\infty} \left| M(\vec{k}_\parallel) \right|^2 \rho_\mathrm{r}(E) \rho_\mathrm{l}(E) \left[f(E) - f(E + eV) \right] dE \end{aligned} \tag{2.54}$$

where ρ_r and ρ_l are the density of states for a fixed $\vec{k}_\parallel$.[67] These values can be identified by $\rho_\mathrm{l}(E) = (L_\mathrm{l}/\pi)(\partial E/\partial k_\mathrm{x})^{-1}$ and $\rho_\mathrm{r}(E) = (L_\mathrm{r}/\pi)(\partial E/\partial k_\mathrm{x})^{-1}$, respectively.[67] By substituting this and $|M(\vec{k}_\parallel)|^2$ (i.e. Eq. 2.53) into Eq. 2.54 and by applying the relation shown in Eq. 2.45, one obtains the following equation for the tunnel current:[67]

$$I = \frac{2e}{h} \sum_{\vec{k}_\parallel} \int_{-\infty}^{\infty} dE \left[f(E) - f(E + eV) \right] \exp\left(-2 \int_{-a}^{a} |k_\mathrm{x}|\, dx \right) \tag{2.55}$$

The tunnel current in Eq. 2.55 is converted to a tunnel current density by dividing I by the electrode's surface $L_\mathrm{y} L_\mathrm{z}$. Finally, the sum over $\vec{k}_\parallel$ (i.e. the overlap of $\vec{k}_\parallel$ of both sides) can be replaced by an integral over the number of parallel wave vectors $N_\parallel$. Obviously, this quantity depends on $\vec{k}_{\parallel,\max}^2$ and it is $\sum_{\vec{k}_\parallel} = N_\parallel = \int_0^{\vec{k}_{\parallel,\max}^2} dN_\parallel$. Further, it is commonly known that the area of a single, two-dimensional k-space state is given by $\Omega_\mathrm{k} = (2\pi)^2/(L_\mathrm{y} L_\mathrm{z})$. Thus it is $d^2\vec{k}_\parallel = \Omega_\mathrm{k} dN_\parallel$. By substituting the latter relation for $dN_\parallel$ in the integral, one finds the tunnel current density as described by Eq. 2.56.[67]

$$J = \frac{e}{2\pi^2 h} \int_{-\infty}^{\infty} dE \left[f(E) - f(E + eV) \right] \int d^2\vec{k}_\parallel \exp\left(-2 \int_{-a}^{a} |k_\mathrm{x}|\, dx \right) \tag{2.56}$$

The exponential function in Eq. 2.56 is usually defined as transmission coefficient $D(W)$, where $W = E - \hbar^2 \vec{k}_\parallel^2/(2m_\mathrm{e})$ is the energy of the electron in normal direction (perpendicular to the interface plane).

2.3.4 Harrison's tunnel current applied to semiconductors

In this section the tunnel current model of Harrison and Bardeen, as discussed above, is applied to a semiconductor-vacuum-metal system. This derivation was first performed by Bono and Good[65] for the case of flat bands and extended by Feenstra and Stroscio[66] for the case of tip-induced band bending. Here, the case of electrons that tunnel out of the semiconductor's valence band and into the metal tip is discussed, only. However, tunneling into the conduction band states follows by analogy.

For the description of semiconductors in the parabolic band approximation, the equations derived above remain valid, if one introduces effective masses. Hence, for the valence band, the free electron mass m_e is replaced by the density-of-states effective mass $m_\mathrm{eff,V}$. Further, the upper and lower integration limit of the integral over the energy E in Eq. 2.56 has to be restricted to the allowed bands of both, the tip and the semiconductor,

$$J_\mathrm{V} = \frac{e}{2\pi^2 h} \int_{E_\mathrm{C,tip}}^{E_\mathrm{V}} dE \, (f_\mathrm{S} - f_\mathrm{M}) \int d^2\vec{k}_\parallel D(W) \tag{2.57}$$

where E_V is the energy of the valence band maximum and $E_\mathrm{C,tip}$ is the bottom of the conduction band of the tip. $E_\mathrm{C,tip}$ is defined by the Fermi energy of the metal:

$$(E_\mathrm{F,tip} - E_\mathrm{C,tip}) = \frac{\hbar^2}{2m_\mathrm{e}} \left(3\pi^2 \frac{N}{V}\right)^{2/3} \tag{2.58}$$

with N/V being the density of electrons in the metal. In Eq. 2.57, the Fermi-Dirac distributions of the semiconductor's and the tip's states are abbreviated by

$$f_\mathrm{S}(E) = \frac{1}{1 + \exp\left[\frac{E - E_\mathrm{F}}{kT}\right]} \tag{2.59}$$

and

$$f_\mathrm{M}(E) = \frac{1}{1 + \exp\left[\frac{E - E_\mathrm{F} + eV}{kT}\right]} \tag{2.60}$$

respectively. For the electrons tunneling from the semiconductor into the tip, the conservation of the momentum holds for the component parallel to the surface of

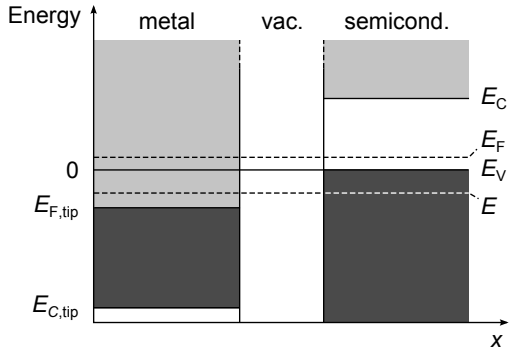

Figure 2.5: Energy levels of the semiconductor and of the tip are shown as a function of the distance x. At the right the conduction band edge E_C, the valence band edge E_V, and the Fermi energy E_F of the semiconductor are indicated. On the left the metal and its conduction band edge $E_\mathrm{C,tip}$ as well as its Fermi energy $E_\mathrm{F,tip} = E_\mathrm{F} + eV$ are shown. E represents any energy level between the limits of the first integral of Eq. 2.57.

the semiconductor. Thus, the latter integral in Eq. 2.57 extends over all parallel wave vectors that can be accommodated in both, the tip and the semiconductor. As discussed in the previous section and according to Ref. [65], the energy W is the normal energy (perpendicular to the surface of the semiconductor), while $E = \frac{\hbar^2}{2m}\left(\vec{k}_\parallel^2 + \vec{k}_\perp^2\right)$ is the total energy. Hence, W is connected to E by

$$W = E - \frac{\hbar^2 \vec{k}_\parallel^2}{2m} \tag{2.61}$$

The mass m can either be the free electron mass m_e for the tip or $m_\mathrm{eff,V}$ for the valence band of the semiconductor. Special attention has to be paid to the last term of Eq. 2.61 for the case of holes in the valence band: The valence band is curved downwards around the maximum and hence the effective mass usually becomes negative. Since unsigned effective masses are used in the simulation, the minus sign in Eq. 2.61 has to be swapped to a plus sign:

$$W = E + \frac{\hbar^2 k_\parallel^2}{2m_\mathrm{eff,V}} \tag{2.62}$$

The necessity of this change of the sign may be further understood by investigating the energy levels of the semiconductor and of the tip versus the distance x as shown

in Fig. 2.5. At the right the conduction band edge E_{C}, the valence band edge E_{V}, and the Fermi energy E_{F} of the semiconductor are indicated. On the left the metal and its conduction band edge $E_{\mathrm{C,tip}}$ as well as its Fermi energy $E_{\mathrm{F,tip}} = E_{\mathrm{F}} + eV$ are shown. E represents any energy level between the limits of the first integral of Eq. 2.57. The maximal energy of holes in the valence band is then given by $E_{\mathrm{V}} - E > 0$. In particular, for $E_{\mathrm{V}} = 0$ the maximal energy is given by $-E$. This is a positive value since E itself is a negative value in the used energy scale. However, the absolute value of W has to be smaller than the absolute value of E, which requires the swapping of the sign of the latter term in Eq. 2.61, if the effective mass is taken to be larger than zero. Note, that Eq. 2.62 is only valid for the holes in the valence band. For the conduction band of the semiconductor *as well as* the tip, Eq. 2.61 still remains valid.

The tunnel current density given by Eq. 2.57 can be simplified further using our sign convention of the energy and the effective masses of the holes. Differentiating Eq. 2.61 with respect to $k_{\parallel}$ yields

$$dk_{\parallel} = -\frac{m_{\mathrm{e}}}{\hbar^2 k_{\parallel}} dW \ . \tag{2.63}$$

Furthermore, the second integral of Eq. 2.57 can be rewritten and solved using polar coordinates ($k_{\parallel}$,θ).

$$\int d^2k_{\parallel} D(W) = \int_{k_{\parallel,\min}}^{k_{\parallel,\max}} dk_{\parallel} k_{\parallel} \int_0^{2\pi} d\theta D(W) = 2\pi \int_{k_{\parallel,\min}}^{k_{\parallel,\max}} dk_{\parallel} k_{\parallel} D(W) \tag{2.64}$$

and by substituting Eq. 2.63 into 2.64, the integral over the parallel wave vector can be transformed into an integral over the normal component of the energy W.

$$2\pi \int_{k_{\parallel,\min}}^{k_{\parallel,\max}} dk_{\parallel} k_{\parallel} D(W) = -2\pi \frac{m_{\mathrm{e}}}{\hbar^2} \int_{W_{\min}}^{W_{\max}} dW D(W) \tag{2.65}$$

The overlap of the parallel wave vectors of the semiconductor and the metal has to be determined in the next step in order to obtain expressions for the maximal and minimal normal energy $W_{\max}$ and $W_{\min}$, respectively. Therefore, one needs to specify the maximal and minimal parallel wave vectors for holes within the semiconductor, first. On the one hand, when the normal wave vector of the holes is maximal, the parallel wave vector becomes zero. On the other hand, when the normal wave vector is zero, the total energy E is attributed to the (maximal) parallel wave vector of the holes:

$$k_{\parallel,\mathrm{min,SC}} = 0 \tag{2.66}$$

$$k_{\parallel,\mathrm{max,SC}} = \frac{2m_{\mathrm{eff,V}}}{\hbar^2}\left(E_\mathrm{V} - E\right) \tag{2.67}$$

Second, the maximal and minimal parallel wave vector of the metal tip can be found analogous.

$$k_{\parallel,\mathrm{min,tip}} = 0 \tag{2.68}$$

$$k_{\parallel,\mathrm{max,tip}} = \frac{2m_\mathrm{e}}{\hbar^2}\left(E - E_\mathrm{C,tip}\right) \tag{2.69}$$

Depending on the value of E, the overlap of the (maximal) parallel wave vector is limited by $k_{\parallel,\mathrm{max,tip}}$ or $k_{\parallel,\mathrm{max,SC}}$, respectively. Thus, one has to determine the energy E_0 where it is $k_{\parallel,\mathrm{max,tip}} = k_{\parallel,\mathrm{max,SC}}$. With $\alpha = m_{\mathrm{eff,V}}/m_\mathrm{e}$, one obtains the following relation.

$$E_0 = \frac{E_\mathrm{C,tip} + \alpha E_\mathrm{V}}{\alpha + 1} \tag{2.70}$$

Moreover, by comparing Eqs. 2.67 and 2.69, one finds that $k_{\parallel,\mathrm{max,SC}} < k_{\parallel,\mathrm{max,tip}}$ for $E > E_0$, while $k_{\parallel,\mathrm{max,SC}} > k_{\parallel,\mathrm{max,tip}}$ for $E < E_0$.[65] This must be taken into account in Eq. 2.57 by splitting the integral over the energy E into two integrals.

$$\begin{aligned}
J_\mathrm{V} &= \frac{e}{2\pi^2 h}\int_{E_\mathrm{C,tip}}^{E_\mathrm{V}} dE\left(f_\mathrm{S} - f_\mathrm{M}\right)\int d^2k_\parallel D(W) \\
&= -\frac{e}{2\pi^2 h}\int_{E_\mathrm{C,tip}}^{E_\mathrm{V}} dE\left(f_\mathrm{S} - f_\mathrm{M}\right)2\pi\frac{m_\mathrm{e}}{\hbar^2}\int_{E+\frac{\hbar^2}{2m_\mathrm{e}}k_{\parallel,\mathrm{min}}}^{E+\frac{\hbar^2}{2m_\mathrm{e}}k_{\parallel,\mathrm{max}}} dW D(W) \\
&= -\frac{m_\mathrm{e}e}{2\pi^2\hbar^3}\left(\int_{E_\mathrm{C,tip}}^{E_0} dE\left(f_\mathrm{S} - f_\mathrm{M}\right)\int_E^{E-\frac{\hbar^2}{2m_\mathrm{e}}\frac{2m_\mathrm{e}}{\hbar^2}\left[E-E_\mathrm{C,tip}\right]} dW D(W)\right. \\
&\left. + \int_{E_0}^{E_\mathrm{V}} dE\left(f_\mathrm{S} - f_\mathrm{M}\right)\int_E^{E+\frac{\hbar^2}{2m_\mathrm{e}}\frac{2\alpha m_\mathrm{e}}{\hbar^2}\left[E_\mathrm{V}-E\right]} dW D(W)\right)
\end{aligned} \tag{2.71}$$

Note, that the upper integration limit of the integral over the normal energy W is $E - \frac{\hbar^2}{2m_\mathrm{e}}\frac{2m_\mathrm{e}}{\hbar^2}\left[E - E_\mathrm{C,tip}\right]$ for the part that is limited by the maximal parallel wave vector of the electrons from the tip, while it is $E + \frac{\hbar^2}{2m_\mathrm{e}}\frac{2\alpha m_\mathrm{e}}{\hbar^2}\left[E_\mathrm{V} - E\right]$ for the part that is limited by the maximal parallel wave vector of holes in the valence band. Again, the change of the sign is attributed to the sign of the effective mass of the holes, that is taken to be positive.

At low temperatures, $f_\mathrm{S} - f_\mathrm{M}$ is 1 for the energy interval $[E_\mathrm{F,tip}, E_\mathrm{F}]$ and 0 otherwise. Assuming, that E_0 is smaller than the Fermi energy of the tip $E_\mathrm{F,tip}$,[65] the first term of the splitted energy integral in Eq. 2.71 ($E_0 < E < E_\mathrm{C,tip}$) becomes zero and one ends up with the following equation:

$$J_{\mathrm{V}} = -\frac{m_{\mathrm{e}} e}{2\pi^2\hbar^3} \int_{E_{\mathrm{F,tip}}}^{E_{\mathrm{V}}} dE\,(f_{\mathrm{S}} - f_{\mathrm{M}}) \int_{E}^{E+\alpha[E_{\mathrm{V}}-E]} dW\,D(W) \tag{2.72}$$

The lower integration limit of the integral over E in Eq. 2.72 was changed from E_0 to $E_{\mathrm{F,tip}}$ for the same, previously described reason. Furthermore, one can change the upper integration limit of the same integral from E_{V} to E_{F}, when the difference of the Fermi-functions $f_{\mathrm{S}} - f_{\mathrm{M}}$ is replaced by a step function, that limits contributions to the integral for energies that are greater than the valence band edge $E > E_{\mathrm{V}}$.

$$J_{\mathrm{V}} = -\frac{m_{\mathrm{e}} e}{2\pi^2\hbar^3} \int_{E_{\mathrm{F,tip}}}^{E_{\mathrm{F}}} dE\Theta\,(E_{\mathrm{V}} - E) \int_{E}^{E+\alpha[E_{\mathrm{V}}-E]} dW\,D(W) \tag{2.73}$$

Eq. 2.73 equals the tunnel current density equation given by Ref. [66] with a negative density-of-states effective mass $\alpha = m_{\mathrm{eff,V}}/m_{\mathrm{e}}$ of the valence band.

In analogy, the tunnel current density for tunneling into empty conduction band states is given by[66]

$$J_{\mathrm{C}} = -\frac{m_{\mathrm{e}} e}{2\pi^2\hbar^3} \int_{E_{\mathrm{F,tip}}}^{E_{\mathrm{F}}} dE\Theta\,(E - E_{\mathrm{C}}) \int_{E}^{E+\alpha'[E_{\mathrm{C}}-E]} dW\,D(W) \tag{2.74}$$

with $\alpha' = m_{\mathrm{eff,C}}/m_{\mathrm{e}}$ being the density-of-states effective mass of the conduction band $m_{\mathrm{eff,C}}$, divided by the electron rest mass.

2.3.5 The transmission coefficient

Transmission through vacuum

At the end of Sec. 2.3.3 the transmission coefficient $D(W)$, mainly determined by the WKB approximation, was introduced as the integral over the barrier region $x = [-a, a]$

$$D(W) = \exp\left(-2\int_{-a}^{a} |k_{\mathrm{x}}|\,dx\right) \tag{2.75}$$

where the normal energy is $W = E - \hbar^2\vec{k}_{\parallel}^2/(2m_{\mathrm{e}})$ and the normal wave vector is $k_{\mathrm{x}}^2 = (2m_{\mathrm{e}})/\hbar^2\,(V - E) + |\vec{k}_{\parallel}|^2$. Note the sign of k_{x}^2 is swapped compared to Eq. 2.46, since the integration is over a region within the barrier, where it is $V > E$. From

this, one obtains the following equation for the transmission coefficient.[65]

$$D(W) = \exp\left(-2\int_{-a}^{a}\sqrt{\frac{2m_\mathrm{e}}{\hbar^2}(V-W)}dx\right) \tag{2.76}$$

The shape of the potential through the central axis of the tip apex $V(x)$ is defined by the solution of the Poisson equation for the electrostatic potential between the tip and the semiconductor, as will be discussed later.

In a first, one-dimensional approach that neglects the shape of the tip, the vacuum potential can be approximated by a linear transition between the vacuum levels E_vac of both sides.[66] The band diagram in Fig. 2.6 shows the valence band maximum

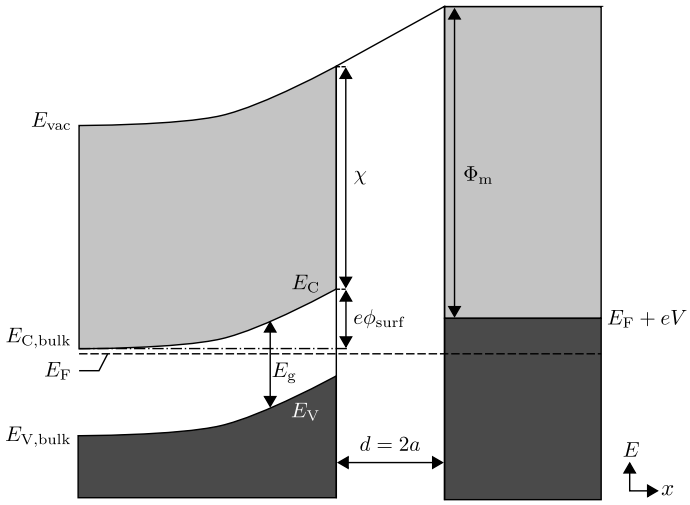

Figure 2.6: Band diagram showing the valence band maximum E_V and the conduction band minimum E_C of the semiconductor as well as the Fermi levels of both, the semiconductor (E_F) and the tip ($E_\mathrm{F} + eV$) as a function of the position x in a one-dimensional approach. Close to the surface, E_C and E_V are bend to higher energy values as compared to their bulk values $E_\mathrm{C,bulk}$ and $E_\mathrm{V,bulk}$, respectively. This effect is caused by the electrostatic potential ϕ, that is not completely screened at the surface of the semiconductor. At the surface of the semiconductor, the electrostatic potential is ϕ_surf. The tip-sample separation is defined by $d := 2a$. Φ_M denotes the work function of the tip, while χ is the electron affinity of the semiconductor. E_g corresponds to the band gap of the semiconductor.

E_V and the conduction band minimum E_C of the semiconductor as well as the Fermi levels of both, the semiconductor (E_F) and the tip ($E_F + eV$) as a function of the position x in a one-dimensional approach. Close to the surface, E_C and E_V are bend to higher energy values as compared to their bulk values $E_{C,bulk}$ and $E_{V,bulk}$, respectively. This effect is caused by the electrostatic potential ϕ, that is not completely screened at the surface of the semiconductor. At the surface of the semiconductor, the electrostatic potential is ϕ_{surf}. The tip-sample separation is defined by $d := 2a$. Φ_M denotes the work function of the tip, while χ is the electron affinity of the semiconductor. E_g corresponds to the band gap of the semiconductor. According to these definitions, the vacuum level of the semiconductor $E_{vac,sc}$ and of the tip $E_{vac,m}$ is given by[66]

$$\begin{aligned} E_{vac,sc} &= E_F + \xi \\ E_{vac,m} &= E_F + eV + \Phi_m \end{aligned} \tag{2.77}$$

where $\xi := E_{C,bulk} - E_F + e\phi_{surf} + \chi$ is the work function of the semiconductor (if the valence band maximum in the bulk is defined to be at zero energy, in analogy to the previous section). The potential within the barrier is then approximated by

$$V'(x) = (E_F + \xi) \cdot (1 - x/d) + (E_F + eV + \Phi_m) \cdot (x/d), \text{ for } x \in [0, d] \tag{2.78}$$

Additionally, an electron that tunnels from one electrode to another causes electric induction when it is close to the surface of one of the electrodes. As a result, an attracting force (image force) is acting on the electron and hence the electrostatic potential in the region of the surfaces is lowered. In analogy to Feenstra and Stroscio,[66] for the simulations, an approximation of the one-dimensional image potential which was introduced by Simmons,[68] is used:

$$V_{img}(x) = -1.15 \frac{e^2 \ln(2)}{8\pi\epsilon_0 d} \cdot \frac{d^2}{x(d-x)}, \text{ for } x \in [0, d] \tag{2.79}$$

In the latter equation, ϵ_0 is the vacuum permittivity. The resulting vacuum potential is then obtained by the sum of Eqs. 2.78 and 2.79:

$$V(x) = V'(x) + V_{img}(x) \tag{2.80}$$

Note that the image force term (Eq. 2.79) has to be added to the three-dimensional solution of the Poisson equation in the vacuum region, too, which will be derived later.

Transmission through the space charge region

As illustrated in Fig. 2.6, upward band bending (as well as downward band bending) of the conduction and valence band leads to space charge regions. Electrons have to tunnel through the vacuum barrier *and* the space charge region in order to get to a region of allowed energy states, again. In contrast to Feenstra and Stroscio[66] one has to replace the term $V - W$ in Eq. 2.76 by $E_C - W$ (where it is $E_C = E_{C,bulk} + e\phi(x)$) *for both*, tunneling out of valence band states *and* tunneling into conduction band states. This is a consequence of the fact that the potential barrier for an electron within the forbidden energy region of the semiconductor is not limited by the vacuum energy anymore but by the conduction band edge. Thus, the transmission coefficient is the same for electrons tunneling out of the valence band or into the conduction band.

2.3.6 Tip-induced band bending in the one-dimensional approach

In the previous section, the importance of the precise knowledge of the tip-induced band bending became apparent: The electrostatic potential ϕ of the tip-vacuum-semiconductor system is used for the calculation of the transmission coefficient, which is dramatically influencing the tunnel current. Thus, in order to calculate the tunnel current using Harrison's WKB approximation, as given by Eqs. 2.73 and 2.74, one first has to find a solution for the electrostatic potential $\phi(x)$ along the central axis through the tip apex. Since the potential is needed at the central axis only, one might come to the conclusion, that it is sufficient to solve the Poisson equation for the one-dimensional problem, only. This approach already yields good results.[66, 69, 13] However, a three-dimensional calculation includes, e.g, the shape of the tip, which has a significant effect on the electric field between the tip and the sample.[70] Furthermore, since a three-dimensional solution cannot be obtained analytically anymore, an iterative Poisson solver is needed. The advantages of such iterative procedures are, that they can easily be extended in order to include, e.g., surface states and continuity equations for electrons and holes. Especially the introduction of the continuity equations is required in order to understand light-excited scanning tunneling spectroscopy, as will be shown later.

Nevertheless, the one-dimensional, analytical solution of the tip-vacuum-semiconductor system is shown first, since it provides bigger physical insight compared to the iterative solvers. Furthermore, on the basis of the one-dimensional approach, a tunnel current simulation software was written, that can be employed for the simulation

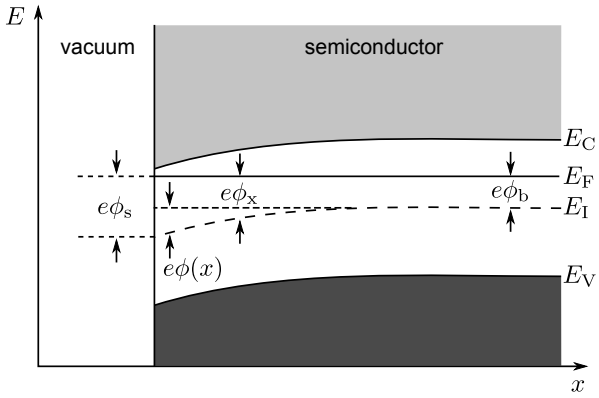

Figure 2.7: Electron energy level diagram in analogy to Ref. [71]

of the tunnel current for simple semiconductors (i.e. without surface states and illumination).

According to Fig. 2.6 and as already discussed, the vacuum potential within the region of the barrier changes linearly. The potential difference between the left side and the right side of the barrier can be assigned to an electric field (at the surface of the semicondcutor) $\varepsilon_s := (E_{vac,m} - E_{vac,sc})/(ed)$. This field causes a space charge region within the semiconductor. The magnitude and length of the space charge region is determined by the physical properties of the semiconductor (i.e. doping concentration, free carrier concentration, etc.).

The solution to this problem was first presented by Seiwatz and Green.[71] According to Fig. 2.7, the band bending at the surface of the semiconductor $e \cdot \phi_{surf}$ can be described by

$$e \cdot \phi_{surf} = e \cdot (\phi_b - \phi_s) \tag{2.81}$$

where ϕ_b and ϕ_s are defined by $e \cdot \phi_x := E_F - E_I(x)$ with $x = s$ at the surface and $x = b$ deep in the bulk material.[71] $E_I(x)$ is the intrinsic Fermi energy (Fermi energy of the semiconductor without doping). Note that the bend bending (and thus the electrostatic potential $\phi(x)$) at an arbitrary position $x > s$ is given by $\phi_b - \phi_x$. Seiwatz and Green used the dimensionless quantity u for their derivation[71]:

$$u = u_x := e \cdot \phi_x/(kT) \tag{2.82}$$

where k is the Boltzmann constant and T is the temperature. Since the electrostatic

field is conservative, it can be described by the change of the potential ϕ_{x}:

$$\varepsilon_{\mathrm{x}} = -\frac{d}{dx}\phi_{\mathrm{x}} = -\frac{kT}{e}\frac{du}{dx} \tag{2.83}$$

On the other hand due to Maxwell's first equation, the divergence of the electrostatic field equals the charge density $\rho(\mathrm{x})$ and hence, by employing Eq. 2.83, one obtains the Poisson equation:

$$\frac{d^2u}{dx^2} = -\frac{e}{\epsilon_{\mathrm{r}}\epsilon_0 kT}\cdot\rho(u) \tag{2.84}$$

ϵ_{r} is the relative permittivity of the semiconductor. For the one-dimensional case, the Poisson equation can be solved by multiplying the factor du/dx on both sides of the equation, followed by an integration over x.[72]

$$\frac{du}{dx}\frac{d^2u}{dx^2} = -\frac{e}{\epsilon_{\mathrm{r}}\epsilon_0 kT}\cdot\rho(u)\frac{du}{dx} \tag{2.85}$$

By employing the derivation rule[72]

$$\frac{du}{dx}\frac{d^2u}{dx^2} = \frac{1}{2}\frac{d}{dx}\left(\frac{du}{dx}\right)^2 \tag{2.86}$$

Eq. 2.85 can be transformed into the integral form (integration from a point x_{b} deep in the bulk material to an arbitrary point x close to the surface).[72]

$$\left(\frac{du}{dx}\right)^2\Bigg|_{x_{\mathrm{B}}} - \left(\frac{du}{dx}\right)^2\Bigg|_{x} = -\frac{2e}{\epsilon_{\mathrm{r}}\epsilon_0 kT}\cdot\int_{u_{\mathrm{x}}}^{u_{\mathrm{b}}}\rho(u)\,du \tag{2.87}$$

By noting that du/dx is zero deep inside the bulk at x_{b}, Eq. 2.87 becomes[72]:

$$\frac{du}{dx} = \pm\sqrt{\frac{2e}{\epsilon_{\mathrm{r}}\epsilon_0 kT}}\cdot\left(\int_{u_{\mathrm{x}}}^{u_{\mathrm{b}}}\rho(u)\,du\right)^{\frac{1}{2}} \tag{2.88}$$

Eq. 2.88 only depends on $u_{\mathrm{b}} = \text{const.}$ and u_{x}. Inserting Eq. 2.88 into Eq. 2.83 yields the electric field as a function of u_{x}, which can easily be transformed into ϕ_{x}:

$$\varepsilon_{\mathrm{x}} = -\frac{kT}{e}\frac{du}{dx} = \mp\frac{kT}{e}\left(\sqrt{\frac{2e}{\epsilon_{\mathrm{r}}\epsilon_0 kT}}\cdot\left(\int_{u_{\mathrm{x}}}^{u_{\mathrm{b}}}\rho(u)\,du\right)^{\frac{1}{2}}\right) \tag{2.89}$$

The charge density $\rho(u)$ of the semiconductor is given by

$$\rho(u) = e\left(N_{\mathrm{D}}^{+} - N_{\mathrm{A}}^{-} + p_0 - n_0\right) \tag{2.90}$$

where n_0 is the concentration of free electrons and p_0 is the concentration of free holes. These charge densities in the semiconductor are assumed to follow the effective mass approximations. For the conduction band, this approximation is given by[73]

$$n_0 = N_{\mathrm{C}} \frac{2}{\sqrt{\pi}} F_{1/2}\left(\frac{E_{\mathrm{F}} - E_{\mathrm{C}}}{kT}\right) \tag{2.91}$$

where E_{C} is the minimum of the conduction band and $F_{1/2}$ is the Fermi-Dirac integral (as defined below). N_{C} is the effective density of states, given by $N_{\mathrm{C}} = 2(2\pi m_{\mathrm{eff,C}} kT/h^2)^{3/2}$. For the charge density of the valence band, the approximation is given by

$$p_0 = N_{\mathrm{V}} \frac{2}{\sqrt{\pi}} F_{1/2}\left(\frac{E_{\mathrm{V}} - E_{\mathrm{F}}}{kT}\right) \tag{2.92}$$

where E_{V} is the maximum of the valence band and $N_{\mathrm{V}} = 2(2\pi m_{\mathrm{eff,V}} kT/h^2)^{3/2}$.

The density of ionized donors N_{D}^{+} and acceptors N_{A}^{-} are defined as [71]

$$N_{\mathrm{D}}^{+} = N_{\mathrm{D}}\left(1 + 2\exp\left[\left(E_{\mathrm{F}} - E_{\mathrm{D}}\right)/kT\right]\right)^{-1} \tag{2.93}$$

$$N_{\mathrm{A}}^{-} = N_{\mathrm{A}}\left(1 + 2\exp\left[\left(E_{\mathrm{A}} - E_{\mathrm{F}}\right)/kT\right]\right)^{-1} \tag{2.94}$$

respectively, where N_{D} (N_{A}) is the concentration of donors (acceptors) and E_{D} (E_{A}) is the respective energy level. Note that E_{D} and E_{A} (in analogy to E_{C} and E_{V}) are shifted by $\phi_{\mathrm{b}} - \phi_{\mathrm{x}}$ in the region of non-zero band bending.

The Fermi-Dirac integral $F_{\mathrm{j}}(\eta)$ is defined by:[71]

$$F_{\mathrm{j}}(\eta) = \int_0^{\infty} \frac{x^j}{1 + \exp(x - \eta)} dx \tag{2.95}$$

Equation 2.95 is charaterized by the absence of the prefactor $1/\Gamma(j+1)$, where $\Gamma(j)$ is the Gamma function, and is also known as Sommerfeld's definition of the Fermi-Dirac integral.[74] Further, the derivative of the Fermi-Dirac integral with respect to η yields a decrementation of j by minus one:[74]

$$\frac{d}{d\eta} F_{\mathrm{j}}(\eta) = F_{\mathrm{j\text{-}1}}(\eta) \tag{2.96}$$

In the following, n, p, N_{A}^{-}, and N_{D}^{+} are obtained as functions of u, which are suitable

for the insertion in Eqs. 2.90 and 2.89, respectively.

$$n_0(u) = N_\mathrm{C}\frac{2}{\sqrt{\pi}}F_{1/2}\left(u - \frac{E_\mathrm{C,bulk} - E_\mathrm{I,bulk}}{kT}\right) \tag{2.97}$$

$$p_0(u) = N_\mathrm{V}\frac{2}{\sqrt{\pi}}F_{1/2}\left(\frac{E_\mathrm{V,bulk} - E_\mathrm{I,bulk}}{kT} - u\right) \tag{2.98}$$

$$N_\mathrm{D}^+(u) = N_\mathrm{D}\left(1 + 2\mathrm{exp}[u - \left(E_\mathrm{D,bulk} - E_\mathrm{I,bulk}\right)/kT]\right)^{-1} \tag{2.99}$$

$$N_\mathrm{A}^- = N_\mathrm{A}\left(1 + 2\mathrm{exp}[\left(E_\mathrm{A,bulk} - E_\mathrm{I,bulk}\right)/kT - u]\right)^{-1} \tag{2.100}$$

In the upper equations $E_\mathrm{I,bulk}$ is the intrinsic Fermi level of the semiconductor's bulk material and $E_\mathrm{D,bulk}$ ($E_\mathrm{A,bulk}$) corresponds to unbend ionization energies in the bulk. Inserting Eqs. 2.99, 2.100, 2.97, and 2.98 into the electric field, given by Eq. 2.89, the integration over u can be easily performed (employing the deviation rule in Eq. 2.96) and yields the following result[71],

$$\begin{aligned}
\varepsilon_\mathrm{x}(u_\mathrm{x}) = \pm\frac{kT}{e}\frac{1}{\lambda_\mathrm{d}}\cdot\Bigg\{&\frac{N_\mathrm{D}}{n_\mathrm{i}}\ln\left[\frac{1+\frac{1}{2}\mathrm{exp}((E_\mathrm{D,bulk}-E_\mathrm{I,bulk})/(kT)-u_\mathrm{x})}{1+\frac{1}{2}\mathrm{exp}((E_\mathrm{D,bulk}-E_\mathrm{I,bulk})/(kT)-u_\mathrm{b})}\right]\\
&+\frac{N_\mathrm{A}}{n_\mathrm{i}}\ln\left[\frac{1+\frac{1}{2}\mathrm{exp}(u_\mathrm{x}-(E_\mathrm{A,bulk}-E_\mathrm{I,bulk})/(kT))}{1+\frac{1}{2}\mathrm{exp}(u_\mathrm{b}-(E_\mathrm{A,bulk}-E_\mathrm{I,bulk})/(kT))}\right]\\
-\frac{1}{F_{\frac{1}{2}}((E_\mathrm{V,bulk}-E_\mathrm{I,bulk})/(kT))}\cdot&\left[\frac{2}{3}F_{\frac{3}{2}}((E_\mathrm{V,bulk}-E_\mathrm{I,bulk})/(kT)-u_\mathrm{b})-\right.\\
&\left.\frac{2}{3}F_{\frac{3}{2}}((E_\mathrm{V,bulk}-E_\mathrm{I,bulk})/(kT)-u_\mathrm{x})\right]\\
+\frac{1}{F_{\frac{1}{2}}((E_\mathrm{I,bulk}-E_\mathrm{C,bulk})/(kT))}\cdot&\left[\frac{2}{3}F_{\frac{3}{2}}(u_\mathrm{x}-(E_\mathrm{C,bulk}-E_\mathrm{I,bulk})/(kT))-\right.\\
&\left.\left.\frac{2}{3}F_{\frac{3}{2}}(u_\mathrm{b}-(E_\mathrm{C,bulk}-E_\mathrm{I,bulk})/(kT))\right]\right\}^{\frac{1}{2}}
\end{aligned} \tag{2.101}$$

where the Debye length λ_d and the intrinsic carrier concentration n_i are introduced as noted below.[71]

$$\lambda_\mathrm{d} = (\epsilon_\mathrm{r}\epsilon_0 kT/(2e^2 n_\mathrm{i}))^{\frac{1}{2}} \tag{2.102}$$

$$n_\mathrm{i} = N_\mathrm{C}\frac{2}{\sqrt{\pi}}\cdot F_{\frac{1}{2}}((E_\mathrm{I}-E_\mathrm{C})/(kT)) \tag{2.103}$$

Now that an equation for the electric field as a function of u_x is found, one is able to derive the band bending at the surface of the semiconductor for an applied tip-sample voltage V. According to the definition of u in Eq. 2.82, the band bending at the surface of the semiconductor ϕ_surf, as illustrated in Fig. 2.6 is connected to

u_s by Eq. 2.104.

$$u_\mathrm{s} = u_\mathrm{b} - e \cdot \phi_\mathrm{surf}/(kT) \tag{2.104}$$

Hence, the electric field at the surface of the semiconductor ε_s as defined by Eq. 2.101 can be written (using Eq. 2.104) as a function of ϕ_surf:

$$\varepsilon_\mathrm{s} = \varepsilon_\mathrm{x}(u_\mathrm{b} - e \cdot \phi_\mathrm{surf}/(kT)) \tag{2.105}$$

From the band diagram in Fig. 2.6 one finds a relation between the electric field at the surface and the vacuum energy levels of the tip and the semiconductor.

$$E_\mathrm{vac,sc} + e\varepsilon_\mathrm{s} d = E_\mathrm{vac,m} \tag{2.106}$$

By substituting $E_\mathrm{vac,sc}$, $E_\mathrm{vac,m}$, and ε_s in Eq. 2.106 by their definitions as given by Eqs. 2.77 and 2.105 (together with Eq. 2.101), respectively, the applied tip-sample voltage V is directly related to the potential ϕ_surf at the surface. The resulting equation can be easily solved with respect to ϕ_surf by numerical methods. The resulting value will be denoted by $\phi_\mathrm{surf}(V)$ below.

In a final step, the band bending $\phi(x) = \phi_\mathrm{b} - \phi_\mathrm{x}$ has to be derived as a function of the distance from the semiconductor's surface x for a known band bending at the surface of the semiconductor $\phi_\mathrm{surf}(V)$. Transferring Eq. 2.83 into the integral form yields

$$\phi_\mathrm{x} = -\int_s^x \varepsilon_{\mathrm{x}'}(u_{\mathrm{x}'})dx' \tag{2.107}$$

The difficulty in solving this integral is, that $u_{\mathrm{x}'}$ (and hence $\varepsilon_{\mathrm{x}'}$) is only known at the surface of the semiconductor for $\mathrm{x}' = s$. Hence, one cannot solve the integral analytically. However, a numerical solution can be obtained by the following procedure:

Using the definition of u_x in Eq. 2.82, Eq. 2.107 becomes

$$kT/e \cdot u_\mathrm{x} = -\int_s^x \varepsilon_{\mathrm{x}'}(u_{\mathrm{x}'})dx' \tag{2.108}$$

Rewriting Eq. 2.108 as a sum, suitable for numerical computation yields

$$kT/e \cdot u_\mathrm{x} = -\sum_{i=0}^{i_\mathrm{max}} \varepsilon_{\mathrm{x}_i}(u_{\mathrm{x}_i}) \cdot \frac{x-s}{i_\mathrm{max}} \tag{2.109}$$

with a sufficiently large i_{max} and x_{i} as defined by Eq. 2.110.

$$x_{\mathrm{i}} = s + i/i_{\mathrm{max}} \cdot (x - s) \tag{2.110}$$

By comparing the terms in the sum of Eq. 2.109, one obtains an equation for an iterative determination of u_{x}:[75]

$$u_{\mathrm{x}_{i+1}} = u_{x_{\mathrm{i}}} - \frac{e}{kT}\varepsilon_{\mathrm{x}_i}(u_{\mathrm{x}_i}) \cdot \frac{x - s}{i_{\mathrm{max}}} \tag{2.111}$$

Starting at the surface where $u_{\mathrm{s}} = u_{\mathrm{x}_0}$ is known (cf. Eq. 2.104), one can iteratively determine u_{x} (and thus $\phi(x) = \phi_b - \phi_x = kT/e(u_{\mathrm{b}} - u_{\mathrm{x}})$) at an arbitrary position x within the semiconductor.

The information about the band bending can be used to obtain the tunnel current as described by Eqs. 2.73 and 2.74. However, in the following a method for solving the Poisson equation and the continuity equations for electrons and holes within the semiconductor in three dimensions is presented. This will lead to highly accurate derivations of the band bending (including the three-dimensional shape of the tip and surface states of the sample). Note that the tip-induced band bending at the surface of a semiconductor can be up to 40% smaller for the three-dimensional models compared to the one-dimensional one.[76] This can be attributed to the larger divergence of the three-dimensional potential.[76] Nevertheless, the one dimensional solution can be used for the estimation of the initial values for the three-dimensional problem. Furthermore the incorporation of continuity equations enables the computation and simulation of scanning tunneling spectroscopy experiments under the influence of laser illumination. On the basis of this, a new and wide field of light-excited scanning tunneling spectroscopy can be explained quantitatively for the first time.

Chapter 3

Development of a quantitative model for light-excited tunneling

This chapter is adapted from [P1] (see list of own publications, p. 119),

3.1 Electrostatic potential and carrier distribution

As outlined above, the calculation of the tunnel current requires the electrostatic potential distribution for a biased metal tip-vacuum-semiconductor system. This system requires a full three-dimensional solution of the Poisson equation, since a one-dimensional analytical solution, as outlined in Chap. 2.3.6 does not consider the effect of the localized shape of the tip on the electrostatic potential. In this section the approach used for calculating the electrostatic potential and charge carrier distributions is described. The latter ones are required for a quantitative derivation of the tunnel current under irradiation conditions since generation and recombination terms are introduced, which allow the treatment of additional light excited charge carriers.

3.1.1 System of differential equations

Thus far, Feenstra solved this kind of electrostatic problem using a finite difference method to iteratively solve the Poisson equation.[70] The charge densities n_0 and p_0 in the semiconductor are assumed to follow the effective mass approximations, as in Eqs. 2.91 and 2.92. Besides some material properties and the temperature,

which is assumed to be constant, the electron and hole densities in the effective mass approximation depend only on the position of the valence and conduction band edges relative to the Fermi energy. Hence, these equations do not hold for the description of additional excess carriers generated by photon interaction.

Thus, here the continuity equations for electrons and holes are introduced, additionally. This will give a more general description of the problem, enabling the introduction of carrier generation and recombination. Overall, it is necessary to solve three coupled partial differential equations:

The Poisson equation for the electrostatic potential $\phi(x, y, z)$ at the position (x, y, z) is given by

$$\Delta\phi(x, y, z) + \frac{e}{\epsilon_0 \epsilon_\mathrm{r}} \left(p(x, y, z) - n(x, y, z) + N_\mathrm{D}^+ - N_\mathrm{A}^- \right) = 0 \tag{3.1}$$

where $n(x, y, z)$ and $p(x, y, z)$ are the electron and hole concentrations at position (x, y, z), respectively. The density of ionized donors N_D^+ and acceptors N_A^- are defined as in Eqs. 2.93 and 2.94.

Assuming a time-invariant charge distribution, the continuity equations for electrons and holes are

$$\nabla \cdot \vec{J}_\mathrm{n} - e \cdot R = 0 \tag{3.2}$$

$$\nabla \cdot \vec{J}_\mathrm{p} + e \cdot R = 0 \tag{3.3}$$

where R is a time-averaged generation or recombination rate and $\vec{J}_\mathrm{n}$ ($\vec{J}_\mathrm{p}$) is the current density for electrons (holes). $\vec{J}_\mathrm{n}$ and $\vec{J}_\mathrm{p}$ can be separated into drift and diffusion terms: [77]

$$\vec{J}_\mathrm{n} = e \left(\mu_\mathrm{n} n(x, y, z) \vec{E} + D_\mathrm{n} \nabla n(x, y, z) \right) \tag{3.4}$$

$$\vec{J}_\mathrm{p} = e \left(\mu_\mathrm{p} p(x, y, z) \vec{E} - D_\mathrm{p} \nabla p(x, y, z) \right) \tag{3.5}$$

where μ_n (μ_p) is the mobility and D_n (D_p) is the diffusion coefficient of electrons (holes) in the semiconductor. D_n (D_p) is connected to μ_n (μ_p) by the Einstein relation. Note, the mobility (and the diffusion coefficient) is assumed to be location-independent in this calculation. Inserting Eqs. 3.4 and 3.5 into Eqs. 3.2 and 3.3, respectively, and using the relation $\vec{E} = -\nabla\phi$, the continuity equations become

$$\nabla \cdot (D_\mathrm{n} \cdot \nabla n(x, y, z) - \mu_\mathrm{n} n(x, y, z) \cdot \nabla\phi) - R = 0 \tag{3.6}$$

$$\nabla \cdot (D_\mathrm{p} \cdot \nabla p(x, y, z) + \mu_\mathrm{p} p(x, y, z) \cdot \nabla\phi) - R = 0 \tag{3.7}$$

3.1.2 Difference equations

Equations 3.1, 3.6, and 3.7 represent a system of three coupled partial differential equations which cannot be solved analytically in full generality.[77] For numerical computations one needs adequate *difference* equations for these *differential* equations. In analogy to Selberherr's discretization approach,[77] the differential operators are directly replaced by their corresponding difference operators. The derivation of the discretized Poisson equation replacing Eq. 3.1 is strait forward since the Laplace operator has to be replaced, only. One divides the three spatial directions into a mesh of discrete points (which are in general not equidistant). The continuous physical coordinates (x, y, z) become discrete indices (i, j, k), which are mapped to discrete physical coordinates $(x_\mathrm{i}, y_\mathrm{j}, z_\mathrm{k})$. Hence, for an arbitrary function $f(x_\mathrm{i}, y_\mathrm{j}, z_\mathrm{k})$, the abbreviated notation $f_\mathrm{i,j,k}$ is used. Furthermore, according to Fig. 3.1, it is $f_\mathrm{i+1/2,j,k} = f([x_\mathrm{i}+x_\mathrm{i+1}]/2, y_\mathrm{j}, z_\mathrm{k})$.[77] From Fig. 3.1 one can also obtain the second partial derivative of f along, e.g., the x direction:

$$\left.\frac{\partial^2 f}{\partial x^2}\right|_\mathrm{i,j,k} \approx \frac{\left.\frac{\partial f}{\partial x}\right|_\mathrm{i+1/2,j,k} - \left.\frac{\partial f}{\partial x}\right|_\mathrm{i\text{-}1/2,j,k}}{\left(x_\mathrm{i+1} - x_\mathrm{i\text{-}1}\right)/2} \tag{3.8}$$

The first partial derivatives at the mid-interval positions $i + 1/2$ and $i - 1/2$ are given by[77]

$$\left.\frac{\partial f}{\partial x}\right|_\mathrm{i+1/2,j,k} \approx \frac{f_\mathrm{i+1,j,k} - f_\mathrm{i,j,k}}{x_\mathrm{i+1} - x_\mathrm{i}} \tag{3.9}$$

$$\left.\frac{\partial f}{\partial x}\right|_\mathrm{i\text{-}1/2,j,k} \approx \frac{f_\mathrm{i,j,k} - f_\mathrm{i\text{-}1,j,k}}{x_\mathrm{i} - x_\mathrm{i\text{-}1}} \tag{3.10}$$

With the help of Eqs. 3.8, 3.9 and 3.10, the Laplace operator in Eq. 3.1 can be approximated by[77]

$$\begin{aligned}\Bigg(&\frac{\frac{\phi_\mathrm{i+1,j,k}-\phi_\mathrm{i,j,k}}{x_\mathrm{i+1}-x_\mathrm{i}} - \frac{\phi_\mathrm{i,j,k}-\phi_\mathrm{i\text{-}1,j,k}}{x_\mathrm{i}-x_\mathrm{i\text{-}1}}}{\frac{x_\mathrm{i+1}-x_\mathrm{i\text{-}1}}{2}} + \frac{\frac{\phi_\mathrm{i,j+1,k}-\phi_\mathrm{i,j,k}}{y_\mathrm{j+1}-y_\mathrm{j}} - \frac{\phi_\mathrm{i,j,k}-\phi_\mathrm{i,j\text{-}1,k}}{y_\mathrm{j}-y_\mathrm{j\text{-}1}}}{\frac{y_\mathrm{j+1}-y_\mathrm{j\text{-}1}}{2}} \\ &+ \frac{\frac{\phi_\mathrm{i,j,k+1}-\phi_\mathrm{i,j,k}}{z_\mathrm{k+1}-z_\mathrm{k}} - \frac{\phi_\mathrm{i,j,k}-\phi_\mathrm{i,j,k\text{-}1}}{z_\mathrm{k}-z_\mathrm{k\text{-}1}}}{\frac{z_\mathrm{k+1}-z_\mathrm{k\text{-}1}}{2}}\Bigg) + \frac{e}{\epsilon_0\epsilon_\mathrm{r}}\left(-n_\mathrm{i,j,k} + p_\mathrm{i,j,k} + N_\mathrm{D}^+ - N_\mathrm{A}^-\right) = 0\end{aligned} \tag{3.11}$$

The derivation of the discretized continuity equations for holes and electrons is more complex and is derived in analogy to Ref. [77] (starting on page 155) for the three

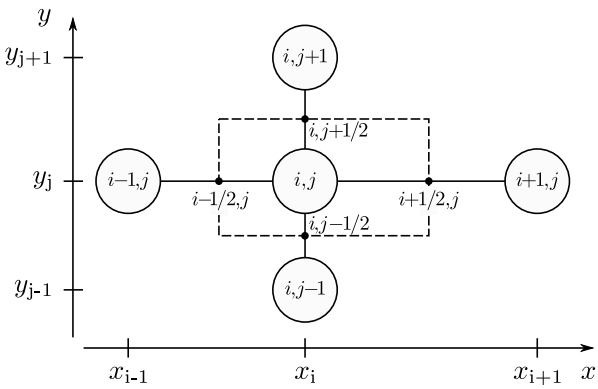

Figure 3.1: Sketch of the finite difference grid in two dimensions for reasons of clarification, in analogy to Ref. [77]

dimensional case here. The resulting discretized continuity equation for electrons is

$$
\begin{aligned}
&\frac{B\left(\frac{\phi_{\mathrm{i+1,j,k}}-\phi_{\mathrm{i,j,k}}}{kT}\right)\cdot n_{\mathrm{i+1,j,k}} - B\left(\frac{\phi_{\mathrm{i,j,k}}-\phi_{\mathrm{i+1,j,k}}}{kT}\right)\cdot n_{\mathrm{i,j,k}}}{(x_{\mathrm{i+1}}-x_{\mathrm{i}})\cdot\frac{x_{\mathrm{i+1}}-x_{\mathrm{i\text{-}1}}}{2}} \\
&-\frac{B\left(\frac{\phi_{\mathrm{i,j,k}}-\phi_{\mathrm{i\text{-}1,j,k}}}{kT}\right)\cdot n_{\mathrm{i,j,k}} - B\left(\frac{\phi_{\mathrm{i\text{-}1,j,k}}-\phi_{\mathrm{i,j,k}}}{kT}\right)\cdot n_{\mathrm{i\text{-}1,j,k}}}{(x_{\mathrm{i}}-x_{\mathrm{i\text{-}1}})\cdot\frac{x_{\mathrm{i+1}}-x_{\mathrm{i\text{-}1}}}{2}} \\
&+\frac{B\left(\frac{\phi_{\mathrm{i,j+1,k}}-\phi_{\mathrm{i,j,k}}}{kT}\right)\cdot n_{\mathrm{i,j+1,k}} - B\left(\frac{\phi_{\mathrm{i,j,k}}-\phi_{\mathrm{i,j+1,k}}}{kT}\right)\cdot n_{\mathrm{i,j,k}}}{(y_{\mathrm{j+1}}-y_{\mathrm{j}})\cdot\frac{y_{\mathrm{j+1}}-y_{\mathrm{j\text{-}1}}}{2}} \\
&-\frac{B\left(\frac{\phi_{\mathrm{i,j,k}}-\phi_{\mathrm{i,j\text{-}1,k}}}{kT}\right)\cdot n_{\mathrm{i,j,k}} - B\left(\frac{\phi_{\mathrm{i,j\text{-}1,k}}-\phi_{\mathrm{i,j,k}}}{kT}\right)\cdot n_{\mathrm{i,j\text{-}1,k}}}{(y_{\mathrm{j}}-y_{\mathrm{j\text{-}1}})\cdot\frac{y_{\mathrm{j+1}}-y_{\mathrm{j\text{-}1}}}{2}} \\
&+\frac{B\left(\frac{\phi_{\mathrm{i,j,k+1}}-\phi_{\mathrm{i,j,k}}}{kT}\right)\cdot n_{\mathrm{i,j,k+1}} - B\left(\frac{\phi_{\mathrm{i,j,k}}-\phi_{\mathrm{i,j,k+1}}}{kT}\right)\cdot n_{\mathrm{i,j,k}}}{(z_{\mathrm{k+1}}-z_{\mathrm{k}})\cdot\frac{z_{\mathrm{k+1}}-z_{\mathrm{k\text{-}1}}}{2}} \\
&-\frac{B\left(\frac{\phi_{\mathrm{i,j,k}}-\phi_{\mathrm{i,j,k\text{-}1}}}{kT}\right)\cdot n_{\mathrm{i,j,k}} - B\left(\frac{\phi_{\mathrm{i,j,k\text{-}1}}-\phi_{\mathrm{i,j,k}}}{kT}\right)\cdot n_{\mathrm{i,j,k\text{-}1}}}{(z_{\mathrm{k}}-z_{\mathrm{k\text{-}1}})\cdot\frac{z_{\mathrm{k+1}}-z_{\mathrm{k\text{-}1}}}{2}} \\
&-\frac{R}{D_{\mathrm{n}}} = 0
\end{aligned}
\tag{3.12}
$$

with the Bernoulli function $B(x) = x/(\exp(x) - 1)$.

Analogously, the discretized continuity equation for holes can be found to be [77]

$$
\begin{aligned}
&\frac{B\left(\frac{\phi_{\mathrm{i,j,k}}-\phi_{\mathrm{i+1,j,k}}}{kT}\right)\cdot p_{\mathrm{i+1,j,k}} - B\left(\frac{\phi_{\mathrm{i+1,j,k}}-\phi_{\mathrm{i,j,k}}}{kT}\right)\cdot p_{\mathrm{i,j,k}}}{(x_{\mathrm{i+1}}-x_{\mathrm{i}})\cdot\frac{x_{\mathrm{i+1}}-x_{\mathrm{i\text{-}1}}}{2}} \\
-&\frac{B\left(\frac{\phi_{\mathrm{i\text{-}1,j,k}}-\phi_{\mathrm{i,j,k}}}{kT}\right)\cdot p_{\mathrm{i,j,k}} - B\left(\frac{\phi_{\mathrm{i,j,k}}-\phi_{\mathrm{i\text{-}1,j,k}}}{kT}\right)\cdot p_{\mathrm{i\text{-}1,j,k}}}{(x_{\mathrm{i}}-x_{\mathrm{i\text{-}1}})\cdot\frac{x_{\mathrm{i+1}}-x_{\mathrm{i\text{-}1}}}{2}} \\
+&\frac{B\left(\frac{\phi_{\mathrm{i,j,k}}-\phi_{\mathrm{i,j+1,k}}}{kT}\right)\cdot p_{\mathrm{i,j+1,k}} - B\left(\frac{\phi_{\mathrm{i,j+1,k}}-\phi_{\mathrm{i,j,k}}}{kT}\right)\cdot p_{\mathrm{i,j,k}}}{(y_{\mathrm{j+1}}-y_{\mathrm{j}})\cdot\frac{y_{\mathrm{j+1}}-y_{\mathrm{j\text{-}1}}}{2}} \\
-&\frac{B\left(\frac{\phi_{\mathrm{i,j\text{-}1,k}}-\phi_{\mathrm{i,j,k}}}{kT}\right)\cdot p_{\mathrm{i,j,k}} - B\left(\frac{\phi_{\mathrm{i,j,k}}-\phi_{\mathrm{i,j\text{-}1,k}}}{kT}\right)\cdot p_{\mathrm{i,j\text{-}1,k}}}{(y_{\mathrm{j}}-y_{\mathrm{j\text{-}1}})\cdot\frac{y_{\mathrm{j+1}}-y_{\mathrm{j\text{-}1}}}{2}} \\
+&\frac{B\left(\frac{\phi_{\mathrm{i,j,k}}-\phi_{\mathrm{i,j,k+1}}}{kT}\right)\cdot p_{\mathrm{i,j,k+1}} - B\left(\frac{\phi_{\mathrm{i,j,k+1}}-\phi_{\mathrm{i,j,k}}}{kT}\right)\cdot p_{\mathrm{i,j,k}}}{(z_{\mathrm{k+1}}-z_{\mathrm{k}})\cdot\frac{z_{\mathrm{k+1}}-z_{\mathrm{k\text{-}1}}}{2}} \\
-&\frac{B\left(\frac{\phi_{\mathrm{i,j,k\text{-}1}}-\phi_{\mathrm{i,j,k}}}{kT}\right)\cdot p_{\mathrm{i,j,k}} - B\left(\frac{\phi_{\mathrm{i,j,k}}-\phi_{\mathrm{i,j,k\text{-}1}}}{kT}\right)\cdot p_{\mathrm{i,j,k\text{-}1}}}{(z_{\mathrm{k}}-z_{\mathrm{k\text{-}1}})\cdot\frac{z_{\mathrm{k+1}}-z_{\mathrm{k\text{-}1}}}{2}} \\
-&\frac{R}{D_{\mathrm{p}}} = 0
\end{aligned}
\tag{3.13}
$$

3.1.3 Boundaries and interfaces

Neumann boundary conditions are assumed for both the electrostatic potential and the charge densities. This means that at the borders of the calculation grid in normal direction the partial derivation of the electrostatic potential and the current densities for electrons and holes are zero. A precise derivation of the boundary conditions with respect to a minimization of the truncation error is given in Ref. [77] on page 172. Particular attention must be paid to the continuity condition for the electrostatic potential at the surface of the semiconductor. For a surface, which is nearly free of surface states, the normal component of the electric displacement field $\vec{D}$ remains constant at the transition from the semiconductor to the vacuum. With surface states being present within or even outside of the fundamental band gap, a surface charge distribution σ gives rise to a change of $\vec{D}$ according to Eq. 3.14.

$$\vec{n}\cdot(\vec{D}_{\mathrm{vac}}-\vec{D}_{\mathrm{semi}}) = \sigma \tag{3.14}$$

where $\vec{n}$ is the normal vector of the surface. Using the relation for isotropic media $\vec{D} = -\epsilon_0\epsilon_\mathrm{r} \cdot \nabla\phi$ one obtains for a normal vector in x-direction:

$$\epsilon_0\epsilon_\mathrm{r} \cdot \left.\frac{\partial\phi}{\partial x}\right|_\mathrm{semi} - \epsilon_0 \left.\frac{\partial\phi}{\partial x}\right|_\mathrm{vac} - \sigma = 0 \tag{3.15}$$

Again, Eq. 3.15 can be discretized by employing difference operators.[77] Assuming that all points $x \geq x_\mathrm{surf}$ belong to the semiconductor, whereas all points $x < x_\mathrm{surf}$ belong to either the tip or the vacuum, Eq. 3.11 needs to be replaced for $x = x_\mathrm{surf}$ (or $i = i_\mathrm{surf}$, respectively) by

$$\begin{aligned}
&\left(\frac{\epsilon_\mathrm{r}\epsilon_0 \dfrac{\phi_{\mathrm{i+1,j,k}} - \phi_{\mathrm{i,j,k}}}{x_{\mathrm{i+1}} - x_\mathrm{i}} - \epsilon_0 \dfrac{\phi_{\mathrm{i,j,k}} - \phi_{\mathrm{i\text{-}1,j,k}}}{x_\mathrm{i} - x_{\mathrm{i\text{-}1}}} + \sigma_{\mathrm{i,j,k}}}{\dfrac{\epsilon_\mathrm{r}\epsilon_0 \left(x_{\mathrm{i+1}} - x_\mathrm{i}\right) + \epsilon_0 \left(x_\mathrm{i} - x_{\mathrm{i\text{-}1}}\right)}{2}} \right. \\
&\left. + \frac{\dfrac{\phi_{\mathrm{i,j+1,k}} - \phi_{\mathrm{i,j,k}}}{y_{\mathrm{j+1}} - y_\mathrm{j}} - \dfrac{\phi_{\mathrm{i,j,k}} - \phi_{\mathrm{i,j\text{-}1,k}}}{y_\mathrm{j} - y_{\mathrm{j\text{-}1}}}}{\dfrac{y_{\mathrm{j+1}} - y_{\mathrm{j\text{-}1}}}{2}} + \frac{\dfrac{\phi_{\mathrm{i,j,k+1}} - \phi_{\mathrm{i,j,k}}}{z_{\mathrm{k+1}} - z_\mathrm{k}} - \dfrac{\phi_{\mathrm{i,j,k}} - \phi_{\mathrm{i,j,k\text{-}1}}}{z_\mathrm{k} - z_{\mathrm{k\text{-}1}}}}{\dfrac{z_{\mathrm{k+1}} - x_{\mathrm{k\text{-}1}}}{2}} \right) \\
&- \frac{e}{\epsilon_0\epsilon_\mathrm{r}} \frac{x_\mathrm{i} - x_{\mathrm{i\text{-}1}}}{\epsilon_\mathrm{r}\left(x_{\mathrm{i+1}} - x_\mathrm{i}\right) + \left(x_\mathrm{i} - x_{\mathrm{i\text{-}1}}\right)} \cdot \left(n_{\mathrm{i,j,k}} - p_{\mathrm{i,j,k}} - N_\mathrm{D}^+ + N_\mathrm{A}^-\right) = 0
\end{aligned} \tag{3.16}$$

In the region of the semiconductor, Eqs. 3.11 (for $x > x_\mathrm{surf}$), 3.16 (for $x = x_\mathrm{surf}$), 3.12, and 3.13 have to be solved, whereas in the region of the vacuum only Eq. 3.11 has to be solved due to the absence of charge carriers. At the tip the electrostatic potential ϕ_tip is set to a constant value, the so-called contact potential $\Delta\phi$.[78] It can be interpreted as the potential difference between the tip and the surface of the semiconductor

$$\phi_\mathrm{tip} = \Delta\phi = V + \left(E_\mathrm{F} - E_\mathrm{C} - \chi + \phi_\mathrm{m}\right)/e \tag{3.17}$$

where V is the voltage applied between the tip and the semiconductor, χ is the electron affinity of the semiconductor and ϕ_m is the work function of the tip.

3.1.4 Initial values

For the initial values of the electrostatic potential $\phi^0_{\mathrm{i,j,k}}$ and the charge densities $n^0_{\mathrm{i,j,k}}$ and $p^0_{\mathrm{i,j,k}}$ within the semiconductor, one assumes that the tip is located infinitely far away from the semiconductor's surface. Hence, the semiconductor is initialized without tip-induced band bending and with equally-distributed carrier

concentrations:

$$\left.\begin{aligned} \phi^0_{\mathrm{i,j,k}} &= 0\,\mathrm{V} \\ n^0_{\mathrm{i,j,k}} &= n_0 + c_{\mathrm{light}} \\ p^0_{\mathrm{i,j,k}} &= p_0 + c_{\mathrm{light}} \end{aligned}\right\} \text{for } i \geq i_{\mathrm{surf}} \tag{3.18}$$

n_0 and p_0 (together with E_{F}) can be easily obtained by solving the charge neutrality condition $n_0 - p_0 - N_{\mathrm{D}}^+ + N_{\mathrm{A}}^- = 0$, when the semiconductor is in equilibrium. For a sample that is illuminated by a laser beam, the initial density of the light-excited carriers c_{light} can be estimated using

$$c_{\mathrm{light}} = \alpha \cdot \frac{P_{\mathrm{opt}}}{E_{\mathrm{ph}} A_{\mathrm{light}}} \cdot \tau \tag{3.19}$$

where α is the absorption coefficient of the semiconductor, τ is the lifetime of the minority carriers, A_{light} is the illuminated surface area, P_{opt} is the optical power of the laser, and E_{ph} is the photon energy. One could also take into account that P_{opt} depends exponentially on the penetration depth of the photons. However, for the samples and light sources that were used in the experiments of this thesis (p-type GaAs with $\alpha \sim 1 \cdot 10^4 \mathrm{cm}^{-1}$ for $E_{\mathrm{ph}} = 1.58$ eV [79], see below), the change of P_{opt} in the region of interest is in the range of only a few percent and hence can be neglected.

For the given problem, one could have chosen other initial values that promise to converge faster to the optimal solution. For example, one could have estimated the tip-induced band bending within the semiconductor by the one-dimensional solution of the Poisson equation as given in Chap. 2.3.6 and use these values for $\phi^0_{\mathrm{i,j,k}}$. However, in practise, the approach given by Eq. 3.18 delivers good results.

3.1.5 Carrier generation and recombination

The generation and recombination process is modeled by radiative band-to-band transitions. For samples with direct band gaps this recombination process is taken to be dominant. The net recombination rate R_{te} in thermal equilibrium and without illumination is given by[80]

$$R_{\mathrm{te}}(x,y,z) = b \cdot (n(x,y,z) \cdot p(x,y,z) - n_0 p_0) \tag{3.20}$$

where b is the bimolecular recombination coefficient. When the laser is switched on, electron and hole pairs will be created with a rate of $R_{\mathrm{light}} = c_{\mathrm{light}}/\tau$. In the absence of the tip-induced band bending (i.e. without a potential gradient for the carriers),

a second equilibrium situation will be reached, when the net recombination rate equals R_{light}:

$$b \cdot ((n_0 + c_{\text{light}})(p_0 + c_{\text{light}}) - n_0 p_0) = R_{\text{light}} \tag{3.21}$$

With the help of Eqs. 3.19 and 3.21, b can be determined and finally, the net recombination rate R for the sample under illumination, suitable for substitution in Eqs. 3.12 and 3.13 is given by

$$R(x, y, z) = b \cdot (n(x, y, z) \cdot p(x, y, z) - n_0 p_0) - R_{\text{light}} \tag{3.22}$$

3.1.6 Numerical iteration method

The numerical iteration method used to solve Eqs. 3.11, 3.12, 3.13, and 3.16 should be discussed briefly. Although there exist many different approaches for the numerical solution of this system of nonlinear algebraic equations, it was decided to use a successive over relaxation (SOR) Newton method because of the easy implementation and the advantage that Eqs. 3.11, 3.12, and 3.13 can be sequentially used to find the solution.[77] A derivation of this and other methods in detail is for example given by Selberherr.[77] Identifying Eqs. 3.11, 3.12, and 3.13 with $F_1(\phi, n, p) = 0$, $F_2(\phi, n, p) = 0$, and $F_3(\phi, n, p) = 0$, respectively, the variation of the variables $\delta\phi^{\text{k}} = \phi^{\text{k+1}} - \phi^{\text{k}}$, $\delta n^{\text{k}} = n^{\text{k+1}} - n^{\text{k}}$, and $\delta p^{\text{k}} = p^{\text{k+1}} - p^{\text{k}}$ of the k-th iteration step of the SOR Newton method are evaluated by [77]

$$\begin{aligned}
\delta\phi^{\text{k,m+1}} &= -\frac{\omega \cdot F_1(\phi^{\text{k}}, n^{\text{k}} + \delta n^{\text{k,m}}, p^{\text{k}} + \delta p^{\text{k,m}})}{\frac{\partial F_1^{\text{k}}}{\partial \phi}} \\
\delta n^{\text{k,m+1}} &= -\frac{\omega \cdot F_2(\phi^{\text{k}} + \delta\phi^{\text{k,m+1}}, n^{\text{k}}, p^{\text{k}} + \delta p^{\text{k,m}})}{\frac{\partial F_2^{\text{k}}}{\partial n}} \\
\delta p^{\text{k,m+1}} &= -\frac{\omega \cdot F_3(\phi^{\text{k}} + \delta\phi^{\text{k,m+1}}, n^{\text{k}} + \delta n^{\text{k,m+1}}, p^{\text{k}})}{\frac{\partial F_3^{\text{k}}}{\partial p}}
\end{aligned} \tag{3.23}$$

where ω is a relaxation parameter. This means that an "inner" iteration (index m) has to be performed for each Newton step k.

3.1.7 Design of the mesh

In order to obtain the potential near the surface with the required spatial accuracy, rather small distances between the points of the mesh used in the finite difference

calculation are needed (in the order of 0.1 nm). However, for lower doped semiconductors the band bending may extend deep into the semiconductor (up to µm). Hence, the mesh needs to cover a volume large enough to include the full decay of the potential. In principle one could use a fully equidistant mesh, but the number of points needed would make the calculation impractical. At large distances (x, y, and z) from the semiconductor surface area facing the tip, the potential changes almost linearly and hence the points of the mesh can be increasingly separated in space. Along all three directions, equidistant points are used close to the surface area facing the tip. At larger distances, the point separation of the mesh is increased, until the mesh volume is sufficiently large. Figure 3.2(a) illustrates a three-dimensional view of a mesh similar to that used in the computations. The mesh points are located at the intersections of the lines. For the sake of clarity, the mesh consists only of one eighth of the mesh points used in the computation. Additionally, the points in the vacuum are hidden. Figure 3.2(b) represents a cross-sectional view along the central x-y plane (including mesh points in the vacuum). This mesh provides a full three-dimensional finite difference calculation, where any tip shape can be modeled. It is not limited to hyperbolically-shaped tips, as previously used.[70]

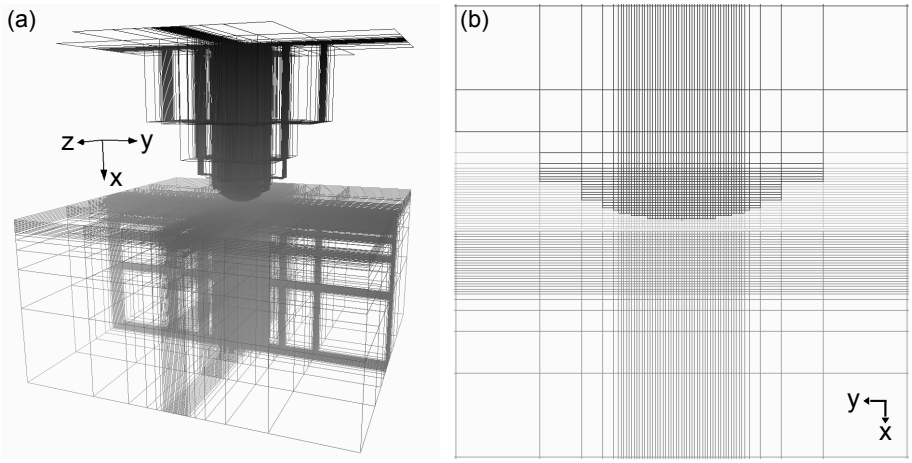

Figure 3.2: (a) Three-dimensional view of a mesh, similar to that used in the computations. The mesh points are located at the intersections of the lines. For the sake of clarity, the mesh consists only of one eighth of the mesh points used in the computation. Additionally, the points in the vacuum are hidden. (b) Cross-sectional view of the central x-y plane (isometric projection) including the mesh points in the vacuum. [P1], © 2015, American Physical Society.

3.2 Calculation of the tunnel current beyond the effective mass approximation

The calculation of the tunnel current density is based on the tunneling model presented in Chap. 2.3.4. The current density is given by Eqs. 2.73 and 2.74. It depends on the band edge energies, obtained from the solution of the Poisson equation, along the axis perpendicular to the sample surface (x-axis in the electrostatic calculation), through the tip apex.

These two equations cover the tunneling of electrons out of the valence band (Eq. 2.73) and out of an electron accumulation zone in the conduction band (Eq. 2.74) into the empty tip states as well as of electrons in the tip into the empty conduction band states (Eq. 2.74) or into a hole accumulation zone in the valence band (Eq. 2.73).

The total tunnel current I is the sum of all current density contributions multiplied by the tunnel area A_{tunnel}: [78]

$$I = (J_{\mathrm{V}} + J_{\mathrm{C}}) \times A_{\mathrm{tunnel}} \tag{3.24}$$

This approach assumes parabolic bands and does not incorporate the tunneling of light-excited carriers. Hence, the model is extended here in order to incorporate the concentrations of both minority and majority carriers (including light-excited carriers) obtained from the solution of the continuity equations. From these carrier concentrations the quasi Fermi levels $E_{\mathrm{FQ,C}}$ and $E_{\mathrm{FQ,V}}$ at the surface are derived. $E_{\mathrm{FQ,C}}$ ($E_{\mathrm{FQ,V}}$) is the upper (lower) limit for the energy of the electrons (holes) in the conduction band (valence band). These electrons (holes) can tunnel from the conduction band (valence band) into the tip. Hence, the quasi Fermi levels replace the upper limit of the first integral in Eqs. 2.73 and 2.74.

The quasi Fermi levels have to be determined precisely, because they affect critically the tunnel current density. Calculating the quasi Fermi levels on the basis of Eqs. 2.91 and 2.92 using the carrier densities $n(x, y, z)$ and $p(x, y, z)$ is only accurate enough for moderate carrier concentrations ($n\,(x, y, z) < N_{\mathrm{C}}$ and $p\,(x, y, z) < N_{\mathrm{V}}$), since the conduction band dispersion deviates from its parabolic approximation almost directly at E_{C}. Hence, for higher carrier concentrations one needs to integrate the calculated density of states [DOS(E)] of the investigated semiconductor (i.e. GaAs), e.g., taken from Chelikowsky and Cohen [81, 82]

$$n' = \int_{E_{\mathrm{C}}}^{\infty} dE \mathrm{DOS}(E) f_{\mathrm{S}}(E - E_{\mathrm{FQ,C}}) \tag{3.25}$$

$$p' = \int_{-\infty}^{E_\mathrm{V}} dE \mathrm{DOS}(E) f_\mathrm{S}(E_\mathrm{FQ,V} - E) \tag{3.26}$$

and numerically solve these integrals for $E_\mathrm{FQ,C}$ and $E_\mathrm{FQ,V}$, such that n' (or p') equals the carrier concentration $n(x, y, z)$ (or $p(x, y, z)$) at the surface below the tip apex. The Fermi-Dirac distribution of the semiconductor $f_\mathrm{S}(E)$ is approximated by a step function here. The same approximation is already used in the derivation of the tunnel current (Eqs. 2.73 and 2.74) and hence does not restrict the validity further.[65]

Additionally, the effective masses $m_\mathrm{eff,V}$ and $m_\mathrm{eff,C}$ of the holes and electrons, respectively, are taken to be energy-dependent. By substituting $E_\mathrm{FQ,C}$ ($E_\mathrm{FQ,V}$) and $n(x, y, z)$ ($p(x, y, z)$) into Eq. 2.91 (Eq. 2.92), it can be solved for new quasi effective masses $m_\mathrm{effq,C}$ ($m_\mathrm{effq,V}$), replacing $m_\mathrm{eff,C}$ ($m_\mathrm{eff,V}$). The resulting quasi effective masses and quasi Fermi levels are then used to calculate the tunnel current density.

Chapter 4

Experimental techniques

4.1 Tip preparation

For all measurements of GaAs and GaN in this thesis, tungsten tips were used. This becomes particularly important for experiments under light irradiation: Tungsten is known to exhibit negligible tip-enhanced raman spectroscopy effects, due to the plasmon resonance frequency that is in deep infrared, and thus cannot be excited by the laser wave length used in the experiment.[83, 84]

The tips were produced by electrochemical etching with sodium hydroxide solution. A ring of platinum wire is used as cathode. Within the Pt ring, a thin film of NaOH solution is spanned. A tungsten wire with a diameter of 0.25 mm is penetrating the NaOH film at the midpoint of the platinum ring, such that a 3-4 mm piece of the tungsten wire is cut off through the etching process. This piece forms the tip. With the tungsten wire as anode, an applied voltage initiates the etching process as follows.[85]

$$\begin{aligned} \text{Anode:} \quad & \mathrm{W}_{(s)} + 8(\mathrm{OH})^- \rightarrow \mathrm{WO}_4^{2-} + 4\mathrm{H_2O} + 6\mathrm{e}^- \\ \text{Cathode:} \quad & 6\mathrm{H_2O} + 6\mathrm{e}^- \rightarrow 3\mathrm{H}_{2(g)} + 6(\mathrm{OH})^- \\ \text{Total:} \quad & W_{(s)} + 2(\mathrm{OH})^- + 2\mathrm{H_2O} \rightarrow \mathrm{WO}_4^{2-} + 3\mathrm{H}_{2(g)} \end{aligned} \tag{4.1}$$

In order to keep the tip free of undesired reaction products that could coat the tip and thus worsen the electrical conductivity, short pulses of reversed bias are applied to the tip during the etching process.[86] After the etching process, the tip is cleaned in distilled water and ethanol, followed by the direct transfer into the vacuum chamber of the scanning tunneling microscope in order to minimize further oxidation in air. Further in-situ treatments, like heating or electron bombardment,[58] is omitted so as not to damage the very sharp foremost end of the tip. Hence, the tip is ready to use right after the transfer to vacuum.

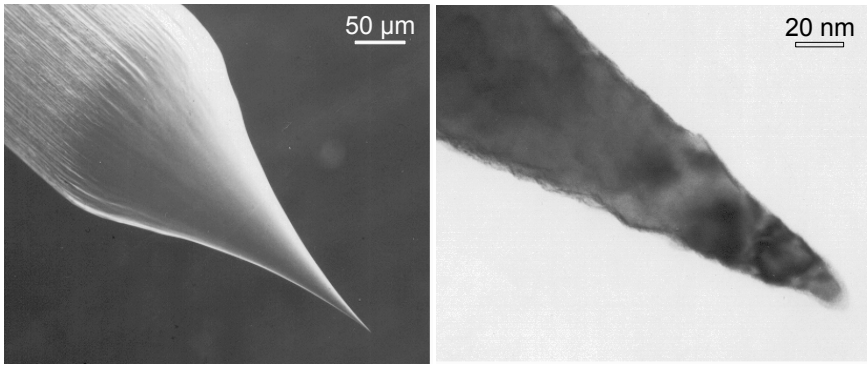

Figure 4.1: SEM (left) and TEM (right) image of tungsten tips, which were etched by our setup previously reveal a common radius of curvature of approximately 10 nm. Images are taken from Ref. [87, 88].

As already shown (e.g. by Eq. 2.38), the radius of curvature of the tip apex is notably affecting the tunnel current. Hence, a quantitative analysis requires the determination of this parameter, first. SEM and TEM images of tungsten tips, which were etched by our setup previously, like those shown in Fig. 4.1, reveal a common radius of curvature of approximately 10 nm.[87, 88] This value was used for all latter simulations of STS measurements on GaAs and GaN surfaces.

For measurements on InN samples, Pt-Ir tips ($Pt_{0.8}Ir_{0.2}$) were used, since the work-function of this alloy ($\approx 5.4\,eV$) is closer to the very large electron affinity of InN ($\approx 5.8\,eV$).[33] The tips were purchased from Agilent Technologies (no. N9801A). They were also manufactured by electrochemical etching and exhibited significant larger radii of curvature at the tip apex as compared to the tungsten tips etched with our setup. SEM images revealed a common radius of curvature of about 100 nm.[89] This value was used for all latter simulations of STS on InN surfaces.

4.2 Sample preparation and cleavage

All samples used in this thesis where investigated by cross-sectional scanning tunneling microscopy at room temperature. This method requires thin samples that can easily be cleaved in-situ. Therefore, the samples were cut from wafers into rectangular pieces of 3-4 mm width and 5-6 mm height. Subsequently, the samples were grinded and polished to a thickness of $\sim 100\,\mu m$. Electrical contacting was achieved by sputtering a layer of gold onto one half of the samples followed

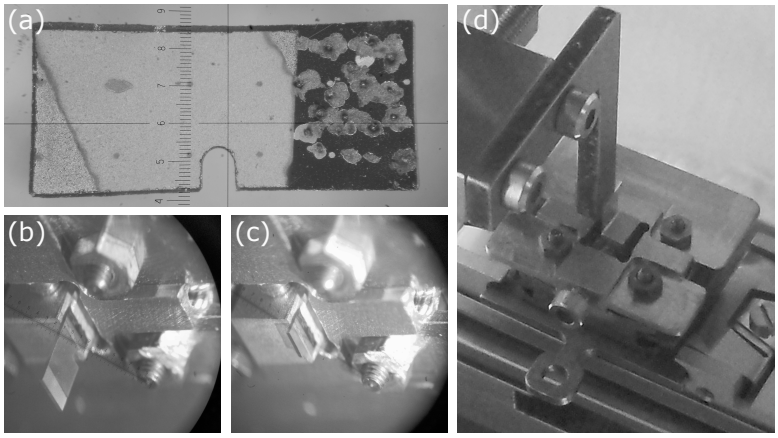

Figure 4.2: (a) A ready-prepared GaN sample, cut from a GaN wafers into a rectangular piece of 3-4 mm width and 5-6 mm height. The sample was grinded and polished to a thickness of $\sim 100\,\mu$m. Electrical contacting was achieved by sputtering a layer of gold onto one half of the sample followed by inducing electrical discharges in the region of the gold layer in order to merge the gold with the underlying semiconductor. (b) A GaN sample glued on a metal cube and mounted on the specimen holder. (c) The same sample after the cleavage procedure. Note that a flat cleavage surface was formed exactly at the position of the small slit, as desired. (d) In-situ cleavage tool exerts a uniform pressure on the sample and guarantees the best possible cleavage result.

by inducing electrical discharges in the region of the gold layer in order to merge the gold with the underlying semiconductor. The formation of a flat cleave plane is supported by small indented spots and a slit at one side of the samples (cf. Fig. 4.2(a)). The such prepared samples were glued (with an electrically conducting two-component adhesive) to a metal cube and finally mounted on the specimen holder (cf. Fig. 4.2(b)).

All samples investigated by XSTM/XSTS were cleaved in UHV (in-situ) at a pressure of 1×10^{-10} mbar, to obtain clean, contamination free surfaces. For an optimal, atomically flat cleavage plane, the cleavage tool (cf. Fig. 4.2(d)) exerts an uniform pressure on the sample. A freshly cleaved sample is shown in Fig. 4.2(c).

4.3 Sample properties

4.3.1 GaAs

The GaAs samples were cut from a commercial p-type GaAs(001) wafer with a Zn doping. The hole concentration was (1-2) $\times 10^{18}\,\mathrm{cm}^{-3}$. The samples were cleaved such that clean, non-polar GaAs(110) surfaces were obtained.

4.3.2 GaN

The GaN samples investigated in the experiments consisted of n-type GaN layers (carrier concentration of $3{\times}10^{18}$ cm^{-3}), epitaxially grown on a free-standing GaN(0001) substrate by MOCVD at 1050 °C. The samples were cleaved such that contamination free GaN($10\bar{1}0$), non-polar m-plane surfaces were obtained. Thus, the measurements were performed in the cross-section on MOCVD grown GaN layers.

4.3.3 InN

The InN samples investigated in this thesis were thick (1–2 µm) InN layers grown in c-direction on free-standing GaN substrates. The growth was performed using plasma-assisted molecular beam epitaxy. The GaN substrate and the InN layers exhibited an n-type conductivity with a carrier concentration of a few $10^{18}\,\mathrm{cm}^{-3}$. The samples for cross-sectional STM measurements were cleaved such that clean ($10\bar{1}0$), m-plane surfaces were obtained.

4.4 Experimental techniques for light-excited scanning tunneling spectroscopy

For light-excited scanning tunneling spectroscopy measurements,[90] the sample was illuminated with a $(0.95 \pm 0.05)\,\mathrm{mW}$ diode laser through a window flange at an angle of incidence of (62±3)°. A wavelength of 785 nm (corresponding to an energy of 1.58 eV, which is larger than the band gap) is used. With the help of two micrometer screws, the beam direction could be adjusted precisely in order to hit the sample exactly at the tip position (see Fig. 4.3). The focussing of the beam spot was achieved by a built-in lens directly in front of the laser. The spot size

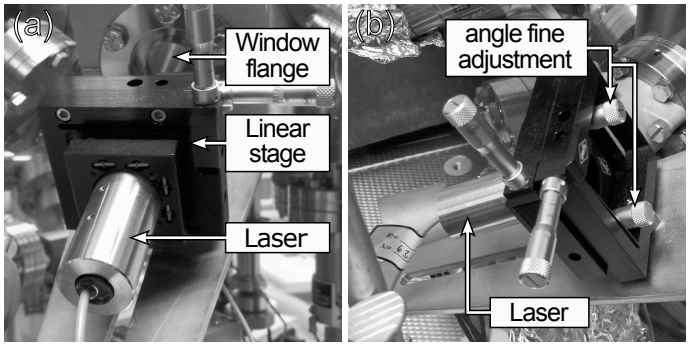

Figure 4.3: (a) Laser mounted on a linear stage at the window flange of the STM chamber. (b) 90° rotated view of the laser and the linear stage. With the help of the inner micrometer screws, the fine adjustment of the spot position on the sample is achieved. The outer micrometer screws are used for coarse adjustments.

was measured in units of the width of the sample, which was determined previously with an calibrated optical microscope. The smallest focus, which could be achieved was elliptical (due to the inclined incident angle) with major and minor axes of (50±10) and (100±20) µm. The irradiance of the laser beam was furthermore weakened by the transmission through the lens, the window flange and the reflection on the sample. The reflection at the sample's surface (i.e. GaAs) was calculated for an incident angle of (62±3)° to (30.5±0.5)% and the losses at the window flange and lenses to (7±1)%. Hence, (60.1±1)% of the original irradiance is deposited in the GaAs sample. This corresponds to an average irradiance of $(1.45\pm0.44)\times10^5\,\mathrm{Wm}^{-2}$.

In contrast to many other experiments, no mechanical chopper was used, since the laser intensity may be influenced by a partially concealed laser beam (laser intensity changes gradually at the chopper edges). Hence, during the acquisition of current-voltage spectra, the laser was electrically modulated by the STS control electronics.[91] In contrast to standard current-voltage spectra, the current with and without illumination was measured consecutively at each voltage step. Each of these steps took 1280 µs, during which first the laser was turned on for 180 µs only to minimize thermal drift. Second, the current without illumination was then acquired 800 µs after turning off the laser. Importantly, the current-voltage spectra with and without illumination were hence probed at the same tip-sample separation, which was fixed by the set voltage and current without illumination.

4.5 Cross-sectional transmission electron microscopy

The InN samples were also investigated in cross-section by TEM. The specimens were prepared by ion beam milling. A final cleaning of the TEM specimens was performed with low energy Ar-ion bombardment (0.5 eV) at liquid N_2 temperature using a Fischione Nanomill system. Structural investigations were performed using a FEI Titan TEM equipped with a spherical aberration corrector at the image plane.

Chapter 5

Light-excited scanning tunneling spectroscopy on the GaAs(110) surface

This chapter is adapted from [P1] (see list of own publications, p. 119),

5.1 Introduction

The efficiency of solar cell and optoelectronic devices is closely connected to the nanoscale distribution of charge carriers. For example, defects can give rise to non-radiative carrier recombination centers, reducing the charge carrier concentration locally.[45, 46] Such effects are detrimental to both the electron-light and light-electron conversion efficiencies in optoelectronic and solar cell devices, respectively. In order to understand the physical processes involved at the atomic scale, the materials used in the device structures need to be investigated simultaneously under illumination and with atomic resolution.

Photo-excited scanning tunneling spectroscopy[92] is ideally suited to probe the illumination-induced local surface photovoltage, band bending, carrier concentration, and the electrostatic potential distribution with atomic resolution.[45, 46, 47, 48, 49, 50, 51, 52, 53] For a quantitative analysis, particularly of the local charge carrier concentration and redistribution, a fundamental physical understanding and theoretical modeling of the photo-excited tunneling spectra would be needed. Grafström pointed out that a realistic model "should allow the various quantities involved such as recombination rates and tip-induced band bending to be identified

more reliably and should put the interpretation of spatial variations of the measurement signal on a more solid ground."[93] However, to date mostly qualitative explanations attribute the photo-excited tunneling spectra to changes of the band bending under illumination.[47, 50, 51, 69, 94, 95, 96, 97, 98] Reliable quantitative simulations of and fits to photo-excited tunneling spectra are still lacking.

Prins *et al.*[99], Sommerhalter *et al.*[100], and Vu *et al.*[101] developed first approaches to the problem. Prins *et al.* focused on pinned surfaces with a high density of surface gap states, but did not take into account tunneling into the conduction and out of the valence band. Sommerhalter *et al.* modeled unpinned surfaces without surface gap states using a one-dimensional metal-insulator-semiconductor model. Both approximated the tunnel current with a thermionic emission current model, which according to Sommerhalter *et al.* represents a simplification compared to the earlier method presented by Feenstra and Stroscio.[66] In addition the one-dimensional model used by Sommerhalter *et al.* as well as the planar one-dimensional GaAs-insulator-Au tunnel contact measured and simulated by Vu *et al.* do not take into account the localized nature of the STM tip, which significantly affects the electric field distribution near the tip apex and thus band bending.[70]

The universally applicable and detailed three-dimensional quantitative description of the effect of illumination on the tunnel current developed in Chap. 3 will be used to calculate the tunnel current under light irradiation and will be compared quantitatively to laser-excited tunnel spectra measured from GaAs(110) surfaces. A detailed discussion of the different tunnel current contributions with and without laser excitation is provided. This analysis demonstrates that the modeling developed in Chap. 3 provides a comprehensive quantitative description of photo-excited tunneling spectra.

5.2 Experimental results

The freshly cleaved, *p*-doped GaAs(110) surface consisted of very large atomically flat terraces separated by steps. An example is shown in Fig. 5.1. The step edges along the $[\bar{1}10]$ direction where shown to induce defect states in the band gap.[102] However, the spatial extension of these states was found to be in the order of a few nanometers around the step edge[102] and thus can be neglected for our measurement in the middle of the 500 nm or more wide terraces. Only a very low, typical[103, 104, 105], defect concentration of $\lesssim 5 \times 10^{10}\,\mathrm{cm}^{-2}$ was present. Thus, *no* relevant concentrations of *extrinsic* surface states and hence no *extrinsic* pinning can be expected.[106]

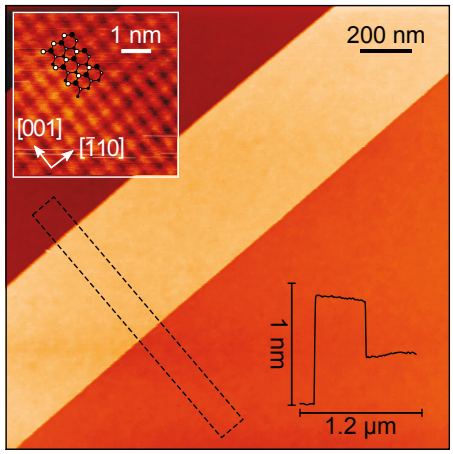

Figure 5.1: STM image of the occupied states of the non-polar GaAs(110) cleave surface that was used for the light-excited STS experiments. The image was acquired with a constant current of 150 pA and a sample voltage of -1.9 V. It consisted of very large atomically flat terraces separated by steps. The averaged height profile, shown at the lower right corner of the image was measured at the region indicated by a dashed rectangle and serves as height scale for the image. Inset: Atomically resolved STM image measured at one of the terraces. (also occupied states, same setpoint) Note, the steps formed along the [$\bar{1}$10] direction.

Figure 5.2 shows two current-voltage spectra obtained simultaneously at identical tip-sample separations using the experimental setup described in Sec. 4.4. The spectrum shown with (black) triangles has been measured in dark. The (red) squares represent the spectrum measured under illumination. At positive voltages both spectra coincide and have identical onset voltages of about +1.7 V. However, at negative voltages, the current measured under illumination is higher than that measured without light. In addition, the illumination shifts the onset voltage of the spectrum from -0.6 V (dark) to -0.4 V (illuminated).

The two spectra shown are representative of a larger set of measurements done on several *p*-GaAs(110) surfaces. The common features of these measurements are: (i) no change of the tunnel current at positive voltages by illumination, (ii) illumination increases the tunnel current at negative voltages, and (iii) the onset voltage of the tunnel current at negative voltages is always close to -0.4 V under illumination using a laser energy of 1.58 eV (785 nm). Note, under dark conditions the onset voltage for tunneling at negative voltages naturally shifts downward for lower doped samples due to the increasing band bending.[107]

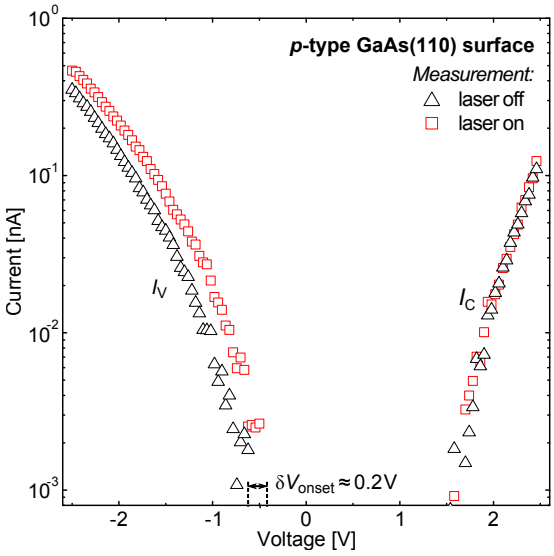

Figure 5.2: Current-voltage spectra obtained on a *p*-doped GaAs(110) surface with (red squares) and without (black triangles) illumination for identical tip-sample separations. The setpoint is -2.0 V and 150 pA (without illumination). The laser excitation increases the tunnel current only at negative sample voltages. At positive voltages no effect is detectable. [P1], © 2015, American Physical Society.

5.3 Qualitative interpretation

In order to interpret laser-excited tunneling spectroscopy, such as the example shown in Fig. 5.2, a qualitative description is given, first. It should be recalled that for *p*-doped GaAs(110) surfaces without laser excitation, the current at positive voltages arises from electrons tunneling into the empty conduction band states (conduction band current, I_C). At negative voltages, the electrons tunnel from the filled valence band states into the empty tip states (valence band current, I_V).[13] Due to the negligible concentration of surface states within the fundamental band gap and the moderate doping concentration of $2 \times 10^{18}\,\mathrm{cm}^{-3}$, the applied electric field between the tip and the sample is not fully screened at the surface and penetrates into the semiconductor. This tip-induced band bending[66, 108, 109] is qualitatively reduced with increasing free charge carrier concentration.[13, 107, 110] Hence, the onset voltages contain information about the distribution of charge carriers.[111, 112]

Figure 5.2 shows that the onset voltage of the conduction band current (at positive sample voltages) remains unchanged under illumination. This is due to the upward band bending, resulting in accumulation of majority carriers at the surface of the semiconductor. The concentration of light-excited majority carriers is smaller than or roughly equal to that of thermally generated majority charge carriers (as shown below). Therefore, the upward band bending is not altered significantly and the tunnel current remains essentially unchanged.

In contrast, the onset voltage of the valence band current (negative sample voltages) is shifted towards smaller negative voltages by $\delta V_{\text{onset}} \approx +0.2\,\text{V}$ under illumination (Fig. 5.2). This indicates the presence of light-excited minority carriers at the semiconductor's surface: Due to the tip-induced downward band bending, the minority carriers (electrons) will move towards the surface, while the majority carriers (holes) drift deeper into the bulk material. The concentration of light-excited minority carriers is orders of magnitude higher than that of thermally generated *minority* carriers. On the one hand, this enhances the screening of the electric field and thus reduces the downward band bending at negative voltages under illumination. Reduced band bending also results in an increased density of valence band states available for tunneling and hence a higher tunnel current. On the other hand, light-excited minority charge carriers at the semiconductor surface can tunnel into the tip, increasing the tunnel current. The relative magnitude of these two effects is unclear and needs to be investigated quantitatively using the model developed in Chap. 3.

5.4 Results and discussion

In this section, the measured spectra, as illustrated in Fig. 5.2, are analyzed and discussed. The quantitative description developed in Chap. 3 is applied to compute the tunnel currents under different physical assumptions and parameters as well as with and without illumination. The results of the computation are fitted to the measured spectra, in order to test the validity of the quantitative description of photo-excited STS.

For the particular case of the GaAs(110) surface, a quantitative physical explanation of the measured tunnel spectra requires the inclusion of intrinsic surface states energetically located within the bands. The physical effect of the surface states on the illuminated tunneling spectra is described with two different models. For both models the tunnel currents are computed and fitted to the measured spectra, followed by a comparative discussion.

5.4.1 Effect of GaAs(110) surface states on the tunnel spectroscopy

At this stage the origin of the relevant tunnel current contributions is recalled first, followed by a discussion of the effect of surface states. Electrons can tunnel from the valence band into the tip, if the energy of the highest occupied state of the tip ($E_{\mathrm{F,tip}} = E_{\mathrm{F}}+eV$) is below the bulk valence band edge of the semiconductor. On the other hand, if $E_{\mathrm{F,tip}}$ is energetically above the bulk conduction band edge, tunneling of electrons from the tip into the conduction band is possible. These two processes usually form the main contributions of the tunnel current, denoted by I_{V} and I_{C}, respectively. In addition, an accumulation current I_{acc} can occur for n-type (p-type) semiconductors, if the conduction (valence) band is bent below (above) E_{F} near the surface (majority carrier accumulation).[13] For n-type surfaces the accumulation current arising from the electron accumulation zone in the conduction band I_{acc} was derived to be at least one order to magnitude larger than I_{V}. However, this was not confirmed by measurements on n-doped GaAs(110) surfaces.[13] Jäger *et al.* [13] and Ishida *et al.* [15] explained this discrepancy by the presence of surface states.

The GaAs(110) surface has two relevant intrinsic surface states located energetically within the bands. The filled one is close to the valence band edge and corresponds to the dangling bond above the As surface atoms. It is commonly labeled A_5 and has its energetic maximum at the Γ-point of the surface Brillouin zone. The empty one is also a dangling bond state, but localized above the Ga surface atoms. It is energetically slightly above the conduction band edge with its minimum at the edge of the surface Brillouin zone ($\overline{X}$-point). It is commonly labeled C_3.[113, 114, 115] All other surface states are deeper within the bands and hence not relevant here.[113, 116, 117] For the explanation of the discrepancy between measured and calculated accumulation current I_{acc}, only the empty C_3 surface state is important: Jäger *et al.* suggested that the accumulation current is suppressed, because the tip cannot accommodate conduction band electrons tunneling out of the empty C_3 surface state due to the nonzero parallel momentum.[13] Ishida *et al.* assumed in addition that the C_3 surface state can be partially filled, effectively pinning the Fermi level. This reduces the charge density in the accumulation layer and hence the magnitude of I_{acc}.[15]

Measurements in this paper were performed on p-doped - not on n-type - GaAs(110) surfaces. The p-type GaAs(110) surface exhibits a Fermi level near the valence band edge. Without illumination, the minority carrier concentration is too low to support an inversion layer (i.e. "accumulation" of electrons in the conduction

band) near the surface under tunneling conditions.[13] Hence, in the dark no current could be supported from electrons tunneling out of the conduction band. The situation changes under illumination, when light-excited electrons are generated. These electrons behave like thermally excited electrons in the conduction band of an n-type sample. Thus, for p-type samples, a tunnel current similar to the accumulation current I_{acc} on an n-type sample arises from the tunneling of light-excited electrons out of the conduction band at negative sample voltages. This *photo-induced tunnel current* is denoted I_{photo} in the following (not to be confused with the current arising from the photoelectric effect).

In analogy to the explanations of the suppressed accumulation current on n-type GaAs(110) in the dark[13, 15], the photo-induced tunnel current is modeled under two different physical conditions: full suppression of the accumulation current and hence the photo-induced tunnel current and a reduced electron accumulation due to surface-state-limited band bending.

5.4.2 Parameters of the calculation

For the calculations a hyperbolically-shaped tip with a radius of curvature of 10 nm, an apex angle of 45°, and a work function of 4.5 eV is assumed. For the GaAs sample a p-type doping of $2 \times 10^{18}\,\mathrm{cm}^{-3}$, an electron affinity of 4.07 eV, and bulk effective masses are used. The tip-sample separation was used as the only fitting parameter to adjust the calculated tunnel current to the measurement under dark conditions. The best fit was obtained for a tip-sample separation of 0.925 nm. The same value was used for all further calculations under illumination, since the spectra were measured at identical tip-sample separations. For the light-excited charge carriers a minority carrier lifetime of $5 \times 10^{-9}\,\mathrm{s}$ is used for Zn-doped GaAs following Ref. [118, 119] as well as hole and electron mobility values of 150 and $2400\,\mathrm{cm}^2\mathrm{V}^{-1}\mathrm{s}^{-1}$, respectively.[120] The irradiance of the incident laser beam was used as the only fitting parameter for the calculation of the illuminated curves. The best fit values will be then compared with the experimentally used laser irradiance.

5.4.3 Results of the calculation

Full suppression of electron tunneling from the conduction band accumulation layer

In this section it is assumed that the light-excited carriers in the conduction band of our p-type GaAs(110) sample cannot tunnel into the tip ($I_{\mathrm{photo}} = 0$). The

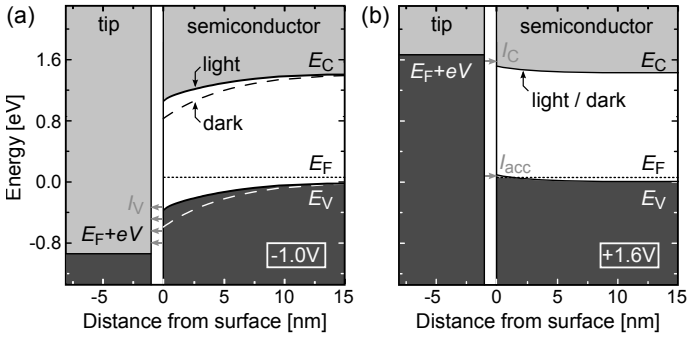

Figure 5.3: Calculated valence (E_V) and conduction (E_C) band-edge positions as a function of the distance from the semiconductor's surface for (a) negative (-1.0 V) and (b) positive (+1.6 V) voltages applied to the sample. The band-edge positions were calculated on the assumption that the surface states do not influence the band bending. The sample is shown on the right side at positive distance values. The Fermi energy (E_F) is close to the valence band edge in the bulk. The tip with its Fermi energy at E_F+eV is shown on the left side. The dark shaded (light shaded) areas represent filled (empty) states. The band gap and the vacuum gap (tunnel barrier) between the surface (at 0 nm) and the tip position (at -0.925 nm) are shown in white. Dashed lines show the semiconductor's band edges without illumination, while solid lines correspond to the illuminated case. Note the reduced band bending under illumination. [P1], © 2015, American Physical Society.

computational results are presented in Figs. 5.3, 5.4, and 5.5. Figure 5.3 illustrates the band edge positions at the central axis through the tip as a function of the distance from the semiconductor surface for voltages of (a) $-1.0\,\mathrm{V}$ and (b) $+1.6\,\mathrm{V}$ without (dashed lines) and with (solid lines) illumination. Figures 5.4 and 5.5 show cross-sectional two-dimensional plots of (a) the electrostatic potential, (b) the electron concentration, and (c) the hole concentration through the central y-x plane for $-1.5\,\mathrm{V}$ and $+1.5\,\mathrm{V}$, respectively, without (left frames) and with (central frames) illumination. The results correspond to the best fit of the model of full suppression of the photo-induced tunnel current to the experimental data, using a irradiance of the laser of $(22\pm5)\times10^5\,\mathrm{Wm}^{-2}$. Note that the calculated tunnel current for the best fitting solution will be shown and discussed in Sec. 5.4.4.

For negative voltages and under illumination, light-excited electrons accumulate near the surface (see Fig. 5.4(b2)). The electron concentration near the surface locally reaches $6 \times 10^{20}\,\mathrm{cm}^{-3}$. Note the color scale of the electron concentration

in Fig 5.4(b2) is reduced by a factor of 5×10^{-2} compared to the scale on the right side of Fig 5.4(b3). This is 300 times larger than the hole concentration in the bulk. Under dark conditions (see Fig 5.4(b1)), almost no free electrons are present and hence the density of electrons accumulating at the surface is almost zero (approximately a factor of 10^{16} smaller than under illumination. Note the color scale of the electron concentration in Fig 5.4(b1) is enhanced by a factor of 5×10^{14} to visualize the distribution.) In contrast, the hole concentration changes only slightly, when the laser is turned on (Fig. 5.4(c1) and (c2)). The accumulated photo-induced electrons are screening the tip-induced band bending. The combined effect on the electrostatic potential ϕ is illustrated in Figs. 5.4(a1), 5.4(a2), and 5.3(a). For example, at an applied voltage of $-1.0\,\mathrm{V}$, ϕ decreases from $-0.59\,\mathrm{V}$ to $-0.37\,\mathrm{V}$ when the sample is exposed to laser light. The reduced potential will, according to Eqs. (2.73), (2.74), and (3.24), lead to an increased valence band tunnel current I_V in accordance with the experimental observation (Fig. 5.2).

For positive voltages, the screening is primarily determined by the thermally-generated holes (accumulating at the surface) (Fig. 5.5(c1) and (c2)), since the concentration of light-excited holes is almost two orders of magnitude lower. The light-excited electrons move away from the surface (Fig. 5.5(b1) and (b2)). Hence, the electron concentration near the surface is small, regardless of whether the laser is switched on or off. Thus, no significant change in the tip-induced band bending can be observed for the dark and illuminated cases in Figs. 5.3(b) and 5.5(a1) and (a2). In consequence, no change in the tunnel current occurs at positive voltages in agreement with the experimental observation.

Surface-state-limited band bending

In this section it is assumed that (i) the light-excited electrons can partially occupy the empty C_3 surface state, but a direct tunneling out of the surface state is negligible,[101] and (ii) light-excited carriers can tunnel out of the conduction band ($|I_\mathrm{photo}| > 0$). In analogy to Ref. [15] the C_3 surface state is modeled by a Gaussian distribution peaking at an energy E_SS of 0.33 eV above the conduction band minimum with a FWHM of 0.25 eV. A surface state density of $4.4 \times 10^{14}\,\mathrm{cm}^{-2}$ is assumed, corresponding to one state per surface cation.[15] The surface state is electrically neutral, if it is positioned completely above the quasi Fermi level of the conduction band ($E_\mathrm{FQ,C}$). For positive voltages and thus upward band bending, the surface state will remain unoccupied and the band bending does not change. For negative voltages and downward bend bending, the tail of the Gaussian distribution will move below the quasi Fermi energy and thus create a negative surface charge distribution. This additionally screens the tip-induced band bending and hence

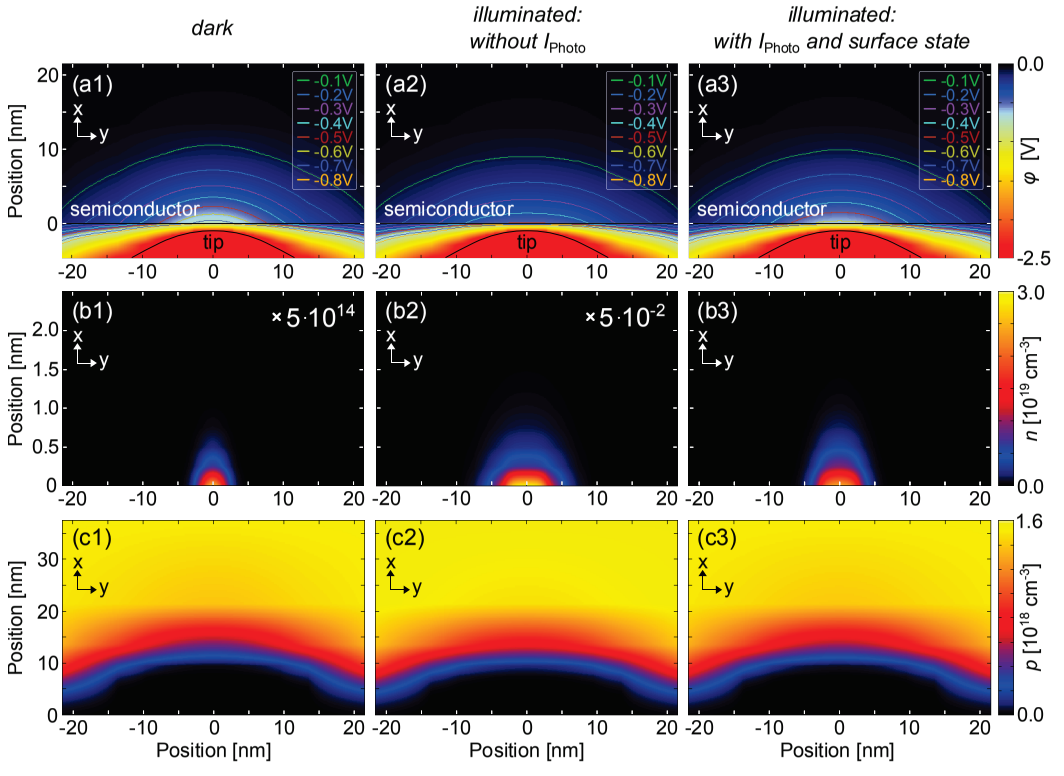

Figure 5.4: Cross-sectional plots of (a) the electrostatic potential ϕ of the tip-vacuum-semiconductor system, (b) the electron concentration n, and (c) the hole concentration p (in the semiconductor only) for a sample voltage of -1.5 V without illumination (left column), with illumination and no tunneling of photo-induced electrons in the surface accumulation layer $I_{\mathrm{Photo}} = 0$ (central column), and with illumination, photo-induced tunnel current, and surface-state limited band bending (right column). The equipotential lines in (a) range from -0.1 V to -0.8 V in steps of 0.1 V. [P1], © 2015, American Physical Society.

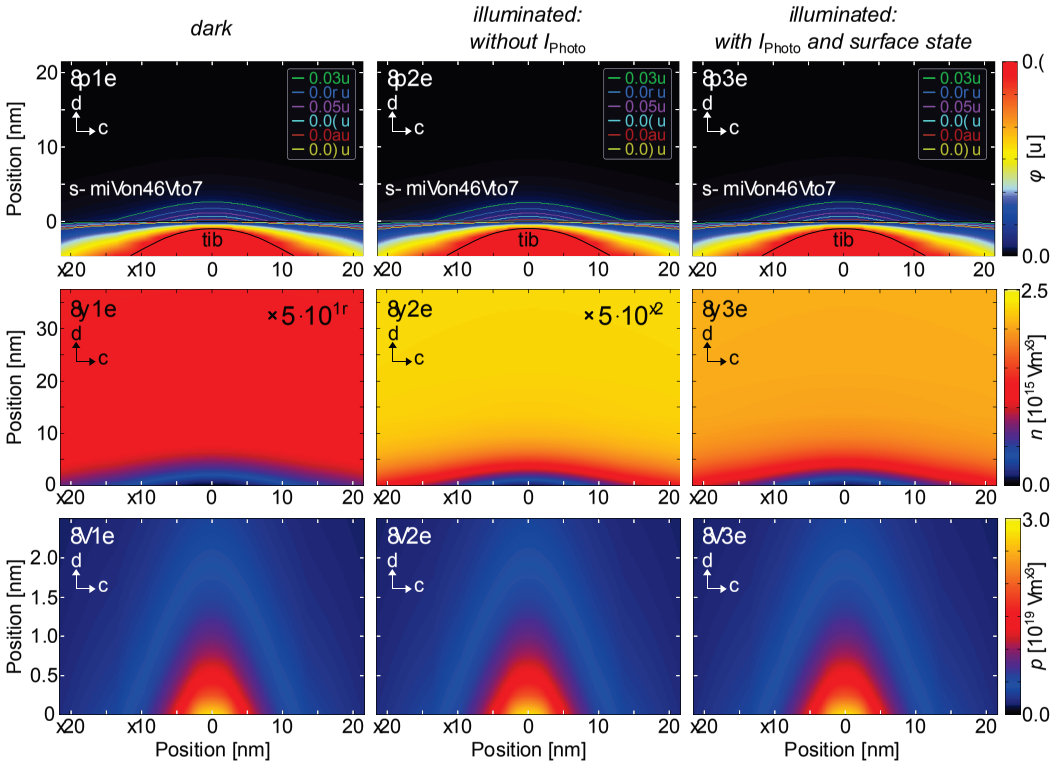

Figure 5.5: Cross-sectional plots of (a) the electrostatic potential ϕ of the tip-vacuum-semiconductor system, (b) the electron concentration n, and (c) the hole concentration p (in the semiconductor only) for a sample voltage of $+1.5\,\mathrm{V}$ without illumination (left column), with illumination and no tunneling of photo-induced electrons in the surface accumulation layer $I_{\mathrm{Photo}} = 0$ (central column), and with illumination, photo-induced tunnel current, and surface-state limited band bending (right column). The equipotential lines in (a) range from $0.03\,\mathrm{V}$ to $0.08\,\mathrm{V}$ in steps of $0.01\,\mathrm{V}$. [P1], © 2015, American Physical Society.

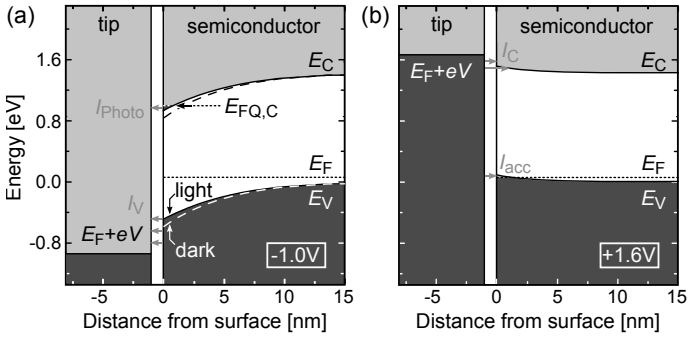

Figure 5.6: As for Fig. 5.3, but calculated assuming that the empty surface state is partially filled and hence limits the tip-induced band bending. Shown are the band edge positions under illumination (solid lines) and under dark conditions (dashed lines). I_{Photo} indicates the photo-induced tunnel current. [P1], © 2015, American Physical Society.

reduces the bulk electron concentration near the surface. The resulting band edge positions E_{V} and E_{C} are shown in Fig. 5.6 as a function of the distance from the surface. For comparison with the previously discussed model, the cross-sectional plots of the potential as well as electron and hole distributions are shown in the right columns of Figs. 5.4 and 5.5 for -1.5 V and +1.5 V, respectively. Again, the screening arises from electrons filling the surface state and accumulating near the surface at negative voltages and from holes accumulating near the surface at positive voltages. The photo-induced tunnel current I_{photo} arises from photo-excited electrons in the conduction band, as indicated in Fig. 5.6(a).

Figure 5.7 shows the band edge positions E_{V} and E_{C} at the surface as a function of the applied voltage under illumination. The quasi Fermi levels $E_{\mathrm{FQ,V}}$ and $E_{\mathrm{FQ,C}}$ are drawn as dotted lines. The peak position of the Gaussian distribution of the C_3 state is drawn as a solid line and denoted E_{SS}. For the purpose of illustration an energy interval of 4σ around E_{SS} indicates the energetic width of the surface state. The occupied part of the Gaussian distribution of the surface state up to $E_{\mathrm{FQ,C}}$ is indicated. Note that a partial occupation of the surface state is already sufficient to limit the tip-induced band bending.

Hence, in this model, the change of the tunnel current between the illuminated and dark case is caused by the limited band bending *and* the tunneling of light-excited electrons from the conduction band into the tip. The best fit of the surface state-limited band bending model to the experimental data is achieved using an irradiance of the laser of $(1^{+0.7}_{-0.3})\times10^5\,\mathrm{Wm}^{-2}$.

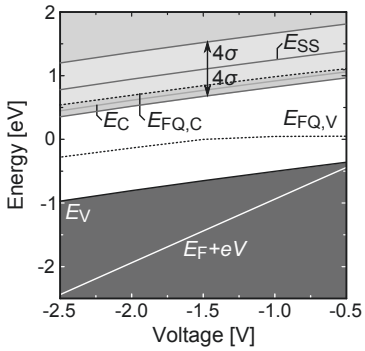

Figure 5.7: Band edge positions E_V and E_C at the surface as a function of the applied voltage under illumination. The quasi Fermi levels $E_{FQ,V}$ and $E_{FQ,C}$ are drawn as dotted lines. The peak position of the Gaussian distribution is denoted E_{SS}, while an energy interval of 4σ around E_{SS} indicates the energetic extension of the surface state. The occupied part of the Gaussian distribution of the surface state up to $E_{FQ,C}$ is indicated. [P1], © 2015, American Physical Society.

5.4.4 Comparison of the calculated and measured tunnel currents

Figure 5.8 shows the measured spectra under dark (black triangles) and illuminated (red squares) conditions taken from Fig. 5.2 together with the calculated currents (lines) under different conditions. First the spectra under dark conditions will be discussed. The calculated current, which is shown as a black solid line, represents the best fit using only the tip-sample separation as a fitting parameter (0.925 nm). This tip-sample separation is a reasonable value for STM operation. Note that the calculated tunnel current under dark conditions is identical for both models. Good agreement is found between the onset voltages of the calculated black solid curve and of the experimental data (triangles).

At this stage, the criteria for the best fit need to be briefly discussed: The theoretical foundation of the tunnel current calculation is most accurate for the smallest voltages, i.e. at the onset voltages. In addition, the onset voltages of the tunnel current are also experimentally the most accurate features. Therefore, the fits, which reproduce best the onset voltages and the initial current slope near the onset voltages were chosen. The deviation of the calculated curve from the measured data points at larger magnitudes of voltage is due to the non-parabolic bands at larger energies.[16]

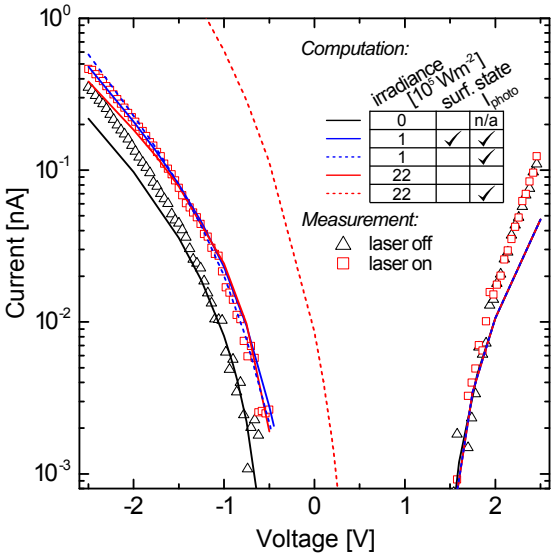

Figure 5.8: I-V curves obtained from a *p*-type GaAs sample with (red squares) and without (black triangles) illumination compared to computational results (solid and dashed lines). The fit of the current for dark conditions is represented by the black solid curve. The red solid line was calculated assuming full suppression of electron tunneling from the conduction band accumulation layer. The tunnel current at negative voltages arises from electrons tunneling out of the valence band only. The blue solid line shows the tunnel current for the case of the surface-state-limited band bending. Here the tunnel current is composed of a valence band current and a photo-induced tunnel current. The red dashed line was calculated using the same parameters as for the red solid curve, but assuming tunneling out of the photo-excited conduction band accumulation layer. Similarly, the blue dashed curve corresponds to a tunnel current, which was derived for the same parameters as for the blue solid curve, but assuming that the surface state cannot be electrically charged. The blue and red solid lines fit well to the experimental data, but require significantly different irradiance levels, given in the table (inset). Note, all the calculated spectra coincide at positive voltages. [P1], © 2015, American Physical Society.

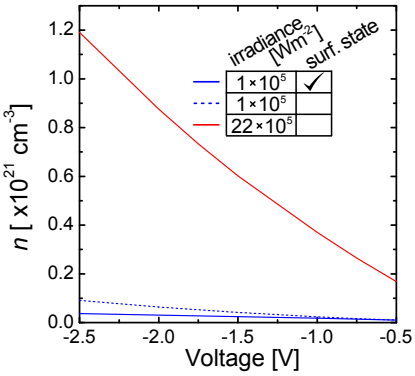

Figure 5.9: Concentration of light-excited bulk electrons at the surface opposite to the tip apex vs. voltage under illumination for a full suppression of the photo-induced tunnel current (red solid line) and a surface-state-limited band bending with photo-induced tunnel current (solid blue line). The blue dashed line illustrates the case of a photo-induced tunnel current, but with no surface state charging. The laser irradiance levels (inset) are identical to those in Fig. 5.8.

Under illumination, the tunnel current was fitted using the irradiance of the laser beam as the only fitting parameter. The tip-sample separation of 0.925 nm determined from the dark spectrum was kept constant, since the pair of dark and illuminated experimental spectra were measured at identical separations. The best fit of the calculated current, assuming full suppression of the photo-induced tunnel current, is shown as solid red curve in Fig. 5.8. Note, the current at positive voltages is independent of the illumination and hence *all* the calculated curves coincide in this voltage range. The result matches the current and the onset voltages of the measured spectrum under illumination on the positive and negative branch.

In order to illustrate the magnitude of the photo-induced tunnel current, if not suppressed, the red dashed line was derived using the same laser irradiance as for the red solid curve, but assuming now that the photo-induced electrons can tunnel. The resulting total current is dominated by the photo-induced tunnel current and is more than one order of magnitude larger than the measured one. Note, the onset voltage for the negative branch is moved to a small positive voltage of 0.3 V. Electrons tunneling out of the sample already at positive voltages have been indeed experimentally observed previously for large laser irradiance.[99, 100]

The blue solid curve in Fig. 5.8 shows the best fit of the calculated current employing surface state-limited band bending including a photo-induced tunnel current

(tunneling of light-excited electrons accumulated at the surface). It agrees also well with the measured spectrum, but the best fit is obtained for a significantly lower laser irradiance as compared to the red curve (see discussion below).

If one assumes that the surface state cannot be occupied by electrons, the lack of surface charges screening the electric field is compensated by the accumulation of additional light-excited electrons at the surface, as shown by the blue dashed line relative to the blue solid line in Fig. 5.9. This leads to a slightly higher photo-induced tunnel current at large voltages, but similarly well fitting at small voltages. The reduction of the current by surface state limited band bending is hence already detectable at the present small laser irradiance, but its effect is much more pronounced at larger laser irradiances.

5.4.5 Comparison and discussion of the models

The dashed blue, solid blue and red lines in Fig. 5.8 demonstrate that all models describe the slope, shape, and onset voltages of the measured spectrum under illumination on the positive and negative branch well. Hence, from this point of view it is almost impossible to decide, which model is physically more appropriate. However, one can discriminate physically these different models. First, the assumption that the surface state cannot be charged when dragged below the Fermi energy at negative sample voltages, is not supported by any experimental or theoretical evidence thus far. Hence, the assumption of a photo-induced tunnel current without surface state limited band bending has to be discarded. For a further discussion of the two remaining models, one has to focus on the electron concentration at the surface (Fig. 5.9) for the two best fits shown as blue and red solid lines in Fig. 5.8. Figure 5.9 shows that the surface-state-limited band bending model exhibits more than one order of magnitude fewer carriers at the surface (blue solid line), than the model of a full suppression of photo-induced tunnel current (red solid line). A smaller amount of light-excited electrons at the surface originates from less laser irradiance: The best-fitting irradiance is found to be smaller for the surface state limited band bending model $[\left(1^{+0.7}_{-0.3}\right) \times 10^5\,\mathrm{Wm^{-2}}]$ as compared to $(22\pm5)\times10^5\,\mathrm{Wm^{-2}}$ for the full suppression model of the photo-induced tunnel current.

The experimentally used laser irradiance (given in Chap. 4.4) is $(1.45\pm0.44)\times10^5\,\mathrm{Wm^{-2}}$. This value agrees well only with the irradiance obtained using the surface-state-limited band bending model including the photo-induced tunnel current. Experimentally the laser irradiance required for the other model was not reached, and hence it can be discarded.

5.5 Conclusions

The quantitative description of photo-excited scanning tunneling spectroscopy, developed in Chap. 3, is applied to experimental data measured on a *p*-doped GaAs(110) surface. The potential and charge carrier distributions within the photo-excited tip-vacuum-semiconductor system is described by the Poisson as well as the hole and electron continuity equations, which are solved by a finite difference algorithm. On the basis of the calculated potential and charge carrier distributions the different contributions to the tunnel current are calculated. Due to the presence of non-equilibrium charge carriers, the calculation of the tunnel current requires an extension of the tunnel current model of Feenstra and Stroscio, in order to include the quasi Fermi levels of the light-excited carrier concentrations. For the GaAs(110) surface, the calculated tunnel currents for different physical models with and without illumination are fitted to the experimental data. The best fit is obtained for a tip-induced band bending, which is limited by the partial occupation of the C_3 surface state in the conduction band with light-excited electrons. The tunnel current at negative voltages is then composed of a valence band contribution and a photo-induced tunnel current of excited electrons in the conduction band. At positive voltages the tunneling of electrons into the conduction band dominates.

How can the quantitative description developed here be applied? Excited charge carriers are particularly relevant in solar cell structures and in light emitting devices, where the spatial distribution of charge carriers, e.g., at defects and interfaces, is critically affecting the efficiency. In order to measure local charge carrier distributions quantitatively with (preferably) atomic resolution by STM, one needs to correlate the tunnel current with the excited charge carrier concentrations. The quantitative description developed here closes this gap, by putting the interpretation of photo-excited (as well as non-excited) tunneling spectra of many different systems on a solid quantitative foundation. By fitting the calculated tunnel current to tunneling spectra with light-excited carriers using as reference spectrum the simultaneously measured dark spectrum, one obtains the best fit value of the laser irradiance, which is directly connected to the charge carrier concentration. Thereby, one can extract from the pairs of dark and illuminated tunneling spectra the locally present excited charge carrier concentration. By doing this spatially resolved one may ultimately derive maps of the local excited charge carrier concentration. Hence, the quantitative description developed here promises to reach significantly deeper physical insight in the physical processes and behavior of excited charge carriers in semi-conducting materials.

Chapter 6

Polarity dependent pinning of a surface state

This chapter is adapted from [P2] (see list of own publications, p. 119),

6.1 Introduction

Chargeable electronic states at semiconductor interfaces, with energies inside the fundamental band gap, commonly induce a phenomenon known as Fermi level pinning.[121] These states can either arise from the interface bonding structure of the semiconductor with, e.g., a metal (so-called metal-induced gap states),[122] or originate from the broken periodicity and the resulting dangling bonds at a semiconductor-vacuum surface.[123] At high densities these surface states may accommodate large quantities of surface charges, which effectively shield the underlying semiconductor from electric potentials applied at the surface (e.g, by metal contacts). The screening shifts the semiconductor's bands and aligns the Fermi level with the energy of the surface states (so-called Fermi level pinning). This effect influences the charge transport across the surface or interface and thus the Fermi level pinning phenomenon is of critical importance for semiconductor-based devices and nanostructures.[124]

It is commonly understood that at sufficiently high densities of surface states in the order of $\approx 6 \times 10^{14}\mathrm{cm}^{-2}$ (corresponding to intrinsic surface states), the Fermi level pinning is essentially independent of the doping as well as of the polarity of externally applied electric fields. This *equilibrium* model assumes a free charge transfer between bands and surface states. In this chapter it will be illustrated that surfaces with chargeable surface states within the fundamental band gap can exhibit

a polarity dependent pinning, since the rate of electron transfer between the bands and surface states is too small due to quantum mechanically prohibited optical transitions. This leads to a one sided, polarity dependent Fermi level pinning, which by itself can create a rectifying behavior.

In order to demonstrate this effect, the semiconductor-vacuum-metal tip configuration in a scanning tunneling microscope is used as model system. Scanning tunneling microscopy together with spectroscopy is one of few experimental methods to probe empty and filled surface states in a single experiment.[62, 125] The tunnel current is highly sensitive to the band edge positions, providing a direct access to the surface potential and hence to the Fermi level pinning.[53, 112, 126] Furthermore, the metallic tip of the STM can be used to apply electric fields, in order to probe the Fermi level pinning as a function of the magnitude and polarity of the applied field.

As semiconductor the clean GaN($10\bar{1}0$) surface is investigated, since most tetrahedrally coordinated non-polar compound semiconductor surfaces can be expected to behave similarly. Non-polar compound semiconductor cleavage surfaces typically have one occupied anion-derived and one empty cation-derived dangling-bond surface state. If these surface states are shifted energetically into the bulk bands, as e.g., for GaAs(110),[127] the tunneling spectroscopy seems to be rather well understood.[13, 15, 66, 125] In contrast, for GaN($10\bar{1}0$) the energetic position of the empty surface state was controversially debated,[128] since the initial STS experiments[129, 130] and calculations[131, 130] found no surface state within the fundamental band gap. However, recent calculations[28, 29, 30, 31] as well as STS experiments at very small tip-sample separations revealed a *"hidden"*, intrinsic empty surface state within the fundamental band gap, which has a very small spatial extension into the vacuum.[132] Hence, GaN($10\bar{1}0$) is used as an example of the group of compound semiconductors, whose non-polar cleavage surfaces have an intrinsic surface state in the fundamental band gap.

6.2 Experimental results

The investigated region of the freshly cleaved GaN($10\bar{1}0$) surface consisted of large atomically flat terraces (see examples in Fig. 6.1 and inset of Fig. 6.2), separated by steps. The steps were found to arise typically from dislocations or stacking faults.[26, 133] STM images reveal that the GaN($10\bar{1}0$) cleavage surfaces used for the experiments have a low defect concentration. Thus, *no* relevant concentrations

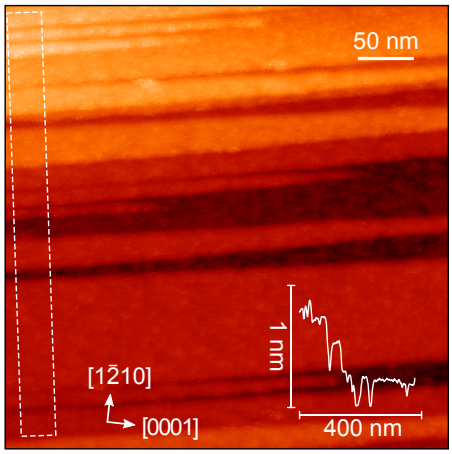

Figure 6.1: STM image of the occupied states of the non-polar GaN(10$\bar{1}$0) cleave surface (m-plane), that was also used for STS experiments. The image was aquired with a constant current of 5 pA and a sample voltage of -4.0 V. It consisted of partially very large atomically flat terraces separated by steps. The averaged height profile, shown at the lower right cover of the image was measured at the region indicated by a dashed rectangle and serves as height scale for the image.

of *extrinsic* surface states and hence no *extrinsic* pinning can be expected. However, the surface should be *intrinsically* pinned due to the empty surface state in the fundamental band gap.[132]

The tunneling spectrum in Fig. 6.2, shown as black squares, exhibits a tunnel current branch at positive and negative voltages and a region in between with no detectable tunnel current (noise level ≈2 pA). The current onset voltages are about +1 V and −1.5 V, respectively. In this experiment, the voltage range without tunnel current ($\times e$) is significantly smaller than the bulk band gap of ≈3.4 eV. Furthermore, the onset voltage of +1 V is significantly larger than that of other n-type non-polar compound semiconductor surfaces, for which values down to almost 0 V are typical.[15, 134] Note, the same features, i.e., onset voltages and apparent band gap, are found in tunneling spectra measured on HVPE grown GaN(10$\bar{1}$0) cleavage surfaces as well as in published spectra in the literature.[130, 132] Hence, the shown spectrum is representative and well reproducible.

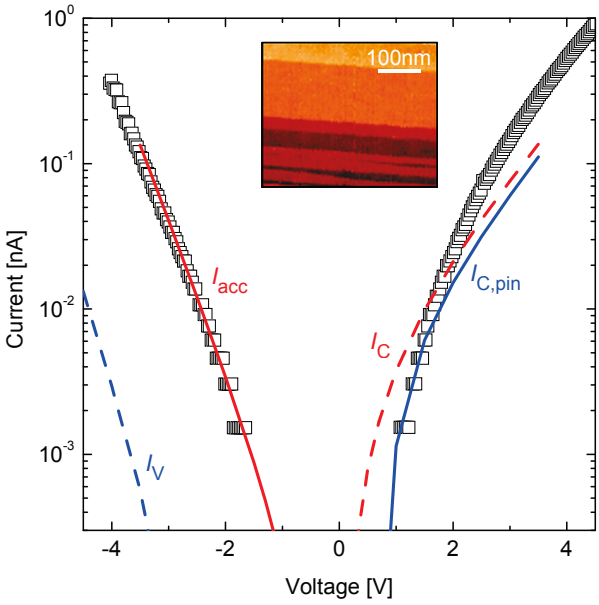

Figure 6.2: Scanning tunneling spectroscopy of n-type GaN$(10\bar{1}0)$ at 290 K. The squares show the experimental data measured at a tip-sample separation fixed by a set voltage of -3.6 V and a set current of 150 pA. The lines represent calculations of the tunnel current with no intrinsic surface state in the band gap (red solid and dashed lines) and with an empty surface state at $E_C - 0.7$ eV (blue solid and dashed lines), pinning the Fermi energy, respectively. Inset: STM image of the GaN$(10\bar{1}0)$ surface, on which the spectrum was measured. [P2], © 2015, American Physical Society.

6.3 Qualitative description

In order to evaluate the measured tunneling spectra, a short qualitative discussion will be given before continuing with a detailed numerical simulation. First, if a surface is fully *pinned* due to the presence of an intrinsic surface state in the band gap, the voltage range without current ($\times e$) corresponds exactly to the fundamental band gap.[110] This is visibly not observed here. Hence, the surface cannot be considered to be fully pinned. In contrast, for an *unpinned* surface, the electric field between the tip and the semiconductor sample induces a band bending in the semiconductor. At negative voltages, the downward band bending shifts the conduction band edge E_C below the Fermi energy E_F and thereby induces an electron accumu-

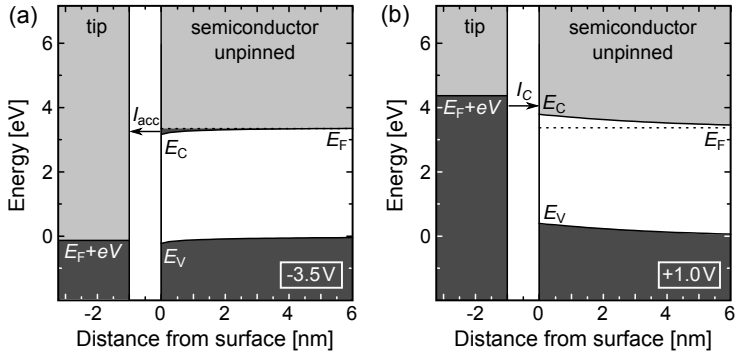

Figure 6.3: Calculated valence (E_V) and conduction (E_C) band edge positions for unpinned GaN surfaces with no surface states in the band gap for (a) negative (-3.5 V) and (b) positive ($+1.0$ V) voltages applied to the semiconductor sample (right-hand side at positive distance values). The sample is located on the right side at positive distance values. The Fermi energy E_F is close to the conduction band in the bulk. The tip with its Fermi energy at $E_F + eV$ is shown on the left-hand side. The dark shaded (light shaded) areas represent filled (empty) states. The band gap and the vacuum gap (tunnel barrier) between the surface at zero position (0 nm) and the tip position (at -1.06 nm) are shown in white. At negative voltages (a) the downward band bending induces an accumulation of electrons in the conduction band. These accumulated electrons tunnel into the tip resulting in an accumulation current I_{acc}. At positive voltages (b) the electrons tunnel from the tip into the conduction band states (I_C). [P2], © 2015, American Physical Society.

lation in the conduction band (Fig. 6.3(a)). The accumulated electrons can already tunnel at voltages within the band gap (accumulation current I_{acc}) and hence the voltage range without tunnel current is reduced.[66, 133, 134] Thus, at first view the tunneling spectrum can be explained apparently assuming an unpinned GaN surface despite the presence of an intrinsic surface state in the band gap.

However, this conclusion is in conflict with the current onset at positive voltages: For unpinned n-type surfaces of all other previously investigated compound semiconductor materials, the onset of the tunnel current at positive voltages is always found close to 0 V.[76, 15, 134] This should also be the case for unpinned GaN surfaces (as calculated below). This is well below the value of $+0.8$ to $+1$ V observed here and visible in published tunneling spectra of n-type GaN($10\bar{1}0$) surfaces.[129, 132, 130]

Thus, neither the model of an *unpinned* nor of a *pinned* surface can satisfactorily explain the experimental data.

6.4 Simulation of the tunnel current of the GaN$(10\bar{1}0)$ surface

To resolve this puzzling situation the simulations of the tunnel current will be discussed, in order to evaluate the measured tunneling spectrum quantitatively. The simulations of the tunnel current assume two different physical models: an *unpinned* and a *fully pinned* GaN surface. One may think of calculating in addition a weakly pinned surface, but this is not necessary since on the one hand the concentration of the intrinsic surface state of 6×10^{14} cm^{-2} is high enough to induce a full pinning[121, 106] and on the other hand, the extrinsic defect concentration is too low to be relevant.

Again, the three-dimensional finite difference calculation of the electrostatic potential in a tip-vacuum-semiconductor sample system, as developed in Chap. 3, is used here. Note, if one uses the code of Feenstra solving the Poisson equation only,[70] one obtains the same physical conclusions. Here it was chosen to include the continuity equations, since this is a more elaborate physical model, especially suited to calculate the accumulation current. For the fully pinned surface, the intrinsic empty surface state is modeled as a Gaussian distribution 0.7 eV below the conduction band edge (FWHM=0.1 eV) and with a concentration of 6×10^{14} cm^{-2} following band structure calculations.[132] In this case the charge neutrality level at the surface E_{CNL} is chosen to be between the filled and empty intrinsic surface states.[123] The tunnel current is calculated using the potential distribution following Ref. [66]. The resulting tunnel currents are shown in Fig. 6.2 as solid and dashed lines. The corresponding band edge positions as a function of the distance into the sample through the central axis of the tip are shown in Figs. 6.3 and 6.4 for the unpinned and pinned surfaces, respectively.

6.4.1 Simulation of the unpinned surface without surface states

First, the focus is set to the *unpinned* surface without surface states (red solid and dashed lines in Fig. 6.2):

(i) At negative voltages, the accumulation current I_{acc}, consisting of electrons extracted from the electron accumulation zone in the conduction band (Fig. 6.3(a)), fits well to the experimental data for a tip-sample separation z of 1.06 nm (compare the red solid line with symbols in Fig. 6.2). z is the only fitting parameter used and is kept constant for all further calculations. Note, a slightly larger z in the experiment was used to avoid tip-sample interactions and obtain more stable tunneling conditions.

(ii) At positive voltages, the tunnel current arises from tunneling of electrons into the empty conduction band states (Fig. 6.3(b)). The onset voltage of this calculated current is found close to +0.2 V (I_{C}, red dashed line in Fig. 6.2). This does not describe the large experimentally observed onset voltage of about +1.0 V. In addition, the slope of the experimental data is not reproduced and at small voltages the calculated current is too large. Thus, the physical model of an unpinned surface only describes the spectrum at negative voltages properly.

6.4.2 Simulation of the fully pinned surface

Second, the *fully pinned* surface with an intrinsic surface state in the band gap, as depicted in Fig. 6.4(a), is addressed: For this pinned surface the effect of the proximity of the tip and an additional applied voltage is discussed.

(i) At positive voltages, the calculated current arises from electrons tunneling into the empty conduction band states ($I_{\mathrm{C,pin}}$, solid blue line in Fig. 6.2). The best fit yields an onset voltage now shifted to +0.81 V, in good agreement with the experimental onset voltage of about +1 V. In addition, the slope of the calculated current fits well to the experimental data. The shifted onset voltage and the larger slope arise from the band bending being increased by ΔE as compared to the case without pinning (compare the band edge positions shown as dashed and solid lines in Fig. 6.4(c)). With increasing positive voltage, the calculated tunnel current with (pinned, $I_{\mathrm{C,pin}}$) and without (unpinned, I_{C}) intrinsic surface state increasingly merge. This effect is due to the change in electron occupation of the surface state with band bending: At *large* positive voltages, the surface state is energetically located fully above the Fermi energy and hence completely empty. Therefore, there is effectively no pinning of the Fermi level. In contrast, at *small* positive voltages, the tail of the surface state below the Fermi energy is occupied and the Fermi level is pinned.

(ii) At negative voltages, the pinning-induced upward band bending suppresses an electron accumulation in the conduction band (Fig. 6.4(b)). Hence, only electrons

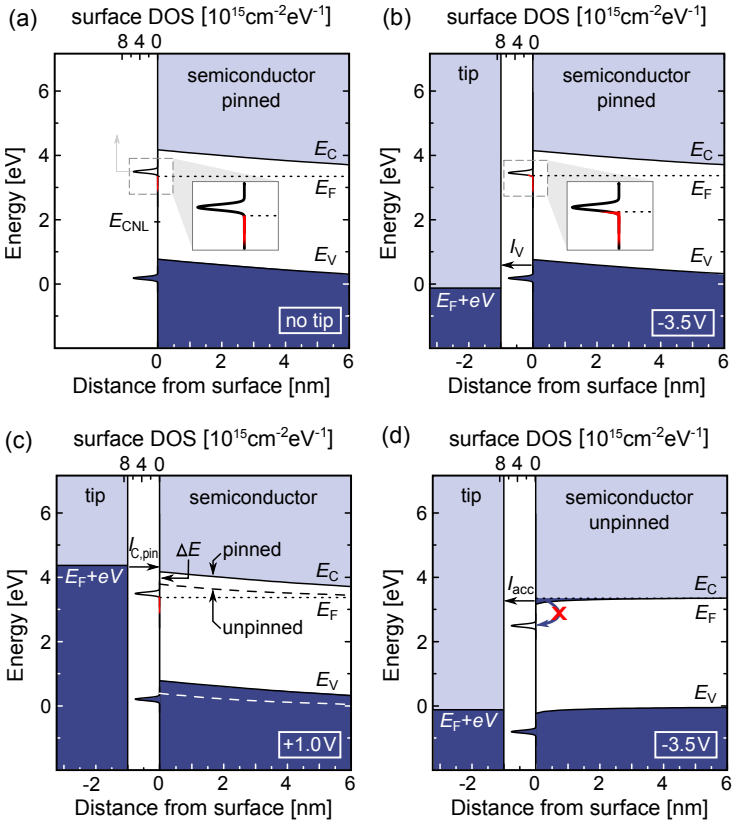

Figure 6.4: Calculated valence (E_V) and conduction (E_C) band edge positions for a GaN surface with a filled and an empty intrinsic surface state. Their density of states is modeled as Gaussian distributions and given on the top axis. Following band structure calculations[132] the upper (empty) intrinsic surface state is assumed to be 0.7 eV below the conduction band minimum, whereas the lower one is below the valence band edge. The same labeling conventions as in Fig. 6.3 are used. Four different configurations are shown: (a) Surface without tip and no applied voltage in equilibrium. The intrinsic surface state is partially occupied (see tiny red area in enlarged inset), fully pinning the surface and hence inducing an upward band bending. (b) Surface in the presence of the metallic tip with a negative sample voltage of -3.5 V. The system reaches equilibrium by partially occupying the surface state (see inset). This induces an upward band bending and fully pins the Fermi level. Hence, no electron accumulation in the conduction band exists and only electrons from the valence band tunnel (I_V). *(continued on the next page)*

Figure 6.4: *(continuation)* (c) Surface biased at +1.0 V with the tip present. The system is again in equilibrium by partially filling the surface state and thus pinning the Fermi level. The band edge positions are presented by solid lines. For comparison, the band edge positions without surface state taken from Fig. 6.3b are shown as dashed lines. The bands are shifted by ΔE, resulting in an offset of the onset voltage of the conduction band tunnel current I_C as experimentally observed. (d) Non equilibrium case of the tip-vacuum-semiconductor system with the semiconductor surface biased at -3.5 V. Under tunneling conditions the surface state does not reach its equilibrium filling, since the optical electron transition between the conduction band and the surface state is prohibited. Hence, there is no Fermi level pinning. This situation is observed experimentally. [P2],

from the valence band can tunnel into the tip. This valence band current I_V is too small (blue dashed line in Fig. 6.2).

Tunneling in or out of the intrinsic Ga-derived surface state in the band gap can be neglected, since its density of states is much smaller than that of the conduction band edge, and indeed, experimentally, the surface state could only be detected at extremely small tip-sample separations.[132] Therefore one does not consider tunneling in/out of the intrinsic surface state here.

6.5 Discussion

At this stage it will be discussed, which of the models describes the system properly. The best fit is obtained for an *unpinned* surface at *negative* voltages (red solid line in Fig. 6.2), but a *pinned* surface at *positive* voltages (blue solid line). This result indicates the existence of a voltage dependent intrinsic pinning. What is the physical origin of this astonishing situation?

Due to the presence of an intrinsic surface state in the band gap, the central question is, why the surface state does not affect the electrostatic potential distribution at negative voltages. It should be recalled that a completely empty surface state (neutral surface) does not influence the Fermi level. Hence, the above suggested lack of Fermi level pinning at negative voltages indicates that the surface state remains unoccupied, although it is shifted by band bending below the Fermi energy. *In equilibrium* the surface state would be filled at negative voltages (effect of pinning shown schematically in Fig. 6.4(b)). However, under tunneling conditions the situation is different and the system is not in equilibrium anymore: For

n-type material, the electrons filling the surface state can only originate from the conduction band. If the rate of electron transfer from the conduction band into the surface state (charging process) is smaller than that of electrons tunneling out of the surface state (discharging process), the surface state cannot reach its equilibrium filling and does not (or only partially) pin. Hence, the transfer probabilities between the conduction band minimum and the surface state are estimated on basis of the quantum mechanical selection rules: For optical transitions of electrons from the conduction band into the surface state the selection rules require that the orbital angular momentum changes by ± 1.[135] However, both the conduction band minimum and the surface state have the same s-type orbital character[31, 132][136, p.34] and hence direct optical transitions between them are prohibited. Only inelastic transitions may occur, whose probabilities are, however, much smaller due to need of an additional particle (e.g. phonon).[137] In this situation the surface state is emptied by the tunnel process more rapidly than it is refilled from the conduction band. As a result, the surface state cannot reach its equilibrium filling under tunneling conditions at negative voltages and can hence not cause any pinning effect. The resulting band diagram is shown in Fig. 6.4(d).

In contrast, at positive voltages no electrons are extracted from the surface (only electron injection occurs) and hence even for small transition rates between the conduction band and the intrinsic surface state in the band gap, the surface state can reach its equilibrium filling, resulting in the band diagram in Fig. 6.4(c).

6.6 Conclusions

In conclusion, the surface state in the band gap of GaN($10\bar{1}0$) surfaces pins the Fermi level only at small positive voltages, but not at negative voltages. This polarity dependence of the Fermi level pinning arises from the low transition rate of electrons from the conduction band to the surface state, inhibiting the filling of the surface state when shifted below the Fermi energy by band bending. Thus, even if an intrinsic surface state is present within the fundamental band gap, it may not pin the Fermi level or only at one polarity. This Chapter shows that one needs to consider the electron transition rates from and to the surface state and therewith the quantum numbers of the involved states to determine the pinning potential of intrinsic surface states in the band gap. Similar effects may occur at interfaces of electronic devices, e.g., interface misfit dislocation arrays in heteroepitaxy, interfaces with oxide semiconductors, between Si and nitride semiconductors, and at the footprint of heteroepitaxially grown semiconductor nanowires, as well

as at semiconductor nanowire sidewall facets. In all cases the pinning potential of interface states in the band gap has a crucial influence on the device properties.

Chapter 7

Intrinsic electronic properties of high-quality InN

7.1 Introduction

In recent years a hype developed around indium nitride (InN) due to measurements and calculations suggesting highly intriguing electronic properties, such as the existence of an electron accumulation in the bulk conduction band,[39, 40, 41, 42, 43, 44] an extremely large electron affinity,[33, 138] or the supposed impossibility of obtaining p-type doped surfaces.[139] Even superconductivity was reported.[140, 141, 142, 142] From these measurements and calculations InN appears to be a highly unusual semiconductor, differing fundamentally from all other binary compound semiconductors.

Unfortunately, to date macroscopic InN single crystal bulk material is not available. Hence, experiments can only be performed either on heteroepitaxially grown layers [33, 40, 140, 143, 144, 145] or on nanostructures.[42, 138] However, heteroepitaxially grown layers typically contain a high density of defects, while nanostructures show interface and/or surface effects, both leading to a rather complex data interpretation. Regrettably, up to now, all experimental measurements were performed on such samples. In order to review the *intrinsic* electronic properties of InN, experiments need to be performed on high quality material with low defect density and strain, having almost bulk-like electronic properties.

In this chapter the electronic properties of high-quality thick heteroepitaxial InN layers, grown on GaN(0001) are probed. The high material quality is proven by high-resolution transmission electron microscopy (HR-TEM). The electronic properties are determined using cross-sectional scanning tunneling microscopy and spectroscopy. It is demonstrated that at the (non-polar) m-plane cleavage surface no

intrinsic surface states are present in the fundamental band gap. The Fermi level is located within the fundamental bulk band gap. Hence, there is no intrinsic electron accumulation and therewith no fundamental hindering for p-type doping. High quality InN appears to be as conventional as all the other binary III-V semiconductors.

7.2 Experimental results

7.2.1 Structural analysis of the GaN-InN interface

First the quality of the InN layers is discussed, followed by the determination of the electronic properties.

Figure 7.1 illustrates the cross-sectional scanning tunneling and transmission electron microscopy results. The cross-sectional cleavage surface of the GaN substrate is mostly atomically flat with only few steps. In the area imaged by STM in Fig. 7.1(a) the GaN pseudosubstrate exhibits perfect cleavage without steps. In contrast, at the GaN-InN interface, a high density of surface steps form and extend in c-direction deep into the InN layer. The line profile in Fig. 7.1(b) (left frame) demonstrates that these steps have a height of one mono-layer (ML). The width of the elongated terraces is typically between 2 and 5 nm directly at the interface. Large scan cross-sectional STM images show that with increasing distance from the interface some of the steps annihilate, leading to 40-50 nm wide terraces.

The appearance of steps at the interface indicates the presence of interface dislocations intersecting the m-plane cleavage surface.[133] The step height implies that the Burgers vectors of the interface dislocations have a component of one ML in m-direction, i.e., $\pm a/2\left[10\bar{1}0\right]$. The annihilation of such steps demonstrates that dislocations with opposite Burgers vectors are present. In order to determine the in-plane component of the Burgers vector, cross-sectional TEM images of the interface region were measured: Figure 7.1(c) indicates a more or less regular pattern of dislocations at the GaN-InN interface. In the imaged sections, the individual dislocations have a separation of typically about 2 nm. The interface dislocations are shown at higher magnification in the atomic resolution aberration corrected high-resolution TEM image in Fig. 7.1(d). Each atomic contrast arises from one Ga (or In) column in $\left[10\bar{1}0\right]$ direction, as illustrated in Fig. 7.2(b) and (c). The N atoms are almost invisible in the HR-TEM images, due to their lower scattering cross section as compared to In and Ga.[146, 147] The unit cell of the m-plane is

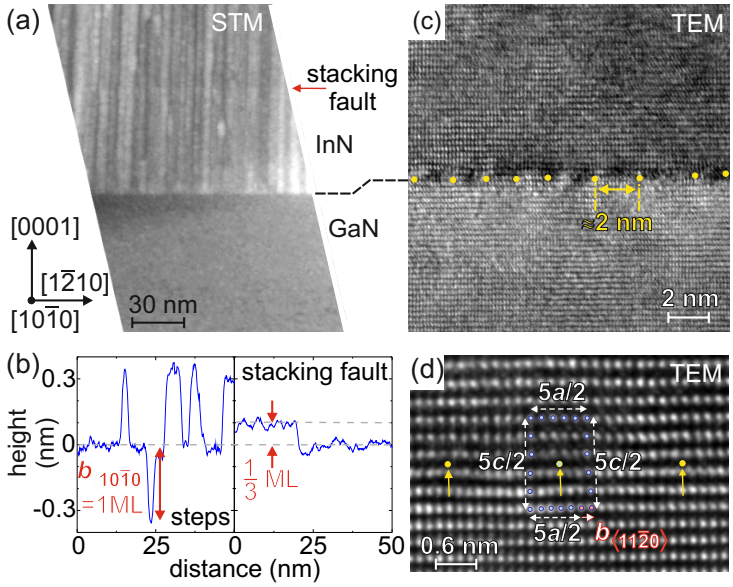

Figure 7.1: Cross-sectional scanning tunneling and transmission electron microscopy of the InN layer on GaN. (a) Constant-current STM image of the InN (top)/GaN (bottom) interface region measured at +4.5 V bias voltage and 40 pA tunnel current. A high density of steps oriented in [0001] direction is present on the InN (10$\bar{1}$0) cleavage surface. Each step starts at the interface, demonstrating the presence of interface dislocations with out-of-plane burgers vector components $b_\perp = \pm\frac{a}{2}\left[10\bar{1}0\right]$ as illustrated in the left part of frame (b). (c) Transmission electron microscopy (TEM) image in m ([10$\bar{1}$0]) direction providing an overview of the InN/GaN interface. At the interface a dislocation network (cores marked with yellow points) can be detected. (d) Atomic resolution aberration corrected high-resolution TEM image showing the interface dislocations at higher magnification. The Burgers circuit yields the in plane component of the Burgers vector to be $b_\parallel = \frac{a}{6}\left[11\bar{2}0\right]$. The interface dislocations are hence edge dislocations with a Burgers vector of the type $\vec{b}=\frac{a}{3}\langle 11\bar{2}0\rangle$. In few cases stacking faults in the InN layer were observed as indicated by the arrow in (a). The stacking faults induce a height shift of $\frac{1}{3}$ ML [right part of frame (b)].

marked by the red dashed rectangle in Fig. 7.2(c). However, since it is not possible to distinguish between In (or Ga) atoms positioned at different sites along the atomic columns in the HR-TEM image, all In (or Ga) columns exhibit the same contrast. Hence, the unit cell, seemingly visible in the TEM images and indicated by the red solid rectangle in Fig. 7.2(c), has the length and width of $a/2$ and $c/2$, respectively. Hence, the separation between neighboring contrast maxima of the HR-TEM images correspond to $\frac{a}{2}$ and $\frac{c}{2}$, with a and c being the lattice constants in $\left[1\bar{2}10\right]$ and [0001] direction, respectively. The in-plane component of the Burgers vector, illustrated using the Burgers circuit in Fig. 7.1(d), is found to be $\frac{a}{6}\left[1\bar{2}10\right]$. Hence, the dislocation network at the interface is composed of pure edge dislocations with Burgers vectors of the type $\frac{a}{3}\left\langle 11\bar{2}0\right\rangle$. The average dislocation separation observed in TEM images matches well the average step separation in STM images of 2 to 5 nm directly at the interface. These values are consistent with an interface dislocation network for the 10,8% lattice mismatch of InN on GaN(0001). Note, due to symmetry reasons one should expect each equivalent Burgers vector orientation to occur on average with equal frequency. However, in the non-atomically resolved STM image only the dislocations whose Burgers vector have an out-of-plane component (4 out of the 6 possible a-type Burgers vectors) can be detected. The remaining two require in-plane atomic resolution.

Besides the interface dislocation network, only very few dislocations within the InN layer are observed. For example, sometimes stacking faults on the c-plane were found, giving rise to a step of $\frac{1}{3}$ ML oriented in a-direction on the cleavage plane. The arrow in Fig. 7.1(a) marks such a stacking fault and the height profile in Fig. 7.1(b) (right frame) illustrates the height offset of $\frac{1}{3}$ ML. This suggest that most of the strain is relaxed directly at the interface. Hence, one can expect that the InN layer further away from the interface is essentially strain free and of high quality compared to the material investigated previously to determine the intriguing properties of bulk InN.

7.2.2 Electrical analysis of the GaN-InN interface

After demonstrating the high quality of the InN layers, the focus is set to their electronic properties. Figure 7.3(a) shows scanning tunneling spectra measured on the cross-sectional m-plane cleavage surface of the GaN substrate (red curve) and the InN layer (blue curve). The spectra were acquired with a PtIr tip at constant tip-sample separation, which was fixed by a set current of 35 pA and set voltages of +2.5 V and +1.0 V for GaN and InN, respectively. Taking into account the different band gaps, these set voltages lead to roughly equal tip-sample separations

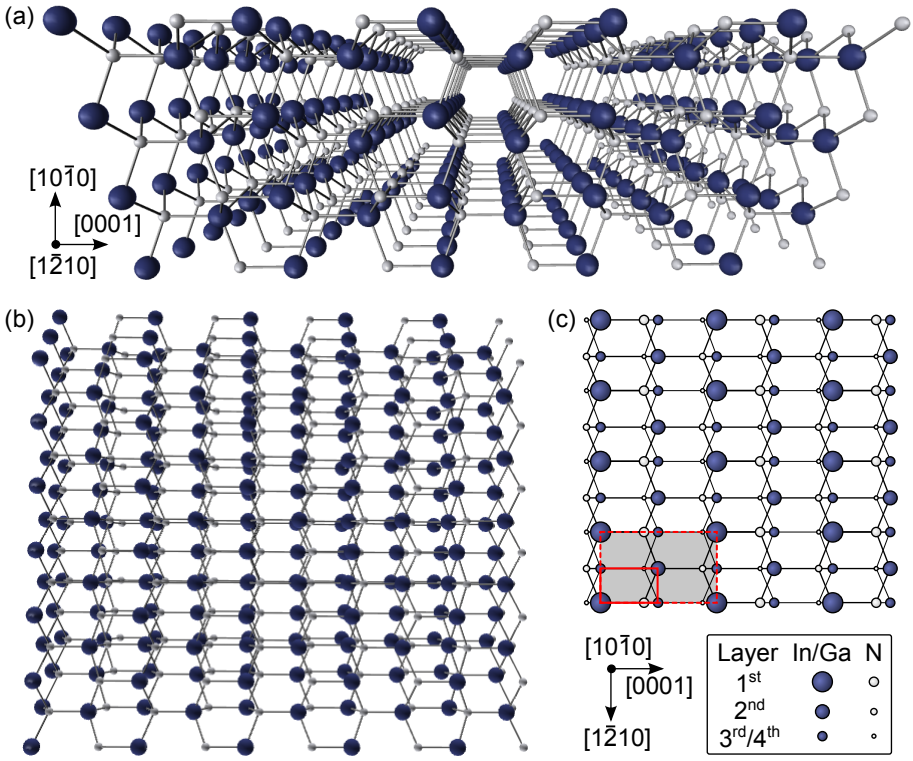

Figure 7.2: (a) Atomic lattice of InN (or GaN) in [1$\bar{2}$10] direction. Blue spheres correspond to In/Ga atoms, while N atoms are indicated as gray spheres. The diameter of the blue spheres is approximately twice the diameter of the gray spheres, visualizing the ratio of the covalent radii of In and N. (b) Atomic lattice of InN (or GaN) in [10$\bar{1}$0] direction, i.e. top-view of the (non-relaxed) *m*-plane. (c) Isometric top-view of of the InN (or GaN) *m*-plane. The diameter of the spheres decreases with increasing distance of the atomic layers from the top layer. In analogy to (a) and (b), the spheres representing N atoms exhibit smaller diameters than the In (or Ga) atoms of the same atomic layer due to their different covalent radii. Note, the columns consist of either only N or Ga/In atoms due to the cross sectional view on the polar [0001] planes. These columns are observed in HR-TEM images (cf. Fig. 7.1(d)). The N atoms are almost invisible in the HR-TEM images, due to their lower scattering cross section as compared to In and Ga.[146, 147] The unit cell of the *m*-plane is marked by the red dashed rectangle. However, since it is not possible to distinguish between In (or Ga) atoms positioned at different sites along the atomic columns in the HR-TEM image, all In (or Ga) columns exhibit the same contrast. Hence, the unit cell, seemingly visible in the TEM images and indicated by the red solid rectangle in (c), has the length and width of $a/2$ and $c/2$, respectively.

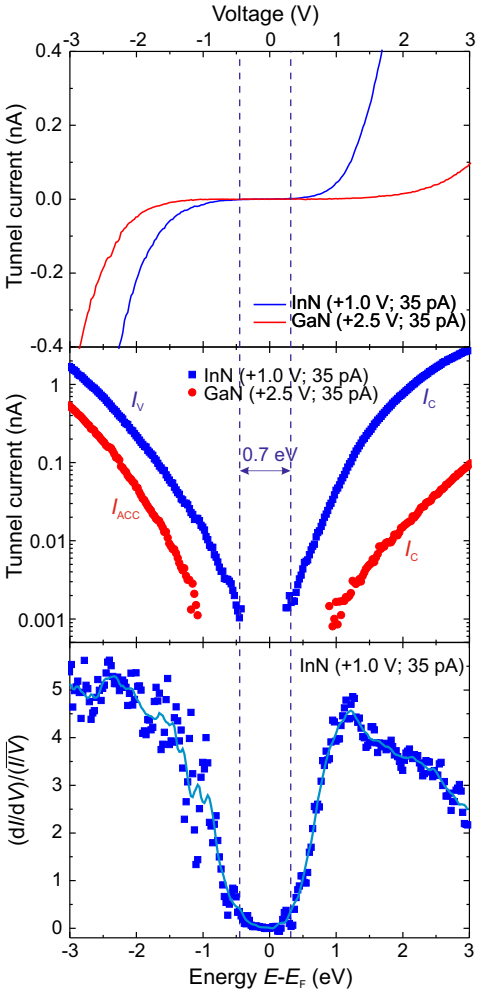

Figure 7.3: STS of the InN and GaN $(10\bar{1}0)$ surfaces illustrated in a linear (a) and logarithmic (b) scale. The data shown in blue (red) has been measured on the InN (GaN) cleavage surface. Note, the InN surface is pinned by the presence of a high step density (see Fig. 7.1(a)) suppressing the tip-induced band bending. Hence, the positive and negative branches of the tunnel current correspond directly to the tunneling of electrons into the conduction band and out of the valence band, respectively, separated by the band gap of 0.7 eV. No intrinsic surface states within the fundamental band gap are detected and the Fermi energy is 0.3 eV below the conduction band edge, i.e. within the fundamental band gap. In contrast, the GaN surface is free of steps and hence the tunneling spectrum is affected by the tip-induced band bending. This induces a tunnel current of electrons out of a tip-induced accumulation zone in the conduction band at negative voltages within the fundamental band gap. At positive voltages electrons tunnel again into the conduction band states. (c) Normalized differential conductivity $(\mathrm{d}I/\mathrm{d}V)/(\overline{I/V})$ derived from the tunnel spectrum measured on the InN cleavage surface.

on both materials. Both spectra exhibit clear semi-conducting properties with no tunnel current at small voltages. The voltage range, where the tunnel current is below the detection limit of 1 pA, can be seen best with a logarithmic current scale in Fig. 7.3(b). It is about 0.7 V (2 V) wide for InN (GaN). The values require a detailed explanation, which is related to the presence or absence of *extrinsic* surface states.

First, the discussion of the tunneling spectra measured on GaN $\left(10\bar{1}0\right)$ surfaces without surface steps (i.e. without *extrinsic* pinning defects) given in Chap. 6 is recalled: These spectra reveal a polarity depended Fermi-level pinning caused by *intrinsic* surface states: At negative sample voltages, no pinning occurs. Hence, the tunnel current is dominated by electrons tunneling out of the tip-induced electron accumulation zone already at voltages corresponding to energies within the band gap. Tunneling out of valence band states occurs only at larger magnitudes of negative voltages and is negligible as compared to the accumulation current I_{acc}.[110] At positive voltages the tunnel current arises from electrons tunneling into empty conduction band states. Due to the pinning of the intrinsic surface state, the onset voltage of the conduction band current is shifted from $\sim 0\,\mathrm{V}$ to $\sim 0.9\,\mathrm{V}$ (cf. Fig. 6.2).

The GaN $\left(10\bar{1}0\right)$ surface investigated in this chapter is also free of surface steps (cf. Fig. 7.1(a)) and hence free of extrinsic pinning defects. Therefore, the tunneling spectra measured on this surface exhibit the same characteristic onset voltages as those analyzed in Chap. 6. Because of the polarity depended Fermi-level pinning, the voltage range of 2 V without detectable tunnel current in Fig. 7.3(b) is smaller than the fundamental band gap of the GaN $\left(10\bar{1}0\right)$ surface.

In contrast, the InN surface has a large density of steps starting at the dislocation network at the GaN/InN interface. Such steps typically have electronic states in the band gap and hence act as extrinsic pinning centers.[148, 149, 18] Therefore, the Fermi energy is pinned at the InN surface and no tip-induced band bending is present. Hence, the voltage scale corresponds directly to the energy scale and the tunnel currents at positive and negative voltages arise from tunneling into the empty conduction and filled valence band states, respectively. The surface band gap is thus $\sim 0.7\,\mathrm{eV}$ in agreement to that determined for bulk InN. In addition, the tunneling spectra show that the Fermi energy is about $\sim 0.3\,\mathrm{eV}$ below conduction band edge within the fundamental band gap. Thus, there is no electron accumulation. Furthermore, the differential conductivity in Fig. 7.3(c) shows no indications of *intrinsic* surface states in the fundamental band gap. The filled and empty surface states are located energetically in the valence and conduction band, respectively. Thus, one is faced with the classical situation of a non-polar III-V

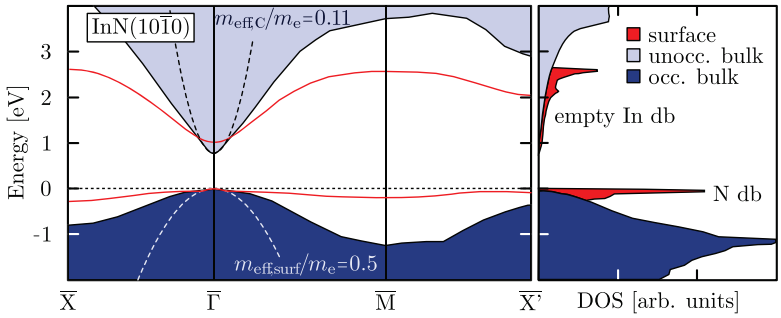

Figure 7.4: Calculated electronic band structure (left) and corresponding density of states (right) of the InN (10$\bar{1}$0) surface. The data is taken from Ref. [29]. For the conduction band minimum, a density-of-states effective mass of $m_{\mathrm{eff,C}}/m_{\mathrm{e}} = 0.11$ was obtained by a fit of the quadratic dispersion relation. In analogy, for the density-of-states effective mass of the occupied surface state, a value of $m_{\mathrm{eff,surf}}/m_{\mathrm{e}} = 0.5$ was determined.

compound semiconductor surface, where the bulk band gap, which is free of intrinsic surface states, is probed. This agrees with theoretical calculations of the band structure of the InN (10$\bar{1}$0) surface[29] (cf. Fig. 7.4).

7.3 Simulation of the tunnel current of the InN(10$\bar{1}$0) surface

To corroborate the interpretation, the tunnel current is calculated using the three-dimensional finite difference calculation of the electrostatic potential and the continuity equations for holes and electrons in a tip-vacuum-semiconductor sample system as developed in Chap. 3. The extrinsic pinning centers at the surface due to steps are modeled as a half filled Gaussian distribution 0.27 eV below the conduction band edge (FWHM= 0.1 eV). Assuming an average step separation of $\sim$ 3 nm (arising from the interface dislocations in the lattice mismatched InN/GaN(0001) system) and one defect state per c-lattice constant along the [0001]-oriented steps, an extrinsic defect state density at the surface of $\sim 5 \times 10^{13}\mathrm{cm}^{-2}$ is obtained, which is used in the calculation. Furthermore, a band gap of 0.67 eV is assumed.[32, 150, 151, 152] Since intrinsic surface states usually extend further into the vacuum than bulk states, the tunnel current is primarily determined by the surface states.[18] This can be assumed to be fulfilled for the occupied surface

state at the N surface atoms: According to Fig. 7.4, its energy is directly at the valence band maximum and the dispersion is flatter than the dispersion of the bulk states (i.e. its density of states is also larger).[29] In contrast, as for GaN $(10\bar{1}0)$ surfaces,[132] the density of states and extension into the vacuum of the empty surface state is smaller than that of the bulk states. In addition the surface state has an energy well within the conduction band.[29] Therefore, electrons first tunnel into the bulk conduction band. Hence, the tunnel current is simulated using the bulk electron effective mass and adjusting the valence band current using a surface hole effective mass $m_{\mathrm{eff,surf}}$.[16] Both effective masses are determined from the band structure calculation shown in Fig. 7.4.

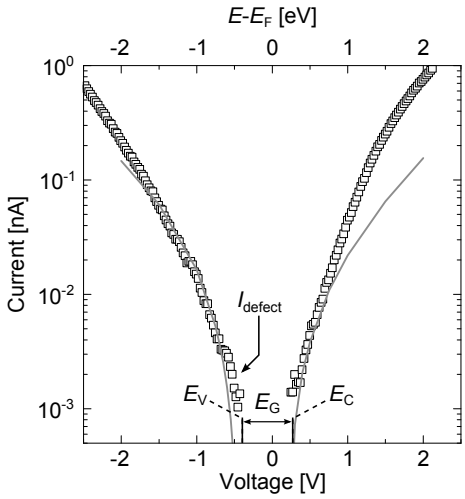

Figure 7.5: Tunnel current obtained for an effective hole and electron mass of 0.5 and 0.11 m_{e}, respectively, shown as solid line together with the experimental data points from Fig. 7.3 (symbols). The band edge positions of $E_{\mathrm{V}} = -0.4$ eV and $E_{\mathrm{C}} = +0.27$ V are indicated by dashes. The band gap used for the calculation is $E_{\mathrm{G}} = 0.67\,\mathrm{eV}$.

7.4 Discussion

The resulting tunnel current obtained for a surface effective hole and bulk effective electron mass of 0.5 and 0.11 m_{e}, respectively, is shown in Fig. 7.5 as solid line together with the experimental data points (symbols). The best result is obtained

for a tip-sample separation of 0.79 nm. The resulting band edge positions of $E_V = -0.4$ eV and $E_C = +0.27$ V are indicated by dashes. The calculated tunnel current agrees well with the initial slopes and onset voltages. At negative voltages the current arises from electrons tunneling from filled surface valence band states into the tip. At positive voltages, electrons tunnel into the empty conduction band states.

The higher current close to the onset at negative voltages can be related to the high extrinsic defect state density: The energy of the defect states is close to the Fermi energy E_F, but due to barrier effects in the tip-vacuum-InN system, they increase the tunnel current within the band gap on the valence band side for n-type materials.[129, 144, 102, 153] This yields the so-called defect current I_{defect}.

The calculation corroborates the interpretation of the tunneling spectra and indicates that no *intrinsic* surface states are present in the fundamental band gap. Furthermore, the band edge positions visible in the experimental and simulated tunnel spectra demonstrate that the Fermi energy is in the fundamental band gap. Hence, there is no *intrinsic* electron accumulation present. There is even no electron accumulation with a positively biased tip in close proximity to the InN surface.

7.5 Conclusions

In conclusion, the structural and electronic properties of high-quality, thick heteroepitaxial InN layers, grown on GaN(0001) are probed by cross-sectional STM and STS as well as cross-sectional HR-TEM on non-polar m-planes. STM images reveal a high density of surface steps, forming at the GaN-InN interface and extending in c-direction deep into the InN layer. The formation of these steps is attributed to a network of edge dislocations at the interface (Burgers vector of the type $\frac{a}{3}\langle 11\bar{2}0\rangle$), which is observed on HR-TEM images. The average step separation of 2-5 nm is consistent with an interface dislocation network for the 10.8% lattice mismatch of InN on GaN(0001). Besides the interface dislocation network, only very few dislocations within the InN layer are observed, emphasizing the high quality of the InN layers.

STS measurements, performed on the non-polar InN $(10\bar{1}0)$ surface, demonstrate that the m-plane surface is free of intrinsic surface states in the fundamental band gap. The Fermi level is located within the fundamental bulk band gap. Due to the Fermi-level pinning, caused by the extrinsic defect states, the region without detectable tunnel current in the I-V spectra is attributed to the fundamental band gap of ~ 0.7 eV. Under these assumptions (incorporation of extrinsic defect states,

but no intrinsic surface states), the measured I-V spectra are compared to simulated spectra (using the model developed in Chap. 3). The agreement between measured and simulated spectra corroborates the result that there is no intrinsic electron accumulation at the non-polar InN($10\bar{1}0$) surface and therewith no fundamental hindering for p-type doping. High quality InN appears to be as conventional as all the other binary III-V semiconductors.

Chapter 8

Summary

The investigation of non-polar III-V semiconductor surfaces by cross-section scanning tunneling microscopy and spectroscopy as well as transmission electron microscopy revealed physical surface effects that could have a major impact on novel electrical devices, such as light-emitting diodes, lasers, solar cells, but also high-electron-mobility transistors. Furthermore, photo-excited scanning tunneling spectroscopy was performed on non-polar GaAs(110) surfaces. With this promising technique, surface photo-voltages and local charge carrier distributions can be probed with atomic resolution.

The general difficulty in a quantitative analysis of scanning tunneling spectroscopy measurements and hence in the determination of physical properties of the semiconductor surface is the *tip-induced band bending*: The electrostatic potential of the tip is not completely screened at the surface of the sample, especially for low-doped materials. Hence, the valence- and conduction band edge of these materials are bent to higher or lower values compared to their values deep within the bulk material. Additionally, one has to take into account the generation and the redistribution of light-excited charge carriers for photo-excited scanning tunneling spectroscopy. Thus, in this thesis, a quantitative description of scanning tunneling spectroscopy with and without light-excited carriers is developed. It is based on a finite difference iteration of the electrostatic potential and the carrier distributions in three dimensions, followed by the calculation of the tunnel current that incorporates light-excited carriers. On the basis of this model, the comparison of measured and calculated scanning tunneling spectra enables the determination of the semiconductor's physical properties.

At first, the model was applied to scanning tunneling spectra measured on *p*-GaAs(110) surfaces with and without laser excitation. It is proven that the model

reproduces the onset voltages and slopes of the measured spectra with high accuracy, revealing the carrier concentrations at the surface of the semiconductor. Furthermore, with the help of the calculated tunneling spectra under illumination, one out of two competing physical descriptions of the suppressed tunneling of electrons from the conduction band of the GaAs(110) surfaces into the tip was discarded: Instead of being completely suppressed, the accumulation current is lowered due to a limited band bending caused by Fermi-level pinning at the intrinsic C_3-surface state.

The application of the simulation model to scanning tunneling spectra measured on non-polar n-GaN($10\bar{1}0$) surfaces helped to demonstrate the existence of a polarity depended Fermi-level pinning. This effect is found to be caused by the low transition rate of electrons from the conduction band to the surface state, inhibiting the filling of the surface state when shifted below the Fermi energy by band bending. Thus, this state pins the Fermi level only at small positive voltages, but not at negative voltages. The results show that an intrinsic surface state may not pin the Fermi level or only at one polarity, even if it is energetically located within the fundamental band gap. For the determination of the pinning potential of intrinsic surface states in the band gap, one rather needs to consider the electron transition rates from and to the surface state and therewith the quantum numbers of the involved states. Interfaces of electronic devices (e.g., interface misfit dislocation arrays in heteroepitaxy, interfaces with oxide semiconductors, between Si and nitride semiconductors, and at the footprint of heteroepitaxially grown semiconductor nanowires, as well as at semiconductor nanowire sidewall facets) may exhibit similar effects, which will crucially affect the device properties.

Furthermore, InN layers, grown on GaN were probed by combining the advantages of cross-sectional scanning tunneling microscopy, cross-sectional scanning tunneling spectroscopy in combination with the simulation model, as well as transmission electron microscopy. The lattice mismatch of GaN and InN was found to be confined directly at the GaN/InN interface by introducing a dislocation network. It is composed of pure edge dislocations with Burgers vectors of the type $\frac{a}{3}\langle 11\bar{2}0\rangle$. As a result, the overgrown InN layer is of highest quality with a low defect concentration. On the cross-sectional m-plane cleavage surface, the interface dislocations induce steps in [0001]-direction in the InN region. These steps lead to an extrinsic pinning of the Fermi level. Further, in contrast to the publications of other groups, it turned out that an electron accumulation layer near the surface, caused by intrinsic surface states, cannot be observed on high quality, non-polar m-plane InN surfaces. Thus, the electron accumulation layer is not intrinsic and hence InN appears to be as conventional as other III-V semiconductors.

The simulation model developed in this thesis is universally applicable to most semiconductor materials and is not restricted to scanning tunneling spectroscopy measured under illumination. Hence, it can also be used for further investigations of future semiconductor materials and offers a helpful tool for the quantitative analysis of scanning tunneling spectroscopy measurements.

Bibliography

[1] R. D. McKirahan, *Philosophy Before Socrates (Second Edition): An Introduction with Texts and Commentary*. Hackett Publishing Company, 2011.

[2] I. Grattan-Guinness, *Landmark Writings in Western Mathematics 1640-1940*. Elsevier Science, 2005.

[3] J. Clerk-Maxwell, "On the Final State of a System of Molecules in Motion Subject to Forces of Any Kind," *Nature*, vol. 8, pp. 537–538, 1873.

[4] L. Boltzmann and F. Hasenöhrl, *Wissenschaftliche Abhandlungen: (1865-1874)*. No. Bd. 1, Barth, 1909.

[5] A. Einstein, "Über die von der molekularkinetischen Theorie der Wärme geforderte Bewegung von in ruhenden Flüssigkeiten suspendierten Teilchen," *Annalen der Physik*, vol. 322, no. 8, pp. 549–560, 1905.

[6] E. Ruska and M. Knoll, "Die magnetische Sammelspule für schnelle Elektronenstrahlen," *Z. techn. Physik*, vol. 12, pp. 389–400, 1931.

[7] A. V. Crewe, J. Wall, and J. Langmore, "Visibility of Single Atoms," *Science*, vol. 168, no. 3937, pp. 1338–1340, 1970.

[8] E. W. Müller, "Versuche zur Theorie der Elektronenemission unter der Einwirkung hoher Feldstärke," *Physikalische Zeitschrift*, vol. 37, pp. 838–842, 1936.

[9] E. W. Müller, "Das Feldionenmikroskop," *Zeitschrift für Physik*, vol. 131, no. 1, pp. 136–142, 1951.

[10] E. W. Müller, "Resolution of the Atomic Structure of a Metal Surface by the Field Ion Microscope," *J. Appl. Phys.*, vol. 27, no. 5, pp. 474–476, 1956.

[11] G. Binnig, H. Rohrer, C. Gerber, and E. Weibel, "Surface Studies by Scanning Tunneling Microscopy," *Phys. Rev. Lett.*, vol. 49, pp. 57–61, 1982.

[12] G. Binnig, H. Rohrer, C. Gerber, and E. Weibel, "Tunneling through a controllable vacuum gap," *Appl. Phys. Lett.*, vol. 40, no. 2, pp. 178–181, 1982.

[13] N. D. Jäger, E. R. Weber, K. Urban, and Ph. Ebert, "Importance of carrier dynamics and conservation of momentum in atom-selective STM imaging and band gap determination of GaAs(110)," *Phys. Rev. B*, vol. 67, p. 165327, 4 2003.

[14] M. B. Johnson, H. P. Meier, and H. W. M. Salemink, "Dopant and carrier profiling in modulation-doped GaAs multilayers with cross-sectional scanning tunneling microscopy," *Appl. Phys. Lett.*, vol. 63, no. 26, pp. 3636–3638, 1993.

[15] N. Ishida, K. Sueoka, and R. M. Feenstra, "Influence of surface states on tunneling spectra of n-type GaAs(110) surfaces," *Phys. Rev. B*, vol. 80, p. 075320, Aug 2009.

[16] M. Schnedler, Y. Jiang, K.H.Wu, E. Wang, R. Dunin-Borkowski, and Ph. Ebert, "Effective mass of a two-dimensional $\sqrt{3} \times \sqrt{3}$ Ga single atomic layer on Si(111)," *Surf. Sci.*, vol. 630, pp. 225–228, 2014.

[17] R. M. Feenstra, "Scanning tunneling spectroscopy," *Surf. Sci.*, vol. 299–300, pp. 965 – 979, 1994.

[18] P. Capiod, T. Xu, J. P. Nys, M. Berthe, G. Patriarche, L. Lymperakis, J. Neugebauer, P. Caroff, R. E. Dunin-Borkowski, Ph. Ebert, and B. Grandidier, "Band offsets at zincblende-wurtzite GaAs nanowire sidewall surfaces," *Appl. Phys. Lett.*, vol. 103, no. 12, p. 122104, 2013.

[19] P. Muralt, H. Meier, D. W. Pohl, and H. W. M. Salemink, "Scanning tunneling microscopy and potentiometry on a semiconductor heterojunction," *Appl. Phys. Lett.*, vol. 50, no. 19, pp. 1352–1354, 1987.

[20] R. M. Feenstra, "Cross-sectional scanning tunnelling microscopy of III-V semiconductor structures," *Semicond. Sci. Technol.*, vol. 9, no. 12, p. 2157, 1994.

[21] F. A. Ponce and D. P. Bour, "Nitride-based semiconductors for blue and green light-emitting devices," *Nature*, vol. 386, pp. 351–359, 1997.

[22] O. Jani, I. Ferguson, C. Honsberg, and S. Kurtz, "Design and characterization of GaN/InGaN solar cells," *Appl. Phys. Lett.*, vol. 91, no. 13, p. 132117, 2007.

[23] M. Asif Khan, A. Bhattarai, J. N. Kuznia, and D. T. Olson, "High electron mobility transistor based on a gan-al$_x$ga$_{1-x}$n heterojunction," *Appl. Phys. Lett.*, vol. 63, no. 9, pp. 1214–1215, 1993.

[24] Y. Xu, L. Chen, Y. Li, G. Song, Y. Wang, W. Zhuang, and Z. Long, "Phosphor-conversion white light using InGaN ultraviolet laser diode," *Appl. Phys. Lett.*, vol. 92, no. 2, p. 021129, 2008.

[25] M. A. Würtele, T. Kolbe, M. Lipsz, A. Külberg, M. Weyers, M. Kneissl, and M. Jekel, "Application of GaN-based ultraviolet-C light emitting diodes - UV LEDs - for water disinfection," *Water Research*, vol. 45, no. 3, pp. 1481 – 1489, 2011.

[26] P. H. Weidlich, M. Schnedler, H. Eisele, R. Dunin-Borkowski, and Ph. Ebert, "Repulsive interactions between dislocations and overgrown v-shaped defects in epitaxial GaN layers," *Appl. Phys. Lett.*, vol. 103, no. 14, p. 142105, 2013.

[27] P. H. Weidlich, M. Schnedler, H. Eisele, U. Strauß, R. E. Dunin-Borkowski, and Ph. Ebert, "Evidence of deep traps in overgrown v-shaped defects in epitaxial GaN layers," *Appl. Phys. Lett.*, vol. 103, no. 6, p. 062101, 2013.

[28] D. Segev and C. G. Van de Walle, "Origins of Fermi-level pinning on GaN and InN polar and nonpolar surfaces," *Europhys. Lett.*, vol. 76, no. 2, pp. 305–311, 2006.

[29] C. G. Van de Walle and D. Segev, "Microscopic origins of surface states on nitride surfaces," *J. Appl. Phys.*, vol. 101, no. 8, p. 081704, 2007.

[30] H. Ye, G. Chen, Y. Wu, Y. Zhu, and S.-H. Wei, "Stability of a planar-defect structure of the wurtzite AlN $(10\bar{1}0)$ surface: Density functional study," *Phys. Rev. B*, vol. 80, p. 033301, Jul 2009.

[31] M. Landmann, E. Rauls, W. G. Schmidt, M. D. Neumann, E. Speiser, and N. Esser, "GaN *m*-plane: Atomic structure, surface bands, and optical response," *Phys. Rev. B*, vol. 91, p. 035302, Jan 2015.

[32] V. Davydov, A. Klochikhin, V. Emtsev, S. Ivanov, V. Vekshin, F. Bechstedt, J. Furthmüller, H. Harima, A. Mudryi, A. Hashimoto, A. Yamamoto, J. Aderhold, J. Graul, and E. Haller, "Band Gap of InN and In-Rich $In_xGa_{1-x}N$ alloys $(0.36 < x < 1)$," *physica status solidi (b)*, vol. 230, no. 2, pp. R4–R6, 2002.

[33] J. W. Ager, N. Miller, R. E. Jones, K. M. Yu, J. Wu, W. J. Schaff, and W. Walukiewicz, "Mg-doped InN and InGaN Photoluminescence, capacitance-voltage and thermopower measurements," *phys. stat. sol. (b)*, vol. 245, no. 5, pp. 873–877, 2008.

[34] M.-S. Hu, G.-M. Hsu, K.-H. Chen, C.-J. Yu, H.-C. Hsu, L.-C. Chen, J.-S. Hwang, L.-S. Hong, and Y.-F. Chen, "Infrared lasing in InN nanobelts," *Appl. Phys. Lett.*, vol. 90, no. 12, p. 123109, 2007.

[35] P. G. Moses and C. G. Van de Walle, "Band bowing and band alignment in InGaN alloys," *Appl. Phys. Lett.*, vol. 96, no. 2, p. 021908, 2010.

[36] J. Wu, W. Walukiewicz, K. M. Yu, W. Shan, J. W. Ager, E. E. Haller, H. Lu, W. J. Schaff, W. K. Metzger, and S. Kurtz, "Superior radiation resistance of In_{1-x} Ga_xN alloys: Full-solar-spectrum photovoltaic material system," *J. Appl. Phys.*, vol. 94, no. 10, pp. 6477–6482, 2003.

[37] K. P. O'Donnell, R. W. Martin, and P. G. Middleton, "Origin of Luminescence from InGaN Diodes," *Phys. Rev. Lett.*, vol. 82, pp. 237–240, 1999.

[38] W. Tan, M. Kauer, S. Hooper, J. Barnes, M. Rossetti, T. Smeeton, V. Bousquet, and J. Heffernan, "High-power and long-lifetime InGaN blue-violet laser diodes grown by molecular beam epitaxy," *Electronics Letters*, vol. 44, pp. 351–352, Feb 2008.

[39] S. X. Li, K. M. Yu, J. Wu, R. E. Jones, W. Walukiewicz, J. W. Ager, W. Shan, E. E. Haller, H. Lu, and W. J. Schaff, "Fermi-level stabilization energy in group III nitrides," *Phys. Rev. B*, vol. 71, p. 161201, Apr 2005.

[40] P. D. C. King, T. D. Veal, C. F. McConville, F. Fuchs, J. Furthmüller, F. Bechstedt, P. Schley, R. Goldhahn, J. Schörmann, D. J. As, K. Lischka, D. Muto, H. Naoi, Y. Nanishi, H. Lu, and W. J. Schaff, "Unversality of electron accumulation at wurtzite *c*- and *a*-plane and zinc-blende InN surfaces," *Appl. Phys. Lett.*, vol. 91, no. 9, p. 092101, 2007.

[41] W. M. Linhart, T. D. Veal, P. D. C. King, G. Koblmüller, C. S. Gallinat, J. S. Speck, and C. F. McConville, "Surface, bulk, and interface electronic properties of nonpolar InN," *Appl. Phys. Lett.*, vol. 97, no. 11, p. 112103, 2010.

[42] E. Calleja, J. Grandal, M. A. Sánchez-García, M. Niebelschütz, V. Cimalla, and O. Ambacher, "Evidence of electron accumulation at nonpolar surfaces of InN nanocolumns," *Appl. Phys. Lett.*, vol. 90, no. 26, p. 262110, 2007.

[43] I. Mahboob, T. D. Veal, C. F. McConville, H. Lu, and W. J. Schaff, "Intrinsic Electron Accumulation at Clean InN Surfaces," *Phys. Rev. Lett.*, vol. 92, p. 036804, Jan 2004.

[44] T. Nagata, G. Koblmüller, O. Bierwagen, C. S. Gallinat, and J. S. Speck, "Surface structure and chemical states of a-plane and c-plane InN films," *Appl. Phys. Lett.*, vol. 95, no. 13, p. 132104, 2009.

[45] R. J. Hamers and K. Markert, "Atomically Resolved Carrier Recombination at Si(111)-(7×7) Surfaces," *Phys. Rev. Lett.*, vol. 64, no. 9, p. 1051, 1990.

[46] Y. Kuk, R. S. Becker, P. J. Silverman, and G. P. Kochanski, "Optical Interactions in the Junction of a Scanning Tunneling Microscope," *Phys. Rev. Lett.*, vol. 65, no. 4, p. 456, 1990.

[47] T. W. Matthes, C. Sommerhalter, A. Rettenberger, M. Böhmisch, J. Boneberg, M. C. Lux-Steiner, and P. Leiderer, "Investigation of photoinduced tunneling current and local surface photovoltage by STM," *Applied Surf. Sci.*, vol. 123/124, pp. 187–191, 1998.

[48] S. Aloni, I. Nevo, and G. Haase, "Local Fermi-level pinning at a single adatom (Cs) or vacancy (As) on a GaAs(110) surface," *Phys. Rev. B*, vol. 60, no. 4, p. 2165, 1999.

[49] S. Aloni, I. Nevo, and G. Haase, "Photovoltage imaging of a single As-vacancy at a GaAs(110) surface: Evidence for electron trapping by a charged defect?," *J. Chem. Phys.*, vol. 115, no. 4, p. 1875, 2001.

[50] S. Yoshida, Y. Kanitani, R. Oshima, Y. Okada, O. Takeuchi, and H. Shigekawa, "Microscopic Basis for the Mechanism of Carrier Dynamics in an Operating *p-n* Junction Examined by Using Light-Modulated Scanning Tunneling Spectroscopy," *Phys. Rev. Lett.*, vol. 98, p. 026802, Jan 2007.

[51] S. Yoshida, Y. Kanitani, O. Takeuchi, and H. Shigekawa, "Probing nanoscale potential modulation by defect-induced gap states on GaAs(110) with light-modulated scanning tunneling spectroscopy," *Appl. Phys. Lett.*, vol. 92, no. 10, p. 102105, 2008.

[52] S. Yoshida, Y. Kanitani, R. Oshima, Y. Okada, O. Takeuchi, and H. Shigekawa, "Nanoscale Mapping of Built-in Potential in GaAs p-n Junction Using Light-Modulated Scanning Tunneling Microscopy," *Jpn. J. Appl. Phys.*, vol. 47, no. 7, pp. 6117–6120, 2008.

[53] S. Landrock, Y. Jiang, K. H. Wu, E. G. Wang, K. Urban, and Ph. Ebert, "Origin of nanoscale potential fluctuations in two-dimensional semiconductors," *Appl. Phys. Lett.*, vol. 95, no. 7, p. 072107, 2009.

[54] F. Hund, "Zur Deutung der Molekelspektren. I," *Zeitschrift für Physik*, vol. 40, no. 10, pp. 742–764, 1927.

[55] W. Heisenberg, "Über den anschaulichen Inhalt der quantentheoretischen Kinematik und Mechanik," *Zeitschrift für Physik*, vol. 43, no. 3-4, pp. 172–198, 1927.

[56] F. Schwabl, *Quantenmechanik - Eine Einführung*. Berlin: Springer, 2007.

[57] M. Schnedler, "Towards a quantitative analysis of scanning tunneling spectroscopy," Diplomarbeit, RWTH Aachen, 2011.

[58] J. Chen, *Introduction to Scanning Tunneling Microscopy*. Oxford: Oxford University Press, 1993.

[59] J. Tersoff and D. R. Hamann, "Theory of the scanning tunneling microscope," *Phys. Rev. B*, vol. 31, pp. 805–813, Jan. 1985.

[60] J. Bardeen, "Tunnelling from a many-particle point of view," *Phys. Rev. Lett.*, vol. 6, no. 2, pp. 57–59, 1961.

[61] A. D. Gottlieb and L. Wesoloski, "Bardeen's tunnelling theory as applied to scanning tunnelling microscopy: a technical guide to the traditional interpretation," *Nanotechnol.*, vol. 17, no. 8, p. R57, 2006.

[62] J. Tersoff and D. R. Hamann, "Theory and Application for the Scanning Tunneling Microscope," *Phys. Rev. Lett.*, vol. 50, pp. 1998–2001, June 1983.

[63] G. Binnig, H. Rohrer, C. Gerber, and E. Weibel, "(111) facets as the origin of reconstructed Au(110) surfaces," *Surf. Sci. Lett.*, vol. 131, no. 1, pp. L379 – L384, 1983.

[64] S. Ohnishi and M. Tsukada, "Molecular orbital theory for the scanning tunneling microscopy," *Solid State Communications*, vol. 71, no. 5, pp. 391 – 394, 1989.

[65] J. Bono and R. H. Good, "Theoretical discussion of the scanning tunneling microscope applied to a semiconductor surface," *Surf. Sci.*, vol. 175, no. 2, pp. 415–420, 1986.

[66] R. M. Feenstra and J. A. Stroscio, "Tunneling spectroscopy of the GaAs(110) surface," *J. Vac. Sci. Technol. B*, vol. 5, no. 4, pp. 923–929, 1987.

[67] W. A. Harrison, "Tunneling from an Independent-Particle Point of View," *Phys. Rev.*, vol. 123, pp. 85–89, 1961.

[68] J. G. Simmons, "Generalized Formula for the Electric Tunnel Effect between Similar Electrodes Separated by a Thin Insulating Film," *J. Appl. Phys.*, vol. 34, no. 6, pp. 1793–1803, 1963.

[69] N. D. Jäger, Ph. Ebert, K. Urban, R. Krause-Rehberg, and E. R. Weber, "Scanning tunneling microscopy and spectroscopy of semi-insulating GaAs," *Phys. Rev. B*, vol. 65, p. 195318, May 2002.

[70] R. M. Feenstra, "Electrostatic Potential for a Hyperbolic Probe Tip near a Semiconductor," *J. Vac. Sci. Technol. B*, vol. 21, no. 5, pp. 2080–2088, 2003.

[71] R. Seiwatz and M. Green, "Space Charge Calucations for Semiconductors," *J. Appl. Phys.*, vol. 29, pp. 1034–1040, 1958.

[72] R. Sauer, *Halbleiterphysik: Lehrbuch für Physiker und Ingenieure*. Oldenbourg Wissenschaftsverlag GmbH, 2009.

[73] S. M. Sze and K. K. Ng, *Physics of Semiconductor Devices*. New York: Wiley-Interscience, 3 ed., 2007.

[74] J. S. Blakemore, "Approximations for Fermi-Dirac integrals, especially the function $F_{1/2}(\eta)$ used to describe electron density in a semiconductor," *Solid-State Electronics*, vol. 25, no. 11, pp. 1067–1076, 1982.

[75] N. D. Jäger, *Effects of individual dopant atoms on the electronic properties of GaAs investigated by scanning tunneling microscopy and spectroscopy*. No. 4053 in Berichte des Forschungszentrum Jülich, Jülich: Forschungszentrum Jülich GmbH, 2003.

[76] R. M. Feenstra, "Tunneling spectroscopy of the (110) surface of direct-gap III-V semiconductors," *Phys. Rev. B*, vol. 50, pp. 4561–4570, Aug 1994.

[77] S. Selberherr, *Analysis and Simulation of Semiconductor Devices*. Vienna, New York: Springer, 1984.

[78] R. M. Feenstra, Y. Dong, M. P. Semtsiv, and W. T. Masselink, "Influence of Tip-induced Band Bending on Tunneling Spectra of Semiconductor Surfaces," *Nanotechnol.*, vol. 18, p. 044015, 2007.

[79] H. C. Casey, D. D. Sell, and K. W. Wecht, "Concentration dependence of the absorption coefficient for n- and p-type GaAs between 1.3 and 1.6 eV," *J. Appl. Phys.*, vol. 46, no. 1, pp. 250–257, 1975.

[80] R. A. Smith, *Semiconductors*. Cambridge: Cambridge University Press, 1959.

[81] J. R. Chelikowsky and M. L. Cohen, "Nonlocal pseudopotential calculations for the electronic structure of eleven diamond and zinc-blende semiconductors," *Phys. Rev. B*, vol. 14, pp. 556–582, Jul 1976.

[82] J. R. Chelikowsky and M. L. Cohen, "Erratum: Nonlocal pseudopotential calculations for the electronic structure of eleven diamond and zinc-blende semiconductors," *Phys. Rev. B*, vol. 30, p. 4828, Oct 1984.

[83] D. Mehtani, N. Lee, R. D. Hartschuh, A. Kisliuk, M. D. Foster, A. P. Sokolov, F. Čajko, and I. Tsukerman, "Optical properties and enhancement factors of the tips for apertureless near-field optics," *J. Optics A*, vol. 8, no. 4, p. S183, 2006.

[84] V. Tsukruk and S. Singamaneni, *Scanning Probe Microscopy of Soft Matter: Fundamentals and Practices*. Weinheim: Wiley-VCH, 2012.

[85] J. Ibe, P. P. Bey, S. L. Brandow, R. A. Brizzolara, N. A. Burnham, D. P. DiLella, K. P. Lee, C. R. K. Marrian, and R. J. Colton, "On the electrochemical etching of tips for scanning tunneling microscopy," *J. Vac. Sci. Technol. A*, vol. 8, no. 4, pp. 3570–3575, 1990.

[86] K. H. Graf. private communication.

[87] Ph. Ebert, "Untersuchungen der InP(110)-Oberfläche mit dem Rastertunnelmikroskop," Diplomarbeit, RWTH Aachen, 1990.

[88] Ph. Ebert and K. Szot, "Scanning Probe Analysis," in *Nanoelectronics and Information Technology* (R. Waser, ed.), ch. 11, pp. 255–281, Weinheim: Wiley-VCH, 3 ed., 2012.

[89] D. A. Lenz. private communication.

[90] M. Schnedler, V. Portz, P. H. Weidlich, R. E. Dunin-Borkowski, and P. Ebert, "Quantitative description of photoexcited scanning tunneling spectroscopy and its application to the GaAs(110) surface," *Phys. Rev. B*, vol. 91, p. 235305, Jun 2015.

[91] V. Portz, "Laser excited scanning tunneling spectroscopy of semiconductor surfaces," Diplomarbeit, RWTH Aachen, 2013.

[92] For the photo-excited scanning tunneling microscopy and spectroscopy different, but essentially synonymous terms are used in the literature such as laser or light-excited, photo- or laser-assisted, light-modulated, optically pumped, and laser-combined STM, STM under (laser) irradiation, photo-induced tunnel current, or photovoltage imaging (using STM).

[93] S. Grafström, "Photoassisted scanning tunneling microscopy," *J. Appl. Phys.*, vol. 91, no. 4, pp. 1717–1753, 2002.

[94] M. McEllistrem, G. Haase, D. Chen, and R. J. Hamers, "Electrostatic sample-tip interactions in the scanning tunneling microscope," *Phys. Rev. Lett.*, vol. 70, pp. 2471–2474, Apr 1993.

[95] T. Takahashi and M. Yoshita, "Laser irradiation effects on tunneling properties of n-type GaAs and InAs by scanning tunneling microscopy," *Appl. Phys. Lett.*, vol. 68, no. 24, pp. 3479–3481, 1996.

[96] T. Takahashi and M. Yoshita, "Scanning tunneling spectroscopy of n-type GaAs under laser irradiation," *Appl. Phys. Lett.*, vol. 70, no. 16, p. 2162, 1997.

[97] K. Arima, H. Kakiuchi, M. Ikeda, K. Endo, M. Morita, and Y. Mori, "Visible Light Irradiation Effects on STM Observations of Hydrogenated Amorphous Silicon Surfaces," *Jpn. J. Appl. Phys.*, vol. 43, no. 4B, pp. 1891–1895, 2004.

[98] S. Yoshida, J. Kikuchi, Y. Kanitani, O. Takeuchi, H. Oigawa, and H. Shigekawa, "Tip-induced band bending and its effect on local barrier height measurement studied by light-modulated scanning tunneling spectroscopy," *e-Journal of Surf. Sci. and Nanotechnology*, vol. 4, pp. 192–196, 2006.

[99] M. W. J. Prins, R. Jansen, R. H. M. Groeneveld, A. P. van Gelder, and H. van Kempen, "Photoelectric properties of semiconductor tips in scanning tunneling microscopy," *Phys. Rev. B*, vol. 53, no. 12, pp. 8090–8104, 1996.

[100] C. Sommerhalter, T. W. Matthes, J. Boneberg, P. Leiderer, and M. C. Lux-Steiner, "Tunneling spectroscopy on semiconductors with a low surface state density," *J. Vac. Sci. Technol. B*, vol. 15, no. 6, 1997.

[101] D. Vu, S. Arscott, E. Peytavit, R. Ramdani, E. Gil, Y. André, S. Bansropun, B. Gérard, A. C. H. Rowe, and D. Paget, "Photoassisted tunneling from free-standing GaAs thin films into metallic surfaces," *Phys. Rev. B*, vol. 82, p. 115331, Sep 2010.

[102] S. Gaan, R. Feenstra, Ph. Ebert, R. Dunin-Borkowski, J. Walker, and E. Towe, "Structure and electronic spectroscopy of steps on GaAs(110) surfaces," *Surf. Sci.*, vol. 606, no. 1-2, pp. 28 – 33, 2012.

[103] Ph. Ebert, M. Heinrich, M. Simon, K. Urban, and M. G. Lagally, "Formation of anion vacancies by Langmuir evaporation from InP and GaAs (110) surfaces at low temperatures," *Phys. Rev. B*, vol. 51, pp. 9696–9701, Apr 1995.

[104] U. Semmler, M. Simon, Ph. Ebert, and K. Urban, "Stoichiometry changes by selective vacancy formation on (110) surfaces of III-V semiconductors: Influence of electronic effects," *J. Chem. Phys.*, vol. 114, no. 1, pp. 445–451, 2001.

[105] U. Semmler, M. Simon, Ph. Ebert, and K. Urban, "Erratum: Stoichiometry changes by selective vacancy formation on (110) surfaces of III-V semiconductors: Influence of electronic effects [J. Chem. Phys. 114, 445 (2001)]," *J. Chem. Phys.*, vol. 115, no. 15, pp. 7330–7330, 2001.

[106] Ph. Ebert, K. Urban, L. Aballe, C. H. Chen, K. Horn, G. Schwarz, J. Neugebauer, and M. Scheffler, "Symmetric Versus Nonsymmetric Structure of the Phosphorus Vacancy on InP(110)," *Phys. Rev. Lett.*, vol. 84, pp. 5816–5819, Jun 2000.

[107] R. Maboudian, K. Pond, V. Bressler-Hill, M. Wassermeier, P. Petroff, G. Briggs, and W. Weinberg, "Tunneling spectroscopy on the GaAs(110) surface: Effect of dopant concentration," *Surf. Sci.*, vol. 275, no. 1-2, pp. L662 – L668, 1992.

[108] R. Dombrowski, C. Steinebach, C. Wittneven, M. Morgenstern, and R. Wiesendanger, "Tip-induced band bending by scanning tunneling spectroscopy of the states of the tip-induced quantum dot on InAs(110)," *Phys. Rev. B*, vol. 59, pp. 8043–8048, Mar 1999.

[109] M. Wenderoth, M. A. Rosentreter, K. J. Engel, A. J. Heinrich, M. A. Schneider, and R. G. Ulbrich, "Low-temperature scanning tunneling spectroscopy as a probe for a confined electron gas," *Europhys. Lett.*, vol. 45, no. 5, pp. 579–584, 1999.

[110] Ph. Ebert, L. Ivanova, and H. Eisele, "Scanning tunneling microscopy on unpinned GaN(1-100) surfaces: Invisibility of valence-band states," *Phys. Rev. B*, vol. 80, p. 085316, 2009.

[111] N. D. Jäger, K. Urban, E. R. Weber, and Ph. Ebert, "Nanoscale dopant-induced dots and potential fluctuations in GaAs," *Appl. Phys. Lett.*, vol. 82, no. 16, pp. 2700–2702, 2003.

[112] P. H. Weidlich, R. E. Dunin-Borkowski, and Ph. Ebert, "Quantitative determination of local potential values in inhomogeneously doped semiconductors by scanning tunneling microscopy," *Phys. Rev. B*, vol. 84, p. 085210, Aug 2011.

[113] J. Chelikowsky and M. Cohen, "Electronic states on the relaxed (110) surface of GaAs," *Solid State Communications*, vol. 29, no. 3, pp. 267 – 271, 1979.

[114] J. Chelikowsky and M. Cohen, "Erratum: Electronic states on the relaxed (110) surface of GaAs," *Solid State Communications*, vol. 30, no. 12, p. 819, 1979.

[115] H. Carstensen, R. Claessen, R. Manzke, and M. Skibowski, "Direct determination of III-V semiconductor surface band gaps," *Phys. Rev. B*, vol. 41, pp. 9880–9885, May 1990.

[116] B. Engels, P. Richard, K. Schroeder, S. Blügel, Ph. Ebert, and K. Urban, "Comparison between *ab initio* theory and scanning tunneling microscopy for (110) surfaces of III-V semiconductors," *Phys. Rev. B*, vol. 58, pp. 7799–7815, Sep 1998.

[117] Ph. Ebert, "Atomic structure of point defects in compound semiconductor surfaces," *Curr. Opinion Sol. State Mat. Sci.*, vol. 5, no. 2-3, pp. 211 – 250, 2001.

[118] C. M. Colomb, S. A. Stockman, N. F. Gardner, A. P. Curtis, G. E. Stillman, T. S. Low, D. E. Mars, and D. B. Davito, "Zero-field time-of-flight characterization of minority-carrier transport in heavily carbon-doped GaAs," *J. Appl. Phys.*, vol. 73, no. 11, pp. 7471–7477, 1993.

[119] H. C. Casey and F. Stern, "Concentration-dependent absorption and spontaneous emission of heavily doped GaAs," *J. Appl. Phys.*, vol. 47, no. 2, pp. 631–643, 1976.

[120] U. Rössler and D. Strauch, eds., *Semiconductors, Group IV Elements, IV-IV and III-V Compounds. Part b - Electronic, Transport, Optical and Other Properties*, vol. III/41a1b of *Landolt-Börnstein, New Series*. Berlin: Springer, 2001.

[121] J. Bardeen, "Surface States and Rectification at a Metal Semi-Conductor Contact," *Phys. Rev.*, vol. 71, pp. 717–727, May 1947.

[122] W. Mönch, *Electronic structure of metal-semiconductor contacts*, vol. 4 of *Perspectives in condensed matter physics*. Dordrecht, Boston, London: Kluwer Academic Publishers, 1990.

[123] W. Mönch, *Semiconductor Surfaces and Interfaces*. Berlin: Springer, 3rd edition ed., 2001.

[124] J. Robertson, "Band offsets, Schottky barrier heights, and their effects on electronicdevices," *J. Vac. Sci. Technol. A*, vol. 31, no. 5, p. 050821, 2013.

[125] R. M. Feenstra, J. A. Stroscio, J. Tersoff, and A. P. Fein, "Atom-Selective Imaging of the GaAs(110) Surface," *Phys. Rev. Lett.*, vol. 58, no. 12, pp. 1192–1195, 1987.

[126] J. A. Stroscio, R. M. Feenstra, and A. P. Fein, "Local state density and long-range screening of adsorbed oxygen atoms on the GaAs(110) surface," *Phys. Rev. Lett.*, vol. 58, pp. 1668–1671, Apr 1987.

[127] D. V. Froelich, M. E. Lapeyre, J. D. Dow, and R. E. Allen, "Dependence of the GaAs (110) surface electronic state dispersion curves on the surface relaxation angle," *Superlattices Microstruct.*, vol. 1, no. 1, pp. 87 – 89, 1985.

[128] H. Eisele and P. Ebert, "Non-polar group-III nitride semiconductor surfaces," *phys. stat. sol. RRL*, vol. 6, no. 9-10, pp. 359–369, 2012.

[129] L. Ivanova, S. Borisova, H. Eisele, M. Dähne, A. Laubsch, and Ph. Ebert, "Surface states and origin of the Fermi level pinning on nonpolar GaN(100) surfaces," *Appl. Phys. Lett.*, vol. 93, no. 19, p. 192110, 2008.

[130] M. Bertelli, P. Löptien, M. Wenderoth, A. Rizzi, R. G. Ulbrich, M. C. Righi, A. Ferretti, L. Martin-Samos, C. M. Bertoni, and A. Catellani, "Atomic and electronic structure of the nonpolar GaN($1\bar{1}00$) surface," *Phys. Rev. B*, vol. 80, p. 115324, 9 2009.

[131] J. E. Northrup and J. Neugebauer, "Theory of GaN($10\bar{1}0$) and ($11\bar{2}0$) surfaces," *Phys. Rev. B*, vol. 53, pp. R10477–R10480, Apr. 1996.

[132] L. Lymperakis, P. H. Weidlich, H. Eisele, M. Schnedler, J.-P. Nys, B. Grandidier, D. Stievenard, R. E. Dunin-Borkowski, J. Neugebauer, and Ph. Ebert, "Hidden surface states at non-polar GaN ($10\bar{1}0$) facets: Intrinsic pinning of nanowires," *Appl. Phys. Lett.*, vol. 103, no. 15, p. 152101, 2013.

[133] Ph. Ebert, L. Ivanova, S. Borisova, H. Eisele, A. Laubsch, and M. Dähne, "Electronic properties of dislocations in GaN investigated by scanning tunneling microscopy," *Appl. Phys. Lett.*, vol. 94, no. 6, p. 062104, 2009.

[134] N. Jäger, M. Marso, M. Salmeron, E. R. Weber, K. Urban, and Ph. Ebert, "Physics of imaging $p - n$ junctions by scanning tunneling microscopy and spectroscopy," *Phys. Rev. B*, vol. 67, no. 165307, p. 165307, 2003.

[135] W. C. Martin and W. L. Wiese, *Atomic, molecular, and optical physics handbook*, ch. Atomic Spectroscopy, pp. 135–153. American Institute of Physics, 1996.

[136] S. Nakamura, S. Pearton, and G. Fasol, *The Blue Laser Diode: The Complete Story*. Springer, 2000. p. 34.

[137] V. N. Abakumov, V. I. Perel, and I. N. Yassievich, *Nonradiative recombination in semiconductors*, vol. 33 of *Modern Problems in condensed matter sciences*. Amsterdam, Oxford, New York, Tokyo: North Holland, 1991.

[138] C.-T. Kuo, K.-K. Chang, H.-W. Shiu, C.-R. Liu, L.-Y. Chang, C.-H. Chen, and S. Gwo, "Natural band alignments of InN/GaN/AlN nanorod heterojunctions," *Appl. Phys. Lett.*, vol. 99, no. 12, p. 122101, 2011.

[139] W. Walukiewicz, J. W. A. III, K. M. Yu, Z. Liliental-Weber, J. Wu, S. X. Li, R. E. Jones, and J. D. Denlinger, "Structure and electronic properties of InN and In-rich group III-nitride alloys," *J. Phys. D*, vol. 39, no. 5, p. R83, 2006.

[140] T. Inushima, V. Mamutin, V. Vekshin, S. Ivanov, T. Sakon, M. Motokawa, and S. Ohoya, "Physical properties of InN with the band gap energy of 1.1 eV," *J. Cryst. Growth*, vol. 227-228, no. 0, pp. 481 – 485, 2001.

[141] T. Inushima, D. K. Maude, N. Kato, H. Lu, W. J. Schaff, R. Tauk, Y. Meziani, S. Ruffenach, O. Briot, W. Knap, B. Gil, H. Miwa, A. Yamamoto, D. Muto, and Y. Nanishi, "Superconductivity of InN as an intrinsic property," *AIP Conference Proceedings*, vol. 893, no. 1, pp. 137–138, 2007.

[142] E. Tiras, M. Gunes, N. Balkan, R. Airey, and W. J. Schaff, "Superconductivity in heavily compensated Mg-doped InN," *Appl. Phys. Lett.*, vol. 94, no. 14, pp. –, 2009.

[143] C.-L. Wu, H.-M. Lee, C.-T. Kuo, C.-H. Chen, and S. Gwo, "Absence of Fermi-Level Pinning at Cleaved Nonpolar InN Surfaces," *Phys. Rev. Lett.*, vol. 101, p. 106803, Sep 2008.

[144] Ph. Ebert, S. Schaafhausen, A. Lenz, A. Sabitova, L. Ivanova., M. Dähne, Y.-L. Hong, S. Gwo., and H. Eisele, "Direct measurement of the band gap and Fermi level position at InN $(11\bar{2}0)$," *Appl. Phys. Lett.*, vol. 98, no. 6, p. 062103, 2011.

[145] K. A. Rickert, A. B. Ellis, F. J. Himpsel, H. Lu, W. Schaff, J. M. Redwing, F. Dwikusuma, and T. F. Kuech, "X-ray photoemission spectroscopic investigation of surface treatments, metal deposition, and electron accumulation on InN," *Appl. Phys. Lett.*, vol. 82, no. 19, p. 3254, 2003.

[146] C. L. Jia, M. Lentzen, and K. Urban, "Atomic-Resolution Imaging of Oxygen in Perovskite Ceramics," *Science*, vol. 299, no. 5608, pp. 870–873, 2003.

[147] M. de la Mata, C. Magen, J. Gazquez, M. I. B. Utama, M. Heiss, S. Lopatin, F. Furtmayr, C. J. Fernández-Rojas, B. Peng, J. R. Morante, R. Rurali,

M. Eickhoff, A. Fontcuberta i Morral, Q. Xiong, and J. Arbiol, "Polarity Assignment in ZnTe, GaAs, ZnO, and GaN-AlN Nanowires from Direct Dumbbell Analysis," *Nano Lett.*, vol. 12, no. 5, pp. 2579–2586, 2012.

[148] S. Gaan, G. He, R. M. Feenstra, J. Walker, and E. Towe, "Size, shape, composition, and electronic properties of InAs/GaAs quantum dots by scanning tunneling microscopy and spectroscopy," *J. Appl. Phys.*, vol. 108, p. 114315, 2010.

[149] M. Heinrich, C. Domke, Ph. Ebert, and K. Urban, "Charged steps on III-V compound semiconductor surfaces," *Phys. Rev. B*, vol. 53, pp. 10894–10897, Apr 1996.

[150] J. Wu, W. Walukiewicz, K. M. Yu, J. W. Ager, E. E. Haller, H. Lu, W. J. Schaff, Y. Saito, and Y. Nanishi, "Unusual properties of the fundamental band gap of InN," *Appl. Phys. Lett.*, vol. 80, no. 21, pp. 3967–3969, 2002.

[151] J. Wu, W. Walukiewicz, S. X. Li, R. Armitage, J. C. Ho, E. R. Weber, E. E. Haller, H. Lu, W. J. Schaff, A. Barcz, and R. Jakiela, "Effects of electron concentration on the optical absorption edge of InN," *Appl. Phys. Lett.*, vol. 84, no. 15, pp. 2805–2807, 2004.

[152] C. Boney and A. Bensaoula, *Molecular Beam Epitaxy: From Research to Mass Production*, ch. Molecular beam epitaxy of low-bandgap InGaN. Waltham, Oxford: Elsevier Science, 2012. p. 245.

[153] A. Sabitova, Ph. Ebert, A. Lenz, S. Schaafhausen, L. Ivanova, M. Dähne, A. Hoffmann, R. E. Dunin-Borkowski, A. Förster, B. Grandidier, and H. Eisele, "Intrinsic bandgap of cleaved ZnO($11\bar{2}0$) surfaces," *Appl. Phys. Lett.*, vol. 102, no. 2, p. 021608, 2013.

List of own publications

Publications that are included in this thesis in a modified version are marked with asterisks (*).

[P1] M. Schnedler, V. Portz, P. H. Weidlich, R. E. Dunin-Borkowski, and Ph. Ebert, "Quantitative description of photoexcited scanning tunneling spectroscopy and its application to the GaAs(110) surface", *Phys. Rev. B*, vol. 91, pp. 235305, 2015*

[P2] M. Schnedler, V. Portz, H. Eisele, R. E. Dunin-Borkowski, and Ph. Ebert, "Polarity-dependent pinning of a surface state", Phys. Rev. B, vol. 91, pp. 205309, 2015*

[P3] M. Schnedler, Y. Jiang, K. H. Wu, E. Wang, R. E. Dunin-Borkowski, and Ph. Ebert, "Effective mass of a two-dimensional $\sqrt{3} \times \sqrt{3}$ Ga single atomic layer on Si(111)", *Surf. Sci.*, vol. 630, pp. 225-228, 2014

[P4] M. Schnedler, P. H. Weidlich, V. Portz, D. Weber, R. E. Dunin-Borkowski, and Ph. Ebert, "Correction of nonlinear lateral distortions of scanning probe microscopy images", *Ultramicroscopy*, vol. 136, pp. 86-90, 2014

[P5] P. H. Weidlich, M. Schnedler, V. Portz, H. Eisele, R. E. Dunin-Borkowski, and Ph. Ebert, "Meandering of overgrown v-shaped defects in epitaxial GaN layers", *Appl. Phys. Lett.*, vol. 105, p. 012105, 2014

[P6] P. H. Weidlich, M. Schnedler, H. Eisele, R. E. Dunin-Borkowski, and Ph. Ebert, "Repulsive interactions between dislocations and overgrown v-shaped defects in epitaxial GaN layers", *Appl. Phys. Lett.*, vol. 103, p. 142105, 2013

[P7] P. H. Weidlich, M. Schnedler, H. Eisele, U. Strauß, R. E. Dunin-Borkowski, and Ph. Ebert, "Evidence of deep traps in overgrown v-shaped defects in epitaxial GaN layers," *Appl. Phys. Lett.*, vol. 103, p. 062101, 2013

[P8] L. Lymperakis, P. H. Weidlich, H. Eisele, M. Schnedler, J.-P. Nys, B. Grandidier, D. Stievenard, R. E. Dunin-Borkowski, J. Neugebauer, and Ph. Ebert, "Hidden surface states at non-polar GaN $(10\bar{1}0)$ facets: Intrinsic pinning of nanowires," *Appl. Phys. Lett.*, vol. 103, no. 15, p. 152101, 2013

Acknowledgment

First of all, I would like to thank Prof. Dr. R. Dunin-Borkowski, who generously enabled me to write my PhD thesis at the Institute of Microstructure Research of the Peter Grünberg Institute (PGI 5, Forschungszentrum Jülich).

My special thanks go to Priv.-Doz. Dr. Ph. Ebert for supervising this thesis and for his support and guidance during the measurements, the analysis of the data, and the development of new theoretical models.

Furthermore my thanks go to Prof. Dr. M. Morgenstern from the II. Physikalisches Institut B of the RWTH Aachen University for the co-supervision.

I also want to thank Prof. Dr. M. Dähne, Dr. A. Lenz, Dipl.-Phys. J. Schuppang, and especially Priv.-Doz. Dr. H. Eisele from the Institut für Festkörperphysik at the Technische Universität Berlin for numerous physical discussions and ideas and for giving me the opportunity to perform measurements using their microscopes.

In this context, further thanks go to Dr. B. Grandidier, J. P. Nys, and M. Berthe from the Institut d'Electronique, de Microélectronique et de Nanotechnologie in Lille, France for enabling me to use their microscopes, too.

I would also thank Prof. Dr. S. Selberherr from the Institute for Microelectronics at the Technische Universität Wien in Vienna, Austria for fruitful discussions via mail concerning the accuracy of the finite-difference algorithms.

My thanks also go to Dr. M. Duchamp from the Ernst Ruska-Centre at the Forschungszentrum Jülich for the measurement of HR-TEM images of the InN/GaN interface.

The GaN samples were supplied by the "Advanced Semiconductors For Photonics And Electronics Lab" (LASPE) under the direction of Prof. N. Grandjean at the École Polytechnique Fédérale de Lausanne, Switzerland and hence my thanks go to them as well.

In addition I want to thank Dr. S. Choi and Prof. Dr. J. Speck from the Materials Department of the University of California Santa Barbara (UCSB) in Santa Barbara, US, for the growth of the InN samples.

Furthermore my thanks go to K.H. Graf for the technical support, discussions about the technical aspects of STM and STS, and the maintenance of the technical equipment.

In addition, thanks go to D. Meertens from the Ernst Ruska-Centre at the Forschungszentrum Jülich for SEM measurements.

A great thank you for the positive cooperation to Dr. Ph. Weidlich and to Dipl.-Phys. V. Portz for scientific discussions and joint measurements as well as for software testing. Furthermore, I want to thank Dipl.-Phys. V. Portz for generating and providing Fig. 3.2.

Last but not least a big thank-you to my parents for their support.

Band / Volume 30
Parallelisation potential of image segmentation in hierarchical island structures on hardware-accelerated platforms in real-time applications
S. Suslov (2013), xiv, 211 pp
ISBN: 978-3-89336-914-0

Band / Volume 31
Carrier mobility in advanced channel materials using alternative gate dielectrics
E. Durğun Özben (2014), 111 pp
ISBN: 978-3-89336-941-6

Band / Volume 32
Electrical characterization of manganite and titanate heterostructures
A. Herpers (2014), ix, 165 pp
ISBN: 978-3-89336-948-5

Band / Volume 33
Oxygen transport in thin oxide films at high field strength
D. Weber (2014), XII, 115 pp
ISBN: 978-3-89336-950-8

Band / Volume 34
Structure, electronic properties, and interactions of defects in epitaxial GaN layers
P. H. Weidlich (2014), 139 pp
ISBN: 978-3-89336-951-5

Band / Volume 35
Defect Engineering of $SrTiO_3$ thin films for resistive switching applications
S. Wicklein (2014), xi, 144 pp
ISBN: 978-3-89336-963-8

Band / Volume 36
Integration and Characterization of Atomic Layer Deposited TiO_2 Thin Films for Resistive Switching Applications
M. Reiners (2014), xiv, 166 pp
ISBN: 978-3-89336-970-6

Band / Volume 37
Resistive switching in ZrO_2 based metal-oxide-metal structures
I. Kärkkänen (2014), xviii, 125 pp
ISBN: 978-3-89336-971-3

Band / Volume 38
Resistive switching phenomena of extended defects in Nb-doped $SrTiO_3$ under influence of external gradients
C. Rodenbücher (2014), xiii, 200 pp
ISBN: 978-3-89336-980-5

Band / Volume 39
Micro-spectroscopic investigation of valence change processes in resistive switching $SrTiO_3$ thin films
A. Köhl (2014), viii, 166 pp
ISBN: 978-3-89336-988-1

Band / Volume 40
Strained Silicon and Silicon-Germanium Nanowire Tunnel FETs and Inverters
S. Richter (2014), iii, 117 pp
ISBN: 978-3-95806-002-9

Band / Volume 41
Integration of Redox-Based Resistive Switching Memory Devices
F. Lentz (2014), i, 166 pp
ISBN: 978-3-95806-019-7

Band / Volume 42
Ladungstransportuntersuchungen an nanofunktionalen Bauelementen mit Diodencharakteristik basierend auf funktionalisierten Nanopartikeln
N. Babajani (2015), iv, 138, XLVII
ISBN: 978-3-95806-026-5

Band / Volume 43
Transport and Noise Properties of Nanostructure Transistors for Biosensor Applications
J. Li (2015), vii, 175 pp
ISBN: 978-3-95806-034-0

Band / Volume 44
Quantitative scanning tunneling spectroscopy of non-polar III-V compound semiconductor surfaces
M. Schnedler (2015), 122 pp
ISBN: 978-3-95806-075-3

Information
Band / Volume 44
ISBN 978-3-95806-075-3